

Linköping University | Department of Physics, Chemistry and Biology
Master's Thesis, 60 ECTS | Educational Program: Chemistry
2023 | 23/4257—SE

A Quantum Chemical Investigation of Chemical Vapour Deposition of Fe using Ferrocene and Plasma Electrons

Felicia Andersson

Examiner: Professor Lars Ojamäe

Supervisor: Professor Henrik Pedersen



Linköpings universitet
SE-581 83 Linköping
013-28 10 00, www.liu.se

Upphovsrätt

Detta dokument hålls tillgängligt på Internet - eller dess framtida ersättare - under 25 år från publiceringsdatum under förutsättning att inga extraordinära omständigheter uppstår.

Tillgång till dokumentet innebär tillstånd för var och en att läsa, ladda ner, skriva ut enstaka kopior för enskilt bruk och att använda det oförändrat för icke-kommersiell forskning och för undervisning. Överföring av upphovsrätten vid en senare tidpunkt kan inte upphäva detta tillstånd. All annan användning av dokumentet kräver upphovsmannens medgivande. För att garantera äktheten, säkerheten och tillgängligheten finns lösningar av teknisk och administrativ art.

Upphovsmannens ideella rätt innefattar rätt att bli nämnd som upphovsman i den omfattning som god sed kräver vid användning av dokumentet på ovan beskrivna sätt samt skydd mot att dokumentet ändras eller presenteras i sådan form eller i sådant sammanhang som är kränkande för upphovsmannens litterära eller konstnärliga anseende eller egenart.

För ytterligare information om Linköping University Electronic Press se förlagets hemsida <http://www.ep.liu.se/>.

Copyright

The publishers will keep this document online on the Internet - or its possible replacement - for a period of 25 years starting from the date of publication barring exceptional circumstances.

The online availability of the document implies permanent permission for anyone to read, to download, or to print out single copies for his/hers own use and to use it unchanged for non-commercial research and educational purpose. Subsequent transfers of copyright cannot revoke this permission. All other uses of the document are conditional upon the consent of the copyright owner. The publisher has taken technical and administrative measures to assure authenticity, security and accessibility.

According to intellectual property law the author has the right to be mentioned when his/her work is accessed as described above and to be protected against infringement.

For additional information about the Linköping University Electronic Press and its procedures for publication and for assurance of document integrity, please refer to its www home page: <http://www.ep.liu.se/>.

© Felicia Andersson

Abstract

Thin films provide a remarkable asset, as depositing a thin surface layer can completely alter a material's characteristics and provide new, inexpensive, and valuable properties. In 2020, a new Chemical Vapour Deposition (CVD) approach was developed at Linköping University, using plasma electrons as reducing agents for the deposition of metallic thin films. To understand the CVD approach, comprehension of the deposition chemistry is crucial.

In this thesis, I have performed a theoretical examination of the gas phase and surface chemistry of ferrocene in the recently developed CVD method to form metallic iron thin films, using plasma electrons as reducing agents. Results show that ferrocene anion formation and dissociation are probable in the gas phase, depending on the energy of the plasma electrons. It gets successively easier to dissociate the complex after gaining electrons. The most probable gas phase species leading to film formation was determined FeCp_2^- , FeCp , and Cp^- under the normal deposition parameters. An electron energy above 220 kJ/mol would suffice for ion formation and dissociation to form FeCp and Cp^- fragments.

On the surface, ferrocene's vertical and horizontal adsorption is equally probable, with energies around -72 kJ/mol. Cp , Fe , and FeCp with Fe facing towards the surface interacts stronger with the surface than ferrocene, with adsorption energies of -179, -279 kJ/mol, and -284 kJ/mol. FeCp with Fe facing up from the surface had adsorption energy of -23 kJ/mol. As the surface bonding of Fe and FeCp with Fe facing the surface is stronger than for the other species, this poses a possible way of tuning the CVD method to limit carbon impurities. By providing above 180 kJ/mol energy, for example in the form of heating the substrate, the unwanted species FeCp_2 , Cp , and FeCp with the ring facing downwards would desorb from the surface, leaving the Fe and FeCp fragments with iron facing towards the surface still adsorbed. This poses a possible way of reducing carbon impurities.

Acknowledgements

I would like to begin by expressing my deepest gratitude and heartfelt appreciation to all those who have extended support, guidance, and encouragement to me during my time at Linköping University and during this master's project.

First of all, I would like to express my sincere gratitude and appreciation to my examiner Professor Lars Ojamäe. Thank you for introducing me to the field of computational chemistry during my bachelor's thesis. Thank you for your willingness of being the examiner in my project course, and for making it possible for me to specialise my master's profile the way I wanted to. Thank you for all your help with my master's project, your support, insightful feedback, and discussions, and for the opportunity to be part of your research group for the past one and a half years. Thank you for being the best examiner I could have ever wished for.

To my supervisor, Professor Henrik Pedersen, thank you for the opportunity of making this project possible. I am so grateful for all your help, enthusiasm, support, and encouragement and for welcoming me into your research group.

To the members of the Computational group, Giane Benvinda Damas, and Karl Rönby. Your willingness to share your expertise with me has been invaluable and I am forever grateful for the knowledge and skills I have acquired through your guidance. Thank you for welcoming me into the group with open arms, for all the meaningful discussions, and for all the fun times.

To the current and past members of the e-CVD group, Pentti Niiranen, Daniel Lundin, Hama Nadhom, and Charlotte Carpentier. Thank you for your insights and for always being supportive.

To my dear friends, thank you for your unwavering support throughout my five years at the University. Thank you for the fun times, shared laughter, and beautiful friendships that have made this academic journey so memorable and meaningful.

Lastly, to my family, for your unending love, support, belief in my abilities, and encouragement.

Contents

1	Introduction	1
1.1	Chemical vapour deposition of metallic thin films	1
1.2	Ferrocene	3
1.3	Thesis objective	3
2	Background	4
2.1	Ferrocene electronic structure	4
2.2	Ferrocene geometry and dissociation	7
2.3	Ferrocene adsorption on surfaces	9
3	Quantum Chemical Methodology	11
3.1	Quantum Chemistry	11
3.1.1	The Schrödinger equation and the many body problem . . .	11
3.1.2	The Hartree-Fock method	12
3.2	Density Functional Theory	14
3.2.1	The theorems of Hohenberg and Kohn	14
3.2.2	The Kohn-Sham approach	15
3.2.3	Exchange-correlation functionals	17
3.3	Statistical mechanics	18
3.4	Quantum Chemical modelling	19
3.4.1	Energy Optimisation and Vibrational analysis	19
3.4.2	Molecular Quantum Chemistry Modelling	19
3.4.3	Periodic calculations for solid-state quantum chemical mod- elling	20
3.4.4	Bulk characterisation	21
3.4.5	Surface energy	22
3.4.6	Adsorption energy	22
3.4.7	Density of states analysis	22
3.4.8	Bader charge analysis	22
4	Computational details	23
4.1	Gas phase chemistry	23
4.1.1	Electronic spin states and geometry	23
4.1.2	Ion formation electronic energies, enthalpies, and Gibbs free energies	24
4.1.3	Ferrocene dissociation	25
4.2	Surface chemistry	26
4.2.1	Bulk silver crystal structure	26

4.2.2	Isolated silver atom	26
4.2.3	Cohesive energy	27
4.2.4	Surface energies	27
4.2.5	Crystal layer convergence and extension	27
4.2.6	Isolated ferrocene	28
4.2.7	Adsorption system	28
4.2.8	Adsorption energy	28
4.2.9	Density of States & Bader charge analysis	29
4.2.10	Adsorption of fragments	29
4.2.11	Vertical decomposition	29
4.2.12	Horizontal decomposition	29
5	Gas phase chemistry	30
5.1	Electronic spin states and molecular structures	30
5.1.1	Relative electronic spin states	30
5.1.2	FeCp ₂	31
5.1.3	FeCp ₂ ions	33
5.1.4	FeCp fragments	33
5.1.5	Cp fragments	34
5.1.6	Fe fragments	35
5.2	Electronic energies, enthalpies and Gibbs free energies of ion formation	36
5.3	Ferrocene dissociation	39
6	Surface Chemistry	43
6.1	Bulk and crystal characterisation	43
6.1.1	Isolated Silver atom and Cohesive energy	44
6.1.2	Slab models and surface energies	44
6.1.3	Convergence of the crystal layers and extension of the crystal structure	46
6.2	Isolated ferrocene	47
6.3	Ferrocene adsorption	48
6.3.1	Vertical adsorption	49
6.3.2	Horizontal adsorption	50
6.4	Electronic structure analysis	51
6.4.1	Density of states	51
6.4.2	Bader charge analysis	55
6.5	Vertical ferrocene surface decomposition	56
6.5.1	Fe adsorption	56
6.5.2	Cp adsorption	58
6.5.3	FeCp adsorption	61
6.5.4	Vertical decomposition	63

6.6	Horizontal ferrocene surface decomposition	64
7	Concluding Remarks & Future Outlook	66
8	Appendix	75
8.1	Appendix A.	75
8.2	Appendix B.	80
8.3	Appendix C.	83
8.4	Appendix D.	85

1 Introduction

1.1 Chemical vapour deposition of metallic thin films

Thin films have been utilised for centuries and are applied for numerous purposes to enhance everyday life. They provide a remarkable asset as depositing a thin layer, typically ranging in nano to micrometers, on top of a bulk material can alter the characteristics and provide new, inexpensive, and valuable properties [1]. Metallic thin films can improve several attributes, such as optical [1], coating [1–4], electrical [1, 5], mechanical [2–4], chemical [2], magnetic [6, 7], and catalytic [8, 9] properties. Hence, they have multiple meaningful application areas, such as in electronics, coatings, optics, and catalysis [10, 11]. The deposition is feasible through different techniques, such as Physical Vapour Deposition (PVD) and Chemical Vapour Deposition (CVD). In CVD, the molecular species, called precursors, are typically introduced with a carrier gas into a heated CVD chamber (Figure 1), where molecules react and form a thin film on top of a substrate [10, 12, 13]. In PVD, the deposition involves purely physical impacts [10, 12]. As opposed to PVD, CVD is not a line-of-sight process. Therefore, CVD is superior for specific applications, such as when films of high uniformity or large areas are required [10, 12–14]. Additionally, plasma-enhanced CVD may enhance film quality and growth rate by providing extra energy or changing the chemical pathways [3].

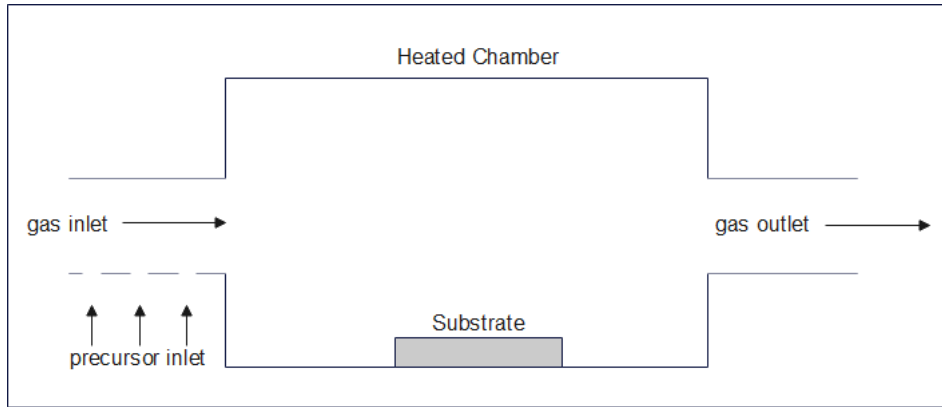


Figure 1: A simple schematic drawing of a CVD chamber.

In CVD, many simultaneous reactions can occur, and both gas phase and surface reactions are relevant for thin film growth. Such reactions include precursor decomposition, gas phase reactions of the precursor, and adsorption, diffusion, nucleation, and desorption at the surface, as visualised in Figure 2. As can be described by fluid dynamics, the friction encountered by gas when flown above a surface creates a fluid-flow boundary layer where the velocity and concentration of species differ. The species must diffuse through this boundary layer, where the

lower speed makes them reside longer and chemical reactions more likely to occur. On the surface, the adsorbed species, called the adsorbate, can diffuse to find more energetically favourable sites. If the adsorption strength is insufficient, some species may desorb after adsorption. [10, 12]

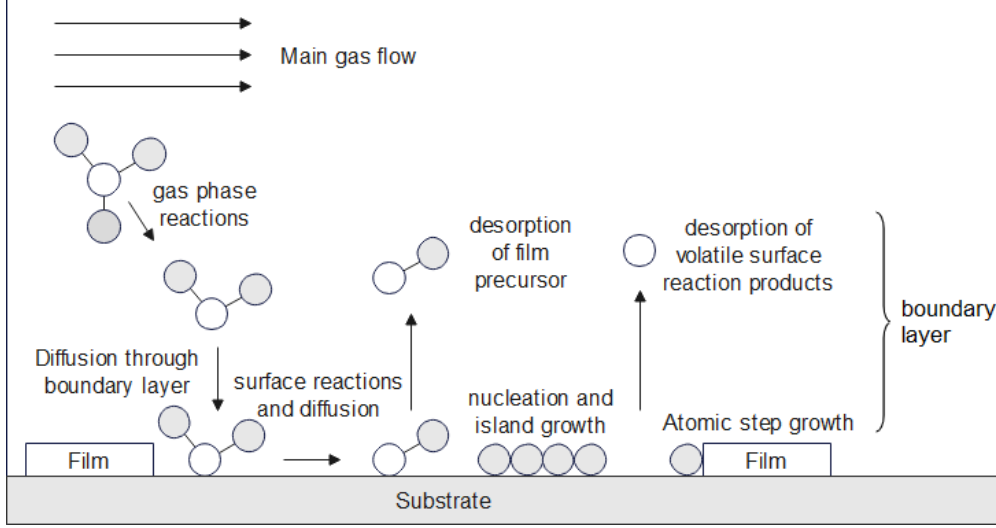


Figure 2: Schematic drawing of the most relevant chemical reactions inside a CVD chamber, inspired by Figure in [12].

In 2020, Nadhom et al. [15] demonstrated a unique CVD technique to deposit metallic thin films, using plasma electrons as reducing agents for metal-containing precursors. The electrons are drawn towards the substrate surface using a positive bias (see schematic drawing in Figure 3). In a cold plasma, the energy of the electrons is significantly higher than that of the ions. The collision between high-energy plasma electrons and precursors can break chemical bonds, producing new fragments such as radicals and ions in the gas phase or on the surface. Using plasma as an energy source enables low deposition temperatures and the deposition of metals with a

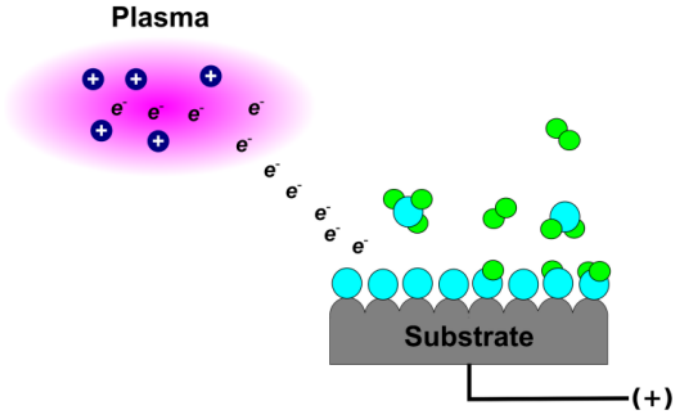


Figure 3: Schematic representation of the new CVD method described in [15]. Courtesy of Henrik Pedersen, used with permission.

low reduction potential, which is generally difficult due to their oxidising tendency. Such an example is an iron thin film (74 at.% Fe) deposited from a ferrocene precursor on a cold (35-50°C) Ag substrate, using the CVD approach. Additionally, the method has been proven area-selective depending on substrate resistivity[16] and adhesive masking[14]. The new CVD approach has several meaningful application areas. For instance, it opens for less complicated electronics and elemental semiconductors manufacturing and enables using temperature-sensitive materials in, for example, patterning applications [3].

1.2 Ferrocene

Ferrocene and other metallocenes are used extensively as CVD precursors [10]. Ferrocene has two five-carbon cyclopentadienyl anions (Cp^-), centered by a positively valenced iron (Fe^{2+}) [17–19]. Figure 4 shows the staggered and eclipsed ferrocene conformations. Each Cp^- ring holds six π -electrons equally shared by five orbitals to form an essentially aromatic structure. [20]

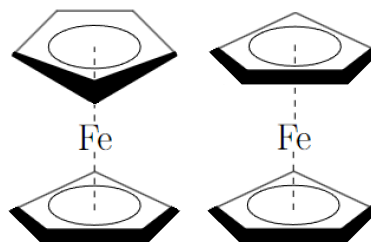


Figure 4: Ferrocene staggered (left) and eclipsed (right) conformational structure.

1.3 Thesis objective

This thesis focuses on the formation of iron (Fe) thin films on silver (Ag), using ferrocene (FeCp_2) as a precursor and plasma electrons as a reducing agent in the CVD approach presented by Nadhom et al. [15]. So far, the chemical reactions and mechanisms of the new CVD technique are limited. Additional investigations are required to understand the gas phase, surface chemistry, and the effects of the plasma, leaving a knowledge gap to be filled by further research. Knowledge about the gas phase and surface reactions is crucial for understanding and advancing CVD processes and deposited materials. As CVD systems often limit the performance of in-situ measurements, analyses are usually constrained to ex-situ analyses. Therefore, computational studies provide an invaluable tool for knowledge about the chemistry occurring during CVD processes.

In this thesis, I employ Quantum Chemical methodology to unveil information about the previously mentioned CVD method. Here, I examine gas phase and surface chemistry on an Ag(111) surface for ferrocene and decomposition fragments. The Gaussian 16 and the Vienna Ab-Initio Simulation Package (VASP) were used to compute the gas phase and surface reactions. The National Academic Infrastructure for Supercomputing in Sweden (NAISS), and the National Supercomputer Centre (NSC) at Linköping University provided the computational resources.

2 Background

2.1 Ferrocene electronic structure

Iron is a transition metal (TM) with an electronic configuration of $[\text{Ar}]3d^64s^2$, with five d-orbitals containing six d-electrons. Due to the incompletely filled d-orbitals, Fe and its complexes exhibit several close-lying spin states [21]. Ferrocene adopts an approximately octahedral geometry, where the Fe d-orbitals split into triply degenerate low-energy orbitals (d_{xz} , d_{xy} , d_{yz}) and doubly degenerate high-energy orbitals (d_{z^2} , $d_{x^2-y^2}$) under the influence of the octahedral crystal field. This splitting, known as orbital spin splitting, is characterized by the ligand-field splitting parameter, Δ_{oct} . The degree of spin splitting depends on the strength of the ligand, the metal identity, and the metal charge [18]. Compared to the energy state of the degenerate orbitals, referred to as the barycentre, the low-energy orbitals (labelled t_{2g}) lie $\frac{2}{5}\Delta_{oct}$ lower in energy, and the high-energy orbitals (labelled e_g) lie $\frac{3}{5}\Delta_{oct}$ higher in energy. The energy differences arise due to the repulsion between the ligand and metal orbitals. The t_{2g} orbitals locate between the ligands, whereas the e_g orbitals align with the ligand axis, creating repulsion forces. As a result, the t_{2g} orbitals are more involved in metal-ligand bonding. Molecules in low and high spin states correspond to electrons occupying low or high-energy orbitals, respectively. For the iron d-orbitals, the low and high spin states are the singlet and quintet states, respectively (Figure 5). Ferrocene is considered to be a low-spin complex.

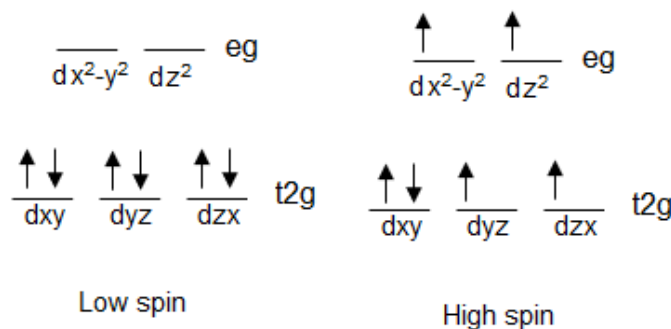


Figure 5: Schematic drawing of the occupation of the spin-split iron d-orbitals for the low (singlet) and high (quintet) spin state in an octahedral field.

The cyclopentadienyl anion (Cp^-) has a practically aromatic structure with three delocalized pairs of electrons around the ring. Cp^- belongs to the D_{5h} point group, and the orbitals form a_2'' , e_1'' , and e_2'' orbitals with increasing energy, varying from bonding to weakly bonding to anti-bonding (Figure 6). The e_1'' and e_2'' orbitals are doubly degenerate. Electrons fill the orbitals from lowest to highest energy, leaving the e_2'' orbitals unfilled. The orbitals of two Cp^- rings can combine to form ten ligand orbitals with $a_1' < a_2'' < e_1' < e_1'' < e_2' < e_2''$ (Figure 7), where e_1' , e_1'' , e_2' , and e_2'' are doubly degenerate. [22]

Ferrocene forms by combining the orbitals of Fe and two Cp^- orbitals, creating an 18-electron complex with five electrons from each Cp^- ring and eight from Fe^{2+} . [20] An 18-electron system is generally considered a very stable configuration. The most significant contributions to the bonding come from the Fe d-orbitals and π -bonds in Cp^- . [23]

In the eclipsed ferrocene (D_{5h}), the orbitals are occupied in the following order: $a_1' < a_2'' < e_1'' < e_1' < e_2' < a_1'' < e_2''$ (nb) $< e_2''^* < a_1'^* < a_2''^* < e_1'^*$ (Figure 8). The first two orbitals (a_1' , a_2'') are mainly contributed from the Cp^- orbitals, with a small contribution of the $4s$, $4p_z$, and $3d_{z^2}$ Fe orbitals.

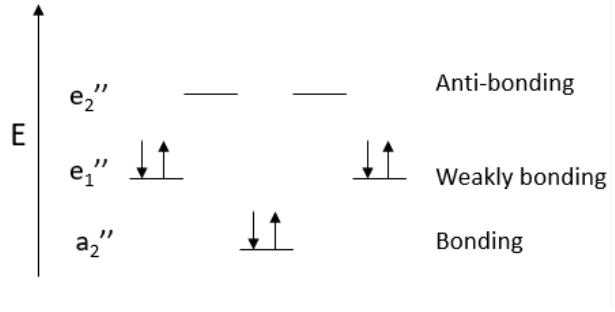


Figure 6: Schematic drawing of the electron occupation of the orbitals in the cyclopentadienyl anion (Cp^-).

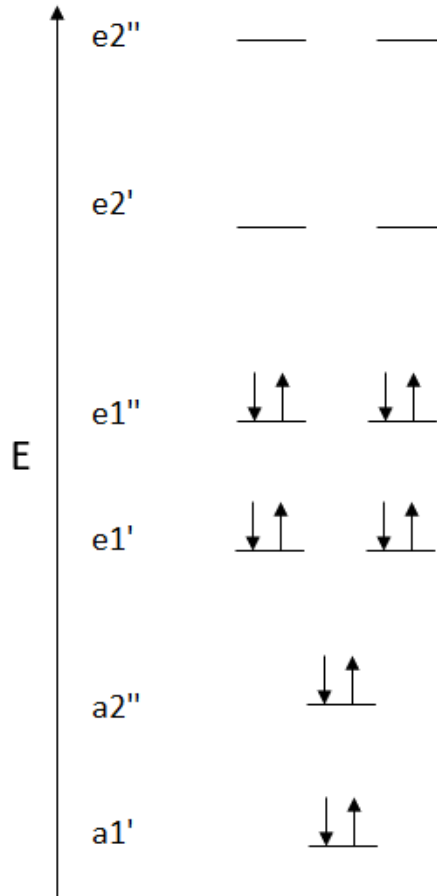


Figure 7: Schematic drawing of the electron occupation of the orbitals of two cyclopentadienyl anions (Cp_2).

The e_1'' orbitals involve the interaction between the ligand and the d_{xz} , d_{yz} Fe-orbitals, the most crucial factor in the complex stabilization as these orbitals have the strongest overlap between the ligand and metal. The following orbital (e_1') is mainly from the Cp orbitals, with a small contribution from the Fe $3p_x, p_y$ orbitals. The three next orbitals are metal d-character orbitals from the contribution of (d_{xy} , $d_{x^2-y^2}$), (d_{z^2}), and (d_{yz} , d_{xz}). These orbitals vary from weakly bonding (e_2') to practically non-bonding (a_1') to anti-bonding ($e_1''^*$). The a_1' orbital is the highest occupied molecular orbital (HOMO). The $e_1''^*$ orbitals are unfilled in the ground state and are the lowest unoccupied molecular orbitals (LUMO). However, it is worth noting that the relative energies of these orbitals have been somewhat ambiguous. [20] Ferrocene is previously recognised to be in a singlet state under normal conditions. [23–25]

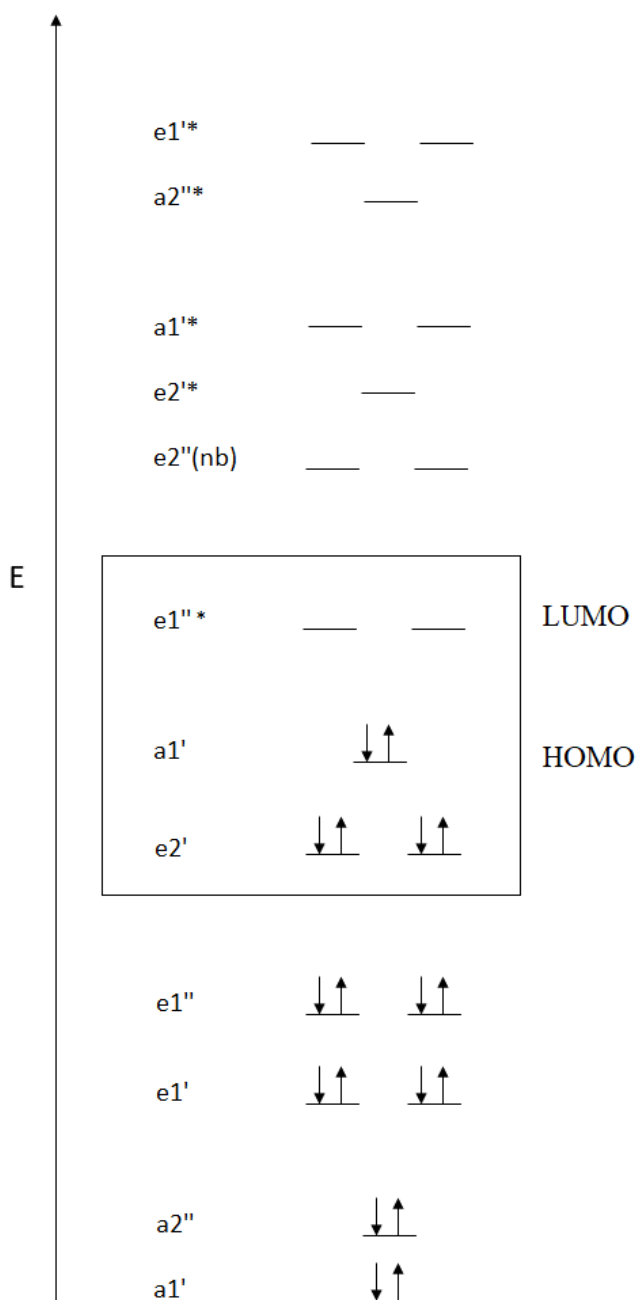


Figure 8: Schematic drawing of the electron occupation of the orbitals in ferrocene.

2.2 Ferrocene geometry and dissociation

In a previous computational project[26], I evaluated different functionals and basis sets to investigate the geometry and ring dissociation of FeCp_2 in the gas phase. The evaluated functionals included the density functional theory-hybrids B3LYP[27, 28] ($\approx 20\%$ Hartree-Fock exchange)[29], MO6-2X[30] ($\approx 54\%$ Hartree-Fock exchange), and the DFT functional PBE[31, 32]. In addition, various basis sets for the B3LYP functional were evaluated, including Pople-type[33], LANL2DZ with Los Alamos National Laboratory 2 double-zeta effective core potential [34] (ECP), and Karlsruhe[35] basis sets. Mixed basis sets were also employed, using the Pople-type basis set on C and H atoms with the LanL2DZ or Karlsruhe basis set on Fe. Furthermore, I investigated the inclusion of Grimme’s dispersion correction (gd3)[36]. The relevant results from the previous study[26] are compiled in Appendix D.

Results showed that using the B3LYP functional with dispersion correction and a mixed basis set consisting of def2tzvp for iron and 6-311G(2df,2pd) for other atoms produced reliable values for conformation energy difference, bond lengths, and reaction enthalpies in close agreement with experimental and theoretical values. The B3LYP functional performed better than the MO6-2X and PBE functionals. The B3LYP functional has been previously shown to produce geometrical values that closely match experimental results[25, 37]. The calculated energy difference between the eclipsed and staggered conformations was found to be -2.2 kJ/mol, with the eclipsed conformation being slightly lower in energy, consistent with experimental[38, 39] and previous computational[24, 40, 41] findings. The low rotation barrier allows both conformations to occur in the gas phase[18, 40, 42]. The standard enthalpy of formation for the reaction $\text{Fe} + 5 \text{C}_2\text{H}_2 \longrightarrow \text{FeCp}_2$ was calculated to be $\Delta_r H^0 = -1305$ kJ/mol for the eclipsed conformer. This value differed by only 22 kJ/mol from the value of -1327 kJ/mol calculated from theoretical values.

The ferrocene dissociation of one and two rings was examined by scanning the bond distance between the iron and the ring center. Asymmetrical dissociation was energetically favored, allowing an intact resonance structure in the remaining Cp^- ring. When one of the rings moved outwards during asymmetric dissociation, while still at a close distance, the iron moved to even out the distance to the rings. At long enough distances, the iron started to move closer to the retained ring, in alignment with experimental data[43]. As one of the Cp^- rings leaves, the electrostatic attraction and hence the distance and dissociation energy between the iron and the remaining Cp^- ring should increase. This has been shown in an experimental study, where the dissociation of the second ring was 123 kJ/mol less energetically favourable[43]. Dissociation of the rings caused the complex to change from a low (singlet) to a high (quintet) state, suggesting a spin change is necessary

for dissociation. Figures 9 and 10 show the respective steps of the symmetric and asymmetric scan, where the end structure is the structure obtained when the scan ended.

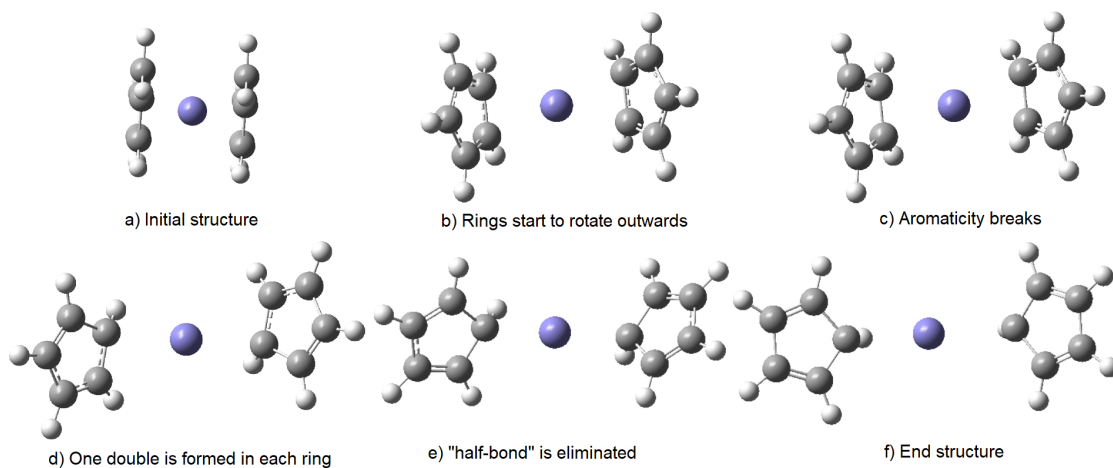


Figure 9: The decomposition steps of the symmetric scan.

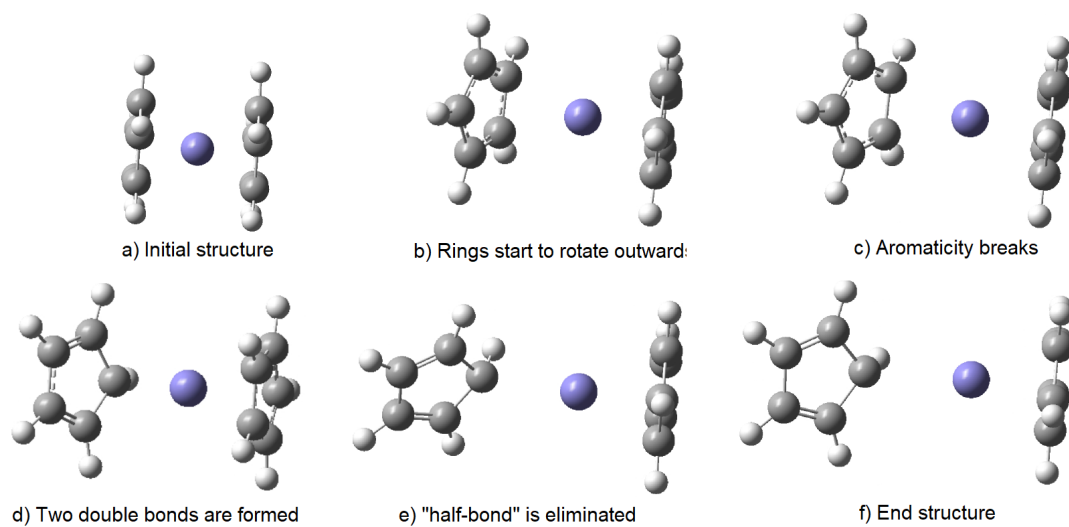


Figure 10: The decomposition steps of the asymmetric scan.

2.3 Ferrocene adsorption on surfaces

The adsorption of ferrocene has been of interest to numerous researchers, and several experimental and theoretical studies have been conducted previously. Deposition of ferrocene requires low temperatures as it readily desorbs from surfaces. Ferrocene has been found to adsorb associatively or dissociatively on various cold surfaces, such as Ag(100)[44–47], Cu(111)[44, 48, 49], Pt(111)[50, 51], and Au(111)[52]. The adsorption of substituted ferrocene has also been studied on Ag(111) [53, 54], in which the substitution atoms bind to the surface. However, to my knowledge, pure ferrocene adsorption on Ag(111) has not been studied.

Silver is an fcc material. The (111) surface of an fcc material has four adsorption sites; 1) on top, 2) hcp hollow, 3) fcc hollow, and 4) bridging positions (Figure 11). The first three correspond to putting the adsorbate directly above one of the crystal structure’s top-layer, second-layer, or third-layer atoms. The bridging position is the site precisely in between two top-layer atoms.

Ferrocene can adsorb vertically and horizontally (Figure 12). Vertical adsorption is generally considered a π -stacking interaction between the Cp^- ring’s π -system and the surface. Cp^- rings and benzene share similarities in being geometrically flat and aromatic. Adsorption, where the conjugated carbon-hydrogen ring lies flat on the surface, has been found previously for benzene on various surfaces[55, 56]. On Ni(111), ben-

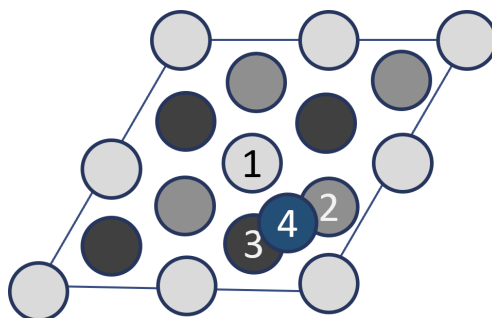


Figure 11: Schematic picture of the adsorption sites of the (111) surface of an fcc material; on-top (1), hcp hollow (2), fcc hollow (3), and bridging (4) position. The light gray atoms are the top-layer atoms, the middle-dark gray are the middle-layer atoms, and the dark gray are the bottom-layer atoms.

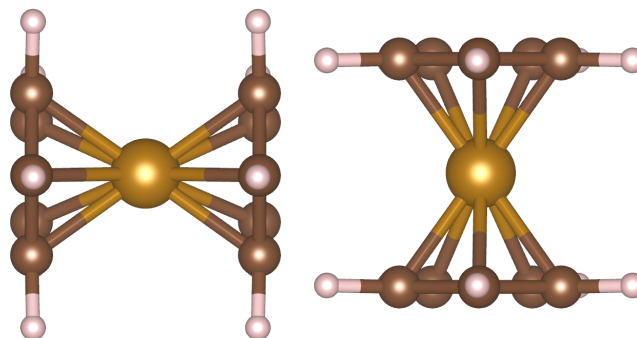


Figure 12: Horizontal (left) and vertical (right) adsorption geometry of ferrocene. Fe, C, and H atoms are yellow, brown, and beige, respectively.

zene adsorbs $1.91(\pm 0.04)$ Å above the surface[55] at the favourable hcp hollow and bridging adsorption sites[55, 56]. Another study has found that the hcp-hollow site is most energetically favourable for the adsorption of Cp^- on Ni(111)[56].

Ferrocene has been shown to adsorb associatively in a vertical geometry on Ag(100)[44–47] and horizontal geometry on Cu(100)[44]. The difference in adsorption is attributed to the distance between the surface atoms, with the Cu-Cu bond length matching that of two adjacent hydrogens of the Cp^- ring, enabling a chelating interaction between the two adjacent hydrogens and two surface copper atoms, with the Cu-H bonds breaking and regenerating at a rapid rate.[44] On Ag(100), desorption is the preferred process over decomposition. Partial fragmentation without desorption could be obtained by synchrotron UV-radiation, resulting in the retention of more strongly chemisorbed fragments on the surface. [45, 46] It has also been found that heating a physisorbed ferrocene leads to ligand dissociation, forming immobile surface-bound Cp radicals ($\text{C}_5\text{H}_5^\bullet$). Cyclopentadienes (C_5H_6), however, were found to be mobile on the surface.[57]

Moreover, ferrocene has been found to adsorb in a sequence of vertical and horizontal geometries on Cu(100)[48] and Cu(111)[48, 49] surfaces, with non-covalent interactions between the Cp^- rings[48]. Ferrocene has also been found to adsorb vertically on Cu(111) with a slight tilt relative to each other, attributed to steric repulsion of the H-atoms[58]. It has also been determined that vertically physisorbed ferrocene on Cu(111) can undergo dissociation of one of the Cp^- rings upon a barrier-less approach of a Fe atom, leading to the formation of surface-bound and gas-phase FeCp complexes viable for further reactions [49].

Dissociative ferrocene adsorption has been determined on Au(111) [52] and Pt(111)[50]. On Au(111), two layers formed of FeCp_2 and FeCp complexes at the bottom and Cp^- rings at the top.[52] On Pt(111), a layer of Cp^- rings formed. At high exposures, ferrocene could replace the fragments on the surface. [50]

Ferrocene adsorption on Pt(111) near a step-edge[51] has shown both vertical physisorption and horizontal chemisorption, the latter slightly favoured on a flat surface but very similar in energy close to a step edge. Chemisorption occurs through an initial C-Pt bond, allowing for an H shift from C to Fe to the surface and a simultaneous Fe-Pt bridge formation. Ferrocene and H can migrate to the step-edge, where the H can rebind to Fe and open the sandwich structure leading to the dissociation of the bottom Cp^- ring from Fe and the rebinding of H to the Cp^- ring, achieving the lowest energy structure. Complete dissociation was reached by migrating the top Cp^- ring away from Fe, resulting in a slightly higher energy end-structure (+0.23 eV).

To conclude, the adsorption of ferrocene is complex, depending on the surface, temperature, and energy source. Further experimental and theoretical investigations are necessary to understand the behavior in the new CVD approach.

3 Quantum Chemical Methodology

3.1 Quantum Chemistry

3.1.1 The Schrödinger equation and the many body problem

Quantum chemistry (QC) applies quantum mechanics to chemical systems to predict chemical behaviour at the atomic level. At the heart of QC lies the Schrödinger equation, providing a means to determine the wave function Ψ of a system, from which many properties of the chemical species can be extracted[59]. The solution to the time-independent, non-relativistic Schrödinger equation (Eq. 1) yields the total energy (E) and wave function (Ψ), which corresponds to the eigenvalues and eigenfunctions of the Hamiltonian operator (\hat{H}), respectively.

$$\hat{H}\Psi = E\Psi \quad (1)$$

The Hamiltonian operator is a differential operator representing the total energy of a system. The total energy consists of the kinetic energy, a sum of the kinetic energy of the electrons \hat{T}_e and the nuclei \hat{T}_n , and the potential energy, a sum of the electron-nuclei \hat{V}_{ne} , electron-electron \hat{V}_{ee} , and nuclei-nuclei \hat{V}_{nn} interaction. In atomic units, the Hamiltonian can be expressed as in Eq. 8. Here, i and j span over N electrons, and A and B span over M nuclei. M_A is the mass of nucleus A , R_{AB} and r_{ij} are the distance between nucleus A and B , and electrons i and j , respectively, Z_A and Z_B denote the particle charge of species A and B , and the Laplacian operator $\nabla^2 = \frac{\delta^2}{\delta x^2} + \frac{\delta^2}{\delta y^2} + \frac{\delta^2}{\delta z^2}$ with respect to the cartesian coordinates of the respective species A and i .

$$\begin{aligned} \hat{H} &= \hat{T}_n + \hat{T}_e + \hat{V}_{ne} + \hat{V}_{nn} + \hat{V}_{ee} = \\ &= -\frac{1}{2} \sum_{A=1}^M \frac{1}{M_A} \nabla_A^2 - \frac{1}{2} \sum_{i=1}^N \nabla_i^2 - \sum_{i=1}^N \sum_{A=1}^M \frac{Z_A}{r_{Ai}} + \sum_{A=1}^M \sum_{B>A}^M \frac{Z_A Z_B}{R_{AB}} + \sum_{i=1}^N \sum_{i>j}^N \frac{1}{r_{ij}} \end{aligned} \quad (2)$$

Quantum chemical methods rely heavily on the Born-Oppenheimer approximation[60], presuming the nuclei to be stationary relative to the fast-moving electrons ($\hat{T}_n=0$). This approximation allows for separating and solving the Schrödinger equation separately in terms of a nuclear and an electronic part. Generally, QC methods utilise the electronic Hamiltonian (\hat{H}_e) (Eq. 3) to calculate the electronic wave function Ψ_e and the electronic energy E_e (Eq. 4). It follows that the nuclear energy is the nuclear interaction energy ($E_n = \hat{V}_{nn}$), and the total system energy E_{tot} sums by the electronic energy E_e and the nuclear energy E_n (Eq. 5).[59, 61]

$$\hat{H}_e = \hat{T}_e + \hat{V}_{ne} + \hat{V}_{ee} = -\frac{1}{2} \sum_{i=1}^N \nabla_i^2 - \sum_{i=1}^N \sum_{A=1}^M \frac{Z_A}{r_{Ai}} + \sum_{i=1}^N \sum_{i>j}^N \frac{1}{r_{ij}} \quad (3)$$

$$\hat{H}_e \Psi_e = E_e \Psi_e \quad (4)$$

$$E_{tot} = E_e + E_n \quad (5)$$

Many-electron species present a many-body problem, which makes it impossible to solve the Schrödinger equation analytically[59]. Quantum chemical methods use approximations and subsets of functions to obtain numerical solutions with varying levels of accuracy, balanced against computational cost, and speed. Hartree Fock (HF) and Density Functional Theory (DFT) are two widely used methods of calculating electronic energy, using functionals of the wavefunction and electron density, respectively. Choosing a method also involves the selection of a basis set, a set of functions that span the vector space of the orbitals approximating the electronic wave function. A complete basis set includes an infinite number of basis functions, which is not computationally feasible. Instead, only a certain set of basis functions are included. In general, larger basis sets give more accurate but more computationally demanding approximations. Two examples of basis sets commonly used in molecular and solid state modelling, respectively, are molecular orbitals (MOs) constructed from a Linear Combination of Atomic-type Orbitals (LCAO), and plane waves constructed from Fourier expansion of the periodic part of the wave function of the solid material.

3.1.2 The Hartree-Fock method

The HF method[62, 63] is a central part of QC, using one-electron equations, a Slater determinant, and an average potential to solve the Schrödinger equation.

The electronic Schrödinger equation of an N-electron molecule can be approximated by a product of N three-dimensional single electron equations, yielding the simplest Hartree approximation of the electronic Schrödinger equation (Eq. 6), where \mathbf{r}_i describes a three-dimensional electron vector, and $\psi_i(\mathbf{r}_i)$ is termed an orbital. Molecular orbitals (Eq. 7) can be approximated as a linear combination of n atomic-type orbitals (Φ) with a coefficient (c_{ij}) describing the contribution of each AO to the molecular orbital, which is the LCAO approach. The set of AOs used to approximate the MOs is the basis set, and improved accuracy can be obtained by including more functions in the basis set, at the cost of increased computational complexity.

$$\hat{H}_e \Psi(r_1, r_2, \dots, r_N) = E_e \Psi(r_1, r_2, \dots, r_N) = E_e \prod_{i=1}^N \Psi_i(\mathbf{r}_i) \quad (6)$$

$$\Psi_i(\mathbf{r}_i) = \sum_{j=1}^n c_{ij} \Phi_j(r) \quad (7)$$

Under the assumption of no electron interaction ($\hat{V}_{ee} = 0$), the electronic Hamiltonian is a sum of one-electron Hamiltonians (Eq. 8), where $\hat{h}(i)$ is a one-electron Hamiltonian, or a core Hamiltonian, which includes the kinetic energy and nuclei-electron interaction energy experienced by the electron (Eq. 9).

$$\hat{H}_e = \sum_{i=1}^N \hat{h}(i) \quad (8)$$

$$\hat{h}(i) = -\frac{1}{2}\nabla_i^2 - \sum_{A=1}^M \frac{Z_A}{r_{Ai}} \quad (9)$$

For describing the interaction between electrons, the HF approximation introduces an averaged potential experienced by one electron due to the repulsive forces from all other $N - 1$ electrons, called the Hartree Fock potential $\hat{V}_{HF}(i)$ (Eq. 10). It contains sums of coulomb interactions (\hat{J}_{ij}) and exchange interactions (\hat{K}_{ij}). \hat{J}_{ij} is the interaction that an electron positioned at \vec{r}_i experiences in the presence of another electron in spin-orbital χ_j (Eq. 11), where a spin-orbital is a product of a spatial orbital and one of the two orthonormal spin functions. \vec{x}_i is a product of the spatial coordinates \vec{r}_i and spin coordinates \vec{s}_i . \hat{K}_{ij} , defined as in Eq. 12, accounts for the Pauli principle, which states that two electrons cannot have the same quantum numbers.

$$\hat{V}_{HF}(i) = \sum_{j=1}^N \hat{J}_{ij} - \hat{K}_{ij} \quad (10)$$

$$\hat{J}_{ij}(\vec{x}_1) = \int \frac{|\chi_j(\vec{x}_2)|^2}{|\vec{r}_1 - \vec{r}_2|} d\vec{x}_2 \quad (11)$$

$$\hat{K}_j(\vec{x}_1)\chi_i(\vec{x}_1) = \int \frac{\chi_j^*(\vec{x}_2)\chi_i(\vec{x}_2)}{|\vec{r}_1 - \vec{r}_2|} d\vec{x}_2 \chi_j(\vec{x}_1) \quad (12)$$

Following this, the Hamiltonian of interacting electrons can be described as the Fock operator $\hat{f}(i)$, a sum of the one-electron Hamiltonian of an independent electron and the HF potential (Eq 13). Eq. 14 defines the Hartree Fock equations, used to find the lowest energy of the orbitals. ϵ_i is the Langmuir multiplier, labelled the orbital energy.[59, 64]

$$\hat{f}(i) = \hat{h}(i) + \hat{V}_{HF}(i) \quad (13)$$

$$\hat{f}_i \chi_i = \epsilon_i \chi_i \quad (14)$$

In the HF method, the N normalised single electron wave functions build up a normalised, antisymmetric Slater determinant Φ_{SD} (Eq. 15, showing the diagonal elements). The expectation value $\langle \Psi^* | \hat{H} | \Psi \rangle$ is minimised by utilising the variational method to vary the spin orbitals that are constrained to being orthonormal.

As the value of a spin-orbital depends on the value of all the other spin orbitals, the HF method utilises the self-consistent field (SCF) theory to solve the Schrödinger equation, which is an iterative process to find the lowest energy of the system. The SCF cycle involves an initial guess of the many-particle wave function used to calculate the kinetic and potential energy operators and the Hamiltonian. Using the Hamiltonian, the Schrödinger equation can be solved to determine the wave function used as an initial guess in a new loop. By repeating the cycle until meeting a convergence criterion of the wave function, the final wave function and solving of the Schrödinger equation give the total energy, called the HF energy E_{HF} (Eq. 16).

$$\Phi_{SD} = \frac{1}{\sqrt{N!}} \det\{\chi_1(x_1) \dots \chi_N(x_N)\} \quad (15)$$

$$\hat{H}\Phi_{SD} = E_{HF}\Phi_{SD} \quad (16)$$

The variational principle states that the calculated energy will always be higher than or equal to the ground state energy, introducing the correlation energy defined as the difference between the ground state energy and the HF energy ($E_C = E_0 - E_{HF}$). The correlation energy mainly arises from the repulsion of electrons, which is treated in an average fashion by the HF potential, and thus is not accounted for correctly, limiting the accuracy of the HF method. Different methods have been proposed to account for the correlation, such as the wave-function based Møller Plesset (MP2), configuration interaction (CI), quadratic CI (QCI), and coupled cluster (CC) approaches. Another method that uses an approximate correlation treatment is the DFT approach. DFT/HF hybrids are DFT functionals that include a part of HF exchange, which usually makes the functional more accurate.[59, 64]

3.2 Density Functional Theory

3.2.1 The theorems of Hohenberg and Kohn

Density Functional Theory is a method with many analogies to the HF method. However, In DFT, the ground state electronic energy is a unique functional of the ground state electron density (ρ_0), as proven by Hohenberg and Kohn[65]. In Eq. 22, given from the first theorem of Hohenberg and Kohn, $T[\rho_0]$ is the kinetic energy, $E_{ee}[\rho_0]$ the electron-electron interaction energy, and $E_{Ne}[\rho_0]$ is the nuclei-electron interaction energy. $E_{ee}[\rho]$ consists of a Coulomb part $J[\rho_0]$ and a non-classical part $E_{ncl}[\rho_0]$ (Eq. 18).

$$E[\rho_0] = T[\rho_0] + E_{ee}[\rho_0] + E_{Ne}[\rho_0] \quad (17)$$

$$E_{ee}[\rho_0] = J[\rho_0] + E_{ncl}[\rho_0] \quad (18)$$

The ground state density correlates to only one system with specific N , R_A , and Z_A . Therefore, the expression divides into system-dependent and system-independent contributions (Eq. 19). The nuclei-electron interaction term E_{Ne} depend on the system, and the kinetic energy and electron-electron interaction terms are said to be system-independent since they are independent of N , R_A , and Z_A . The $T[\rho]$ and $E_{ncl}[\rho]$ parts are unknown.[59]

$$E[\rho_0] = \underbrace{E_{Ne}[\rho_0]}_{\text{system dependent}} + \underbrace{T[\rho_0] + J[\rho_0] + E_{ncl}[\rho_0]}_{\text{system independent}} \quad (19)$$

3.2.2 The Kohn-Sham approach

As mentioned earlier, the kinetic energy of the electrons is unknown. To make the kinetic energy computationally feasible, Kohn and Sham[66] proposed an approach to calculating as much as possible of the kinetic energy explicitly and approximating the rest, introducing the $T_s[\rho_0]$ term for the kinetic energy of non-interacting particles and the exchange-correlation energy E_{xc} (Eq. 21). E_{xc} consists of the Kohn-Sham kinetic energy $T_C[\rho_0]$ approximating the remainder of the kinetic energy (defined as $T[\rho_0] - T_s[\rho_0]$), and $E_{ncl}[\rho_0]$ (defined as $E_{ee}[\rho_0] - J[\rho_0]$). E_{xc} then contains everything unknown.

$$T[\rho_0] = T_s[\rho_0] + E_{xc}[\rho_0] \quad (20)$$

$$E_{xc}[\rho_0] = (T[\rho_0] - T_s[\rho_0]) + (E_{ee}[\rho_0] - J[\rho_0]) = T_C[\rho_0] + E_{ncl}[\rho_0] \quad (21)$$

Finally, the energy functional is the sum of the nuclei-electron and electron-electron interactions, the kinetic energy of non-interacting particles, and the unknown exchange-correlation energy (Eq. 22).

$$E[\rho_0] = E_{Ne}[\rho_0] + J[\rho_0] + T_s[\rho_0] + E_{xc}[\rho_0] \quad (22)$$

By introducing an effective potential of an electron V_{eff} , the Hamiltonian of a non-interacting electron can be described (Eq. 24). This Hamiltonian is called the Kohn-Sham (KS) operator (\hat{f}_{KS}). V_{eff} contains the Coulombic forces of the electron-nuclei and electron-electron interaction, as well as an unknown exchange-correlation potential V_{xc} , defined as the derivative of E_{xc} with respect to ρ ($\delta E_{xc}/\delta \rho$).

$$\hat{f}_{KS} = -\frac{1}{2}\nabla_i^2 + V_{eff}(\mathbf{r}_i) \quad (23)$$

$$V_{eff}(\mathbf{r}) = -\sum_A^M \frac{Z_A}{|\mathbf{r}_1 - \mathbf{R}_A|} + \int \frac{\rho_0(r_2)}{|\mathbf{r}_1 - \mathbf{r}_2|} d\mathbf{r}_2 + V_{xc}(r_1) \quad (24)$$

From here, the Schrödinger-like Kohn-Sham equation of a non-interacting electron can be introduced (Eq. 25). The solving of these one-electron Kohn-Sham equations involves an iterative SCF method by using a trial density to obtain the

V_{eff} and using it to get the electron density of the one-electron Kohn-Sham orbitals with energy ϵ . As in the HF method, this is done by using a Slater determinant and exploiting the variational principle, using a trial density $\tilde{\rho}$ under the constraints that it is non-negative $\tilde{\rho}(\vec{r}) \geq 0$ and that the integral of the density over all space is equal to the number of electrons N in the system $\int \tilde{\rho}(\vec{r}) d\vec{r} = N$. The SCF loop is repeated until a set convergence criterion is satisfied. Figure 13 illustrates a flowchart scheme of the Kohn-Sham SCF procedure.

$$\hat{f}_{KS}\Psi_i = \epsilon_i\Psi_i \quad (25)$$

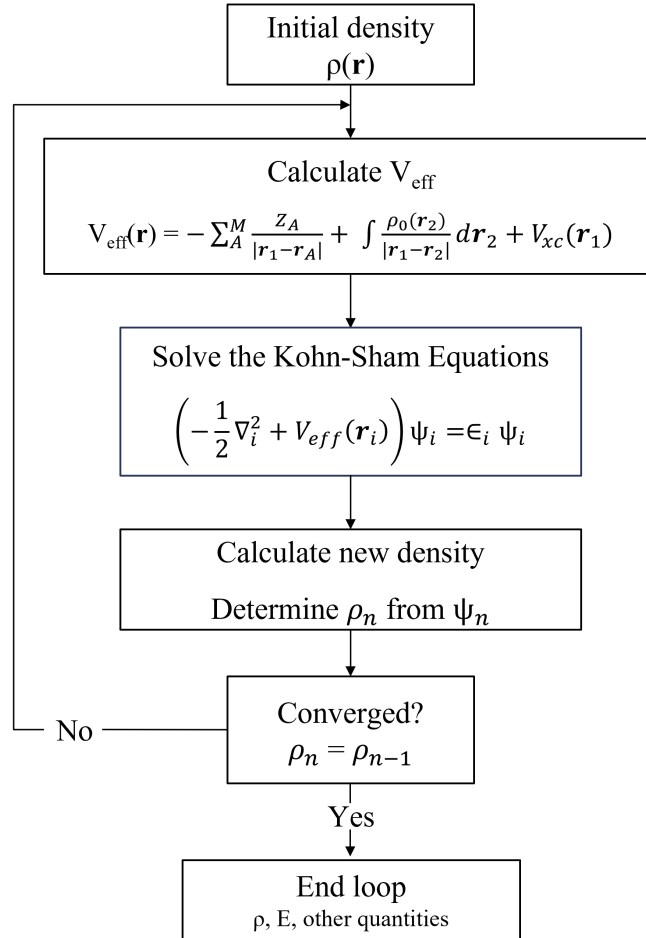


Figure 13: Flow scheme illustration of the Kohn-Sham self-consistent loop.

The Kohn-Sham approach thus makes the computation of the kinetic energy of the non-interacting electrons feasible. Next, a method of approximating the unknown exchange-correlation term E_{xc} is required. The computational accuracy heavily depends on the exchange-correlation functional.

3.2.3 Exchange-correlation functionals

To approximate the exchange-correlation term, various functionals have been introduced, such as the Local Density Approximation (LDA), Generalised Gradient Approximation (GGA), meta-GGA, and hybrid GGA.

The LDA assumes a uniform electron gas, where E_{xc} depends only on the local electron density at position $\rho(\mathbf{r})$ and is equal to the sum of the exchange-correlation energy per particle ($\varepsilon_{xc}[\rho(\mathbf{r})]$), positioned at $\rho(\mathbf{r})$ (Eq. 26), weighted after the probability that it is an electron at position $\rho(\mathbf{r})$. The LDA approach has shown valuable results for geometry and harmonic frequency calculations. However, it generally delivers poor energetic results.[59]

$$E_{xc}^{LDA}[\rho(\mathbf{r})] = \int \rho(\mathbf{r})\varepsilon_{xc}[\rho(\mathbf{r})]d\mathbf{r} \quad (26)$$

The GGA approach introduces, through a Taylor expansion series of the uniform electron density from the LDA method, a charge density gradient to account for the non-homogeneity of the electron gas (General form, Eq. 27). The exchange-correlation is often split into exchange E_x and correlation E_c parts. Different GGA method uses different integrands f and gradients ∇ . A meaningful GGA functional is PBE, proposed by Perdew, Burke, and Ernzerhof[31].

$$E_{xc}^{GGA}[\rho(\mathbf{r})] = \int \rho(\mathbf{r})f[\rho(\mathbf{r}), \nabla\rho(\mathbf{r})]d\mathbf{r} \quad (27)$$

A hybrid functional incorporates a contribution of exact HF exchange into the DFT functional. B3LYP is a DFT/HF hybrid including 20% HF exchange and 80% DFT exchange[29], tuned for accurate yet efficient calculations. It includes Becke's 3-parameter exchange functional with both LDA and GGA exchange and the Lee-Yang-Parr correlation functional. This thesis utilises the DFT/HF hybrid B3LYP for molecular modelling and the pure DFT functional PBE for solid-state modelling.

For weakly interacting systems, accurately describing dispersion forces is crucial, something where both LDA and GGA fail. In such cases, the addition of dispersion correction can be made to the functional. In this thesis, I utilise the D3 version of Grimme's empirical dispersion correction (gd3)[36].

3.3 Statistical mechanics

In DFT, the calculations are generally performed at 0 K. By combining the results from quantum mechanics with statistical mechanics, one can get thermodynamic information, providing a way of comparing the obtained results with experimental data. Statistical mechanics, therefore, constitute an important link between quantum mechanics and the real world.

Central to statistical mechanics is the partition function q (Eq. 28), where k_B is Boltzmann's constant and T is the temperature. The molecular partition function is defined as the sum over all quantum energy states 0, 1, ..., n , with corresponding energies $\epsilon_0, \epsilon_1, \dots, \epsilon_n$, that a molecule may exist in, as described by the Boltzmann distribution. The probability of the molecule being in state i can therefore be explained as the number of molecules in state i (N_i) divided by the total number of molecules in all states (N), which is equal to the partition function (Eq. 29).

$$q = \sum_{i=1}^N e^{-\frac{\epsilon_i}{k_B T}} \quad (28)$$

$$\frac{N_i}{N} = \frac{e^{-\frac{\epsilon_i}{k_B T}}}{q} \quad (29)$$

The partition function can be used to directly derive the internal energy U and the Helmholtz free energy (A) and from them several other important thermochemical properties such as entropy (S), enthalpy (H), and Gibbs free energy (G) (Eqs. 30-34).

$$U = k_B T^2 \left(\frac{\partial \ln(q)}{\partial T} \right)_V \quad (30)$$

$$A = -k_B T \ln(q) \quad (31)$$

$$S = \frac{U - A}{T} = k_B T \left(\frac{\partial \ln(q)}{\partial T} \right)_V + k_B \ln(q) \quad (32)$$

$$H = U + PV = k_B T^2 \left(\frac{\partial \ln(q)}{\partial T} \right) + k_B T V \left(\frac{\partial \ln(q)}{\partial V} \right)_T \quad (33)$$

$$G = H - TS = k_B T V \left(\frac{\partial \ln(q)}{\partial T} \right)_V - k_B T \ln(q) \quad (34)$$

For an isolated molecule, the total energy can be expressed as a sum of the translational (ϵ_i^T), rotational (ϵ_i^R), vibrational (ϵ_i^v), and electronic contributions (ϵ_i^E), (Eq. 35). Following, the partition function can be described as a product of the partition functions of the different contributions (Eq. 36), simplifying computations.

$$\epsilon_i = \epsilon_i^T + \epsilon_i^R + \epsilon_i^v + \epsilon_i^E \quad (35)$$

$$q_i = q_T q_R q_v q_E \quad (36)$$

3.4 Quantum Chemical modelling

3.4.1 Energy Optimisation and Vibrational analysis

Performing a geometry optimisation of a system means finding the geometric structure that corresponds to a minimum on the potential energy surface (PES). The PES portrays the potential energy as a function of a molecule’s atomic positions, where a minimum is where the partial derivatives are zero. A guess of the initial molecular geometry initiates the geometry optimisation, the iterative investigation of the structure, and its corresponding electronic potential energy.[61]

Molecules always vibrate around their positions. These vibrations occur at specific frequencies, and each frequency corresponds to a motion. Near the equilibrium, the vibrations can be considered essentially harmonic.[61] A vibrational analysis[67] refers to calculating the harmonic frequencies of vibrations. The vibrational frequencies yield spectroscopy information. Paired with statistical mechanics, thermochemical and kinetic data can be obtained. From the different frequencies, the entropy (S), enthalpy (H), Gibbs free energy (G), and heat capacity (c_v) can be calculated using the partition function[68].

The vibrational analysis involves the evaluation of the equilibrium structure’s potential energy second derivatives with respect to the cartesian coordinates.[59] The second derivatives line up in a Hessian matrix, which is diagonalised to determine the frequencies and the corresponding normal modes. The principal axes of inertia are determined to separate the rotational and translational modes from vibrational modes. The rotational and translational frequencies should be close to zero, and the occurrence of negative frequencies indicates the optimised geometry corresponds to a transition state.[67]

3.4.2 Molecular Quantum Chemistry Modelling

Gaussian 16 is a code used for electronic structure modeling. The molecular modelling in this thesis has been performed using the DFT/HF B3LYP functional. The used basis set was a mixed basis set with def2tzvp on the Fe atom and the 6-311G(2df,2pd) basis set on the C and H atoms.

The 6-311G(2df,2pd) Pople basis set uses six basis functions to describe the core electrons. As the valence electrons are more critical for bonding and chemical reaction, models typically use more basis functions for the valence electrons compared to the core electrons to increase accuracy while keeping a low computational cost. The valence basis set consists of three basis functions to form a so-called split-valence triple-zeta basis set, making it a more extensive basis set and increasing accuracy compared to a minimal or double-zeta split valence basis. The primitive functions are of Gaussian type. During chemical bonding, the positive charge of the nucleus in adjacent atoms distorts the atomic orbitals, a

phenomenon called polarisation. It is meaningful to account for the polarisation effects in polarised molecules by adding polarisation functions, which in practice means adding functions of higher orbital quantum numbers to the basis set. In this basis set, 2p1d polarisation functions are added on H and 2d1f polarisation on other atoms.[69] The def2tzvp basis set is an Ahlrich basis set with a triple-zeta valence and 1p polarisation on H, 2d1f on C, and 1p1d1f on Fe.

3.4.3 Periodic calculations for solid-state quantum chemical modelling

The Vienna Ab-Initio Simulation Package (VASP) is a quantum chemical code used for computing the quantum mechanical properties of materials. The solid-state calculations in this thesis have been performed using the DFT functional PBE implemented in the VASP software.

The modelling of solid systems differs from individual molecular species and is typically approached using either a cluster or a periodic model [70]. When surfaces are to be studied, the so-called slab approach involves modelling the crystal unit cell as a bulk structure, expanding it, cutting it along a direction, and adding a vacuum in the z-direction to obtain a slab model. The vacuum must be large enough to eliminate interaction between the top of the cell and the bottom of the next cell image. The orientation of crystal growth can be studied by cutting the crystal along different surfaces and comparing their surface energies.

Crystals have a periodic structure with a regular stacking pattern and identical properties in equivalent points. [71, 72] The crystal lattice is the characteristic three-dimensional crystal shape. The unit cell is the smallest unit of the crystal symmetry, from which the full crystal lattice can be formed through translation only. The unit cell is characterized by lattice parameters \mathbf{a} , \mathbf{b} , \mathbf{c} , and corresponding angles α, β, γ [70]. In solid-state computations, the crystal unit cell can be repeated under periodic boundary conditions (PBCs)[72]. Bloch's functions (Eq. 37) describe the relationship between the wave function of equivalent points in the crystal, where the wave functions are constrained to satisfy Bloch's theorem [70]. The periodic function u has the same periodicity as the crystal, \mathbf{n} is the band index, \mathbf{k} is the wave vector, \mathbf{r} is an arbitrary positional vector, e is Euler's number, i is the imaginary unit and \mathbf{R} is the lattice vector, consisting of the unit cell vectors. The periodic function can be expanded as a Fourier series of plane waves that run over the reciprocal lattice vectors G (Eq. 38).

$$\psi_{\mathbf{n}\mathbf{k}}(\mathbf{r}) = u_{\mathbf{n}\mathbf{k}}(\mathbf{r})e^{i\mathbf{k}\mathbf{r}} \quad (37)$$

$$u_{\mathbf{n}\mathbf{k}}(\mathbf{r}) = u_{\mathbf{n}\mathbf{k}}(\mathbf{r}+\mathbf{R})$$

$$u_{\mathbf{n}\mathbf{k}}(\mathbf{r}) = \sum_G C_{G\mathbf{n}\mathbf{k}} \cdot e^{iG\cdot\mathbf{r}} \quad (38)$$

The Fourier expansion of the periodic part of the wave function provides an infinite set of one-electron wave functions represented by plane waves. To obtain a feasible basis set, the plane waves of the Kohn-Sham orbitals are truncated by the cutoff energy (Eq. 39) including only waves with smaller kinetic energy than the cutoff. Larger cutoff energy yields a more extensive basis set and typically higher accuracy but is more computationally demanding.

$$\frac{1}{2}|G + k|^2 < E_{cutoff} \quad (39)$$

It is computationally efficient to use a plane wave basis set for periodic calculations. However, close to the nucleus the wavefunctions oscillate rapidly and become difficult to describe. The core electrons do not usually contribute to reactions, why a pseudopotential can replace the potential of each core electron to describe them more accurately and decrease the computational cost. The Project Augmented-Wave pseudopotentials (PAW)[73] yield fast and accurate results and are used in this thesis, as implemented in the VASP software.

All Bloch vectors \mathbf{k} considered as solutions to the wave function must be constrained to lie within the first Brillouin zone, the primitive cell in reciprocal space. The Bloch vectors form an infinite set, which must be simplified for feasible computations. Close points in reciprocal space have approximately the same wave functions, allowing for a finite, weighted set of k-points to be formed that is used to sample the first Brillouin zone. This set consists of Bloch vectors related by symmetry and is called a k-point mesh. Typically, it is preferred to use odd-numbered k-points to include the central Γ point of the first Brillouin zone in the k-point mesh. Using more k-points typically increases accuracy, but significantly increases the computational demand.

To determine a reliable and computationally efficient method for a system, the properties should be converged with respect to cutoff energy and k-points. The general guidance is to use the number of k-points inversely proportional to each length of the unit cell and use a cutoff energy higher than the minimum cutoff energy specified for the elements.

3.4.4 Bulk characterisation

Different parameters can be calculated and compared to experimental data to validate the reliability of the computational method and characterise the periodic system. Such parameters include the lattice parameters, cell volume, bond lengths and angles, and cohesive energy. The cohesive energy is the energy required to remove an atom from a crystal into the gas phase and gives a measure of the stability of the crystal.

3.4.5 Surface energy

The surface energy is the excess energy at the surface, compared to the bulk, and gives information about the stability of the surface, where a lower value indicates surface stability. This can be compared to experimental results, and it can also be utilised to investigate different surfaces of the material to see which is the lowest in energy. The surface of the lowest energy should correspond to the preferred growth direction.

3.4.6 Adsorption energy

Surface chemistry can involve various reactions, such as adsorption, diffusion, and surface reactions. Adsorption occurs when a molecule adheres to the surface, with the adsorbate being the adsorbing species and the adsorbent being the material it adheres to. The strength of the adsorption can vary, as indicated by the adsorption energy, the energy decrease when an adsorbate adheres to the adsorbent. Negative adsorption energies indicate the adsorption is energetically favourable, and that energy is released upon adsorption, with more negative values indicating stronger attachment. Physisorption occurs mainly due to van der Waals interactions, whereas chemisorption involves the formation of chemical bonds. Slightly negative adsorption energy generally signifies physisorption, whereas more negative values signify the creation of a chemical bond.

3.4.7 Density of states analysis

The electronic density of states (DOS) analysis provides a way of investigating electronic structure, by plotting the density of states as a function of energy, thus giving information about how the electrons occupy the orbitals. In VASP, DOS is calculated by projecting the electron contributions onto atomic orbitals. The DOS can then be analysed to obtain an understanding of the electronic properties of a system.

3.4.8 Bader charge analysis

Bader charge analysis is used to calculate the electron density of atoms, using the code from the Henkelman group.[74] The Bader charge analysis divides molecules into atoms based on charge density using zero flux surfaces. The zero flux surfaces are two-dimensional surfaces for which the charge density corresponds to a local minima perpendicular to the surface. These minima are generally considered to occur between atoms and are therefore used to distinguish the atoms. Enclosed in the Bader volume, Bader charges approximate the atomic charges and can be used to evaluate charge transfers, which gives an indication of the chemical character of atomic interactions.

4 Computational details

The gas phase and surface chemistry of ferrocene, ions, and fragments were investigated using the Gaussian 16 and VASP softwares. The National Academic Infrastructure for Supercomputing in Sweden (NAISS), and the National Supercomputer Centre (NSC) at Linköping University provided the computational resources.

4.1 Gas phase chemistry

Molecules were built using Gaussview 6[75]. The gas phase chemistry calculations were performed using the Gaussian 16 software package[76], utilising the B3LYP[27, 28] DFT/HF hybrid functional with D3-Grimme dispersion correction (gd3)[36] and a mixed basis set with Karlsruhe[35] def2tzvp basis set on the iron atom, and the Pople[33] 6-311G(2df,2pd) basis set on the other atoms, herein referred to as a mixed def2tzvp/6-311G(2df,2pd) basis set. This mixed basis set includes all 96 electrons and 405 functions and has previously been shown to produce reliable results for the computations of FeCp_2 bond lengths, conformation energy differences, and thermochemistry[26]. The study investigated the eclipsed FeCp_2 conformer with D_{5h} symmetry, as this conformer has previously been stated lower in energy than the staggered conformer, both computationally[26, 77] and experimentally[18, 38, 39, 77]. The frequencies and thermochemical properties were calculated under standard conditions, at $T = 298.15$ K and $P = 1$ atm.

4.1.1 Electronic spin states and geometry

Due to the incompletely filled d-orbitals, iron, and its complexes can obtain several close-lying spin states. Therefore, it is important to investigate the electronic spin states to ensure the right spin state and energy of the molecule are used for the accuracy of further calculations on the chemical reactions. The relative energy of different electronic spin states and molecular geometries of FeCp_2 and its FeCp , Fe , and Cp fragments was investigated. A plasma is present during the CVD approach used by Nadhom et al.[15]. Therefore, both neutral and

Table 1: The investigated species ferrocene (FeCp_2), cyclopentadienyliron (FeCp), cyclopentadienyl anion (Cp), and iron (Fe), with associated ions.

FeCp_2	FeCp_2^- , FeCp_2^{2-} FeCp_2^+ , FeCp_2^{2+}
FeCp	FeCp^- , FeCp^{2-} , FeCp^{3-} FeCp^+ , FeCp^{2+} , FeCp^{3+}
Cp	Cp^- , Cp^{2-} , Cp^{3-} Cp^+ , Cp^{2+} , Cp^{3+}
Fe	Fe^- , Fe^{2-} , Fe^{3-} Fe^+ , Fe^{2+} , Fe^{3+}

charged FeCp_2 with up to two negative and positive charges, and both neutral and charged fragments FeCp , Fe , and Cp with up to three positive and negative charges

were considered. All investigated species are compiled in Table 1. The energy of different electronic spin states with multiplicities 1,3,5,7 or 2,4,6,8 was investigated for FeCp₂, FeCp, Cp, and Fe, and respective ions. The electronic energies of all species and multiplicities are compiled in Appendix A, Tables A1-A4. For the lowest-energy electronic spin state, the molecular geometry was investigated regarding Fe-C, C-C, and C-H bond lengths.

4.1.2 Ion formation electronic energies, enthalpies, and Gibbs free energies

The electronic energies, enthalpies, and Gibbs free energies of ion formation were considered for the ions. All ions were calculated using the same mixed basis set as the neutral species. The anions were also calculated using diffuse functions[78] on carbon and hydrogen. The diffuse functions were only added on C and H, as the electronic charge is not expected to distribute on Fe due to its low reduction potential. The enthalpies and Gibbs free energies were obtained using vibrational analysis, as implemented in Gaussian 16 [67].

The electron was treated as a product or reactant for the ion formations. The electronic energies, enthalpies, and Gibbs free energies ($X = E, H, G$) of the formation of ions were calculated consecutively. The first electronic energies, enthalpies, and Gibbs free energies of the ion formation to positive ions were calculated as:

$$X_r^{first} = X_{x+} + X_{e-} - X_{x^{neutral}} \quad (40)$$

The second electronic energies, enthalpies, and Gibbs free energies were calculated as:

$$X_r^{second} = X_{x^{2+}} + X_{e-} - X_{x+} \quad (41)$$

And the third electronic energies, enthalpies, and Gibbs free energies were calculated as:

$$X_r^{third} = X_{x^{3+}} + X_{e-} - X_{x^{2+}} \quad (42)$$

The energies and enthalpies of anion formation were calculated in the same way but with the electron as a product. As an electron is a fermion, it is appropriate to use the Fermi-Dirac statistical mechanics approach for the thermochemistry of the electrons[79], as done by Fifen[80]. The electrons are assumed to be an ideal electron gas at 298.15 K described by a canonical ensemble, where the enthalpy of the electron $H_e = 3.1351$ kJ/mol[80], and Gibbs free energy $G_e = -3.6160$ kJ/mol[80]. The electronic energy of the electron was set to zero, $E_e = 0$ kJ/mol, as an at 0 K should have zero energy.

4.1.3 Ferrocene dissociation

The dissociation of the FeCp_2 molecule and ions FeCp_2^- , FeCp_2^{2-} , FeCp_2^+ , and FeCp_2^{2+} into FeCp , Fe , and Cp and respective ions up to three positive and negative charges were examined. All investigated dissociation reactions are compiled in Appendix C, Table C1. All ions were calculated using the same mixed basis set as the neutral species. The anions were also calculated using diffuse functions on carbon and hydrogen. The reaction energies $\Delta_r E$, enthalpies $\Delta_r H$, and Gibbs free energies $\Delta_r G$ ($X = E, H, G$) were calculated for each species as:

$$\Delta_r X = X_{\text{products}} - X_{\text{reactants}} \quad (43)$$

4.2 Surface chemistry

The adsorption process gives information about the first step in thin film formation. Here, the chemistry of FeCp_2 adsorbing to an $\text{Ag}(111)$ surface was investigated. Modelling of the adsorption requires both modelling of the adsorbent and the adsorbate. Therefore, both the silver crystal, its surface, and the free FeCp_2 molecule were modelled. After this, the adsorption of the FeCp_2 molecule to the crystal surface could be examined. The surface decomposition was investigated for both the vertical and horizontally adsorbed FeCp_2 . All surface calculations were modelled using the VASP 5.4.4 software and projector-augmented wave (PAW) pseudopotentials. The computations utilised DFT, the Perdew-Burke-Ernzerhof (PBE)[31, 32] functional, and a basis set of plane waves. The Brillouin zone was sampled using the Monkhorst-Pack k-point mesh[81]. Different cutoff energies and k-points were used after the convergence of the respective system, to decrease computational cost. The bulk structure was calculated with and without D3-Grimme dispersion correction. The rest of the structures were calculated with dispersion correction. Spin polarization was considered for relevant systems after the assessment of magnetisation.

4.2.1 Bulk silver crystal structure

The crystal Ag fcc bulk structure belonging to the Fm-3m space group was modelled. The initial crystal bulk structure was obtained from the crystallographic data. The initial bulk structure had a volume of 68.1923 \AA^3 with dimensions $4.0855 \times 4.0855 \times 4.0855 \text{ \AA}$. The cut-off energy was set to 450 eV, using $7 \times 7 \times 7$ k-points, after convergence. As silver is a metal, the Methfessel-Paxton smearing with $N=2$ and a width of 0.2 eV was used, ensuring an entropy contribution term below 1 meV/atom. The bulk structure was calculated with and without D3-Grimme dispersion correction and the lattice parameters, cell volume, and Ag-Ag nearest neighbor distance were compared to theoretical and experimental values.

4.2.2 Isolated silver atom

To be able to calculate the cohesive energy, the energy of an isolated silver atom in the gas phase was calculated. To keep the silver atoms from interacting with the image, the atom was set in a box of 20 \AA in all directions. Since only one atom was modelled, the k-points were set to $1 \times 1 \times 1$, and Gaussian smearing was used, with a 0.1 eV smearing width, ensuring an entropy contribution term below 1 meV/atom. Spin polarisation was considered, as the system possessed magnetisation of 1. After convergence of the cutoff, it was set to 450 eV.

4.2.3 Cohesive energy

The cohesive energy was calculated and compared to experimental results. The cohesive energy is the energy required to remove an atom from a crystal into the gas phase and is calculated as:

$$E_{cohesive} = E_{bulk} - N \times E_{atom} \quad (44)$$

Where $E_{cohesive}$ is the cohesive energy, E_{bulk} the energy of the atom in the bulk crystal structure, E_{atom} is the energy of an isolated atom, and N the number of atoms in the bulk structure.

4.2.4 Surface energies

The relaxed bulk structure unit cell was expanded to model the crystal structure. A vacuum distance of 15 Å was introduced in the z-direction to keep the images from interacting. The dimensions were $5.75820 \times 5.75820 \times 31.4553$. The crystal model was optimised with 550 eV cut-off energy and 9x9x1 k-points after convergence. The k-point in the direction of the vacuum was set to 1 to reduce computational demand. As the lattice parameters were optimised in the bulk structure, the lattice parameters were fixed during the rest of the optimisations.

The crystals were cut along the relevant directions [111], [311], [200] and [220] to create different slab models. The surface energies were investigated to examine which surface was the most relevant for studying surface reactions. The surface energy was calculated through the following formula:

$$\gamma = \frac{E_{crystal} - nE_{bulk}}{2A} \quad (45)$$

Where $E_{crystal}$ is the energy of the crystal system, n is the number of atoms in the crystal system, E_{bulk} is the energy of a bulk atom in the bulk system and A the surface area.

4.2.5 Crystal layer convergence and extension

When an adsorbate adsorbs to a surface, it usually interacts only with the topmost layers of the crystal model. To reduce computational cost, the number of flexible layers used in the crystal model cut along the [111] direction was converged in terms of surface energy. The bottom layers were fixed and gradually made flexible from the top to the bottom, and because of the fixed layers the surface energy was calculated as follows[82]:

$$\gamma = \frac{1}{A}(E_{crystal}^{relaxed} - nE_{bulk}) - \frac{1}{2A}(E_{crystal}^{unrelaxed} - nE_{bulk}) \quad (46)$$

where A is the slab surface area, $E_{crystal}^{relaxed}$ is the energy of the relaxed crystal structure, n is the number of Ag atoms in the crystal, $E_{crystal}^{unrelaxed}$ is the energy of the unrelaxed crystal structure obtained from a single point calculation, and E_{bulk} is the energy of the bulk structure.

Six crystal layers were fixed and two were left flexible for further calculations. The model was extended to a volume of 2032 \AA^3 , with dimensions $8.6373 \times 8.6373 \times 31.4553$, in order to eliminate interaction between images of the adsorbate when put on the surface.

4.2.6 Isolated ferrocene

To calculate the adsorption energy, the energy of an isolated FeCp_2 needed to be calculated. The FeCp_2 structure optimised in Gaussian 16 was used as an input structure and put inside a box with 20 \AA vacuum in all directions. The cut-off energy was set to 900 eV and k-points to $1 \times 1 \times 1$ after convergence.

4.2.7 Adsorption system

The ferrocene adsorbate was put on the surface to form adsorption systems. Ferrocene was put on the surface in its vertical and horizontal configurations, and at each of the four adsorption sites of an fcc (111) surface, the on-top, hcp hollow, fcc hollow, and bridge positions. All adsorption systems were optimised with fixed lattice parameters and two flexible layers, using 550 eV and $9 \times 9 \times 1$ k-points. The cutoff of the isolated ferrocene converged slowly, therefore a cutoff of 900 eV was used for the calculation of the adsorbate. However, this cutoff is too large and would require too much computational time to use for calculating the adsorption system. To still obtain accurate energies, a single-point calculation was carried out using 900 eV and $9 \times 9 \times 1$ k-points, with the optimised structures at the 550 eV/ $9 \times 9 \times 1$ level used as input structures.

4.2.8 Adsorption energy

The adsorption energy was calculated as:

$$E_{adsorption} = E_{system} - (E_{adsorbate} + E_{adsorbent}) \quad (47)$$

Where $E_{adsorbate}$ is the energy of the optimised FeCp_2 molecule in a vacuum, $E_{adsorbent}$ the energy of the optimised silver crystal system and E_{system} is the energy of the optimised adsorption system containing the crystal and the adsorbed FeCp_2 .

4.2.9 Density of States & Bader charge analysis

To better understand the adsorption process, the electronic configurations, and charges can be analysed. The electronic density of states was calculated. The Bader charge analysis was performed using the code from the Henkelman group.[74]

4.2.10 Adsorption of fragments

To understand how the molecule can dissociate on the surface, the adsorptions of neutral Fe, Cp, and FeCp fragments were modelled and the adsorption energies were calculated.

The isolated neutral Fe, Cp, and FeCp were modelled and optimised, using 1x1x1 k-points. The cutoff energy of Fe was set to 500 eV and for Cp and FeCp 900 eV, after convergence. The systems possessed magnetisation of 4.0, 1.0, and 3.7, respectively, whereas spin polarisation was considered.

The adsorption of Fe and Cp was investigated for the on-top, hcp, fcc, and bridge positions. The adsorption of FeCp was modelled with the iron facing upwards, and downwards. Only the fcc hollow position was considered for FeCp, as this was the favourable adsorption site of both Cp and Fe, respectively. The cutoff of the isolated Cp and FeCp converged slowly, therefore a single-point calculation with a cutoff of 900 eV was performed for the Cp and FeCp adsorption systems.

4.2.11 Vertical decomposition

To model the dissociation of the vertically adsorbed ferrocene on the surface, the surface was extended to a rectangular surface with an area of 129.2 Å² and optimised using 550 eV and 5x5x1 k-points. The neutral FeCp and Cp fragments were put at different fcc positions on the surface and the structures were optimised at 550 eV and 5x5x1 k-points, following a single-point calculation at 900 eV and 5x5x1 k-points.

4.2.12 Horizontal decomposition

To investigate the possible decomposition from horizontal adsorption, the on-top adsorbed ferrocene was moved closer to the surface in steps of 0.2 Å. The z-coordinate of Fe was fixed, while the x and y coordinates were allowed to relax. The C and H atoms were allowed to relax in all directions. The structures were optimised with 5x5x1 k-points and a cutoff of 550 eV, following a single-point calculation at a cutoff of 900 eV. Magnetisation was assessed for each step except the last.

5 Gas phase chemistry

The relative electronic spin state energies and molecular geometries were examined for FeCp_2 and its FeCp , Fe , and Cp fragments. Taking into account the plasma in the CVD approach[15], I examined neutral and charged ferrocene, up to 2 positive or negative charges, and neutral and charged FeCp , Fe , and Cp fragments, up to 3 positive or negative charges. To better understand the structures, the Fe-C, C-C, and C-H bond lengths were investigated for the lowest-energy spin states. The reactions of ion formation reactions were calculated. To describe anions more accurately, I added diffuse functions to the basis set for C and H atoms in the FeCp_2 , FeCp , and Cp anions. To investigate gas phase thermodynamics, the dissociation reactions of neutral and charged FeCp_2 into neutral and charged FeCp , Fe , and Cp fragments were examined. For reactions where anions were present, diffuse functions were added to all species in the reaction.

5.1 Electronic spin states and molecular structures

5.1.1 Relative electronic spin states

Iron and its complexes can have multiple electronic spin states due to incompletely filled d-orbitals, thus I investigated which state had the lowest energy, with Appendix A, Tables A1 - A4 providing calculated electronic energies for each electronic state and species. The relative electronic spin states are compiled in Appendix A, Table A5. To compare the relative energies, I looked to Swart's[24] investigation of the electronic spin states of metallocenes, at the OPBE/TZP level, which has given reliable results for iron[83]. The relative energies of ferrocene were approximately 0.0 (sing.), 206 kJ/mol (trip.), and 217 kJ/mol (quin.), in agreement with experimental data and the results of Pansini et al.[25] at the OPBE/ADZP level of approximately 0.0 kJ/mol (sing.), 160 kJ/mol (trip.), and 181 kJ/mol (quin.). In contrast, the B3LYP functional used here gives lower values, differing by 120-180 kJ/mol: 0.0 (sing.), 82.7 (trip.), and 76.8 (quin.). Note that B3LYP is previously recognized to favour high spins, due to the inclusion of HF exchange in the functional. [24] The results here significantly favours high spins, compared to the OPBE functional. For cases that require accurate determination of the spin states, a thorough investigation is recommended to ensure an appropriate method. For metallocenes, a starting point would be the OPBE functional. Here, the crucial aspect is to correctly specify the lowest energy state. The singlet was correctly determined as the lowest energy state of ferrocene, consistent with previous results.

5.1.2 FeCp₂

The singlet state of ferrocene, which has zero unpaired electrons, was energetically favourable indicating all electrons occupy the orbitals pairwise. This is consistent with previous results[24, 25, 84]. Swart[24] has suggested that the low spin state of metallocenes increases the covalent bonding properties of the ligand-metal bond, hence favouring the low spin state. Figure 14 shows the optimised geometrical structure of the ferrocene molecule. The singlet state ferrocene's Fe-C, C-C, and C-H bond was 2.070 Å, 1.423 Å, and 1.077 Å, respectively. A compilation of experimental and calculated bond lengths from previous studies is found in Table 2.

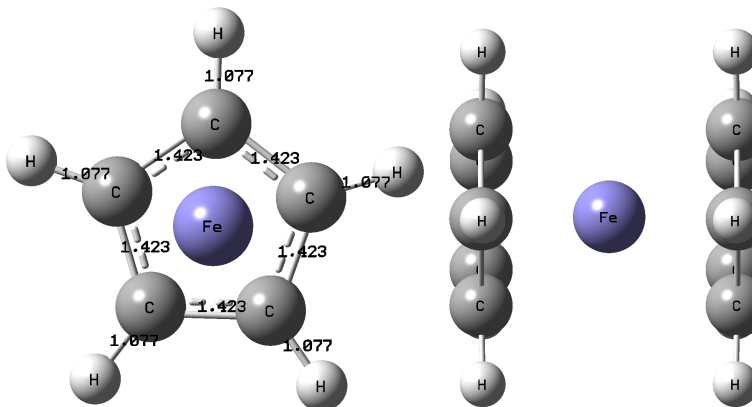


Figure 14: Geometrical structure (top and side view) of ferrocene.

Table 2: Compilation of the Fe-C, C-C, and C-H bond lengths (Å) of ferrocene from this and other experimental and theoretical works.

^a The def2tzvp basis set was used for Fe, and the 6-311G(2df,2pd) basis set was used for C and H.

^b The LanL2DZ basis set was used for Fe and the 6-31G* basis set was used for C and H.

Method	Fe-C	C-C	C-H	Ref.
B3LYP/ (def2tzvp/6-311G(2df,2pd)) ^a	2.070	1.423	1.077	This work
Experimental	2.064 ± 0.003	1.440 ± 0.002	1.104 ± 0.006	[85]
Experimental	2.058 ± 0.005	1.431 ± 0.005	1.122 ± 0.02	[39]
B3LYP/m6-31G(d)	2.065	1.428	1.082	[40]
B3LYP/ (LanL2DZ/(6-31G*)) ^b	2.079-2.080	1.428	-	[84]
B3LYP/ADZP	2.078 Å	1.429	1.091	[25]
OPBE/TZP	2.007	1.431	1.087	[24]

Experimental results found Fe-C, C-C, and C-H bond length in the ranges 2.053-2.067 Å, 1.426-1.442 Å, and 1.098-1.142 Å, respectively.[39, 85]. Compared to experimental results, the calculated Fe-C bond length agrees well while the C-C and C-H bond lengths are underestimated. The Fe-C bond length is slightly longer (0.003-0.017 Å deviation), and the C-H bond length is slightly shorter (0.003-0.019 Å deviation) compared to experimental results, with relative errors of 0.15-0.83% and 0.21-1.32%, respectively. Deviations larger than ± 0.1 Å are common for coordination complexes[59], hence the result of the Fe-C bond length provided here agrees exceptionally well.

In a previous project[26], I investigated the ferrocene bond lengths by using different hybrid functionals with different extents of HF exchange (B3LYP, MO6-2X) and a pure DFT functional (PBE), along with different basis sets. The B3LYP functional gave results in close agreement with experimental results, while the MO6-2X overestimated and PBE underestimated the Fe-C bond length. The B3LYP functional has also previously been stated to give reliable results of the geometry of metallocenes[23].

The Fe-C bond length here lies within the range of what has been found in previous theoretical works (2.007-2.080 Å). The C-C and C-H bond lengths are slightly shorter than what has been found in other works. Compared to the Fe-C bond length of 2.007 Å obtained at the OPBE/TZP level[24], the Fe-C bond length presented here agrees better with the experimental, while the C-C and C-H bond lengths show less agreement with the experiment. The differences are likely due to the different functional and basis sets. Compared to computational results from other works using the same functional as here, B3LYP, the bond lengths agree very well. The C-C and C-H bond lengths calculated here are a bit shorter compared to the other computations (1.428-1.429 Å, and 1.082-1.091 Å)[25, 40, 84]. This is likely an effect of the difference in basis sets. The smaller 6-31G*/LanL2DZ[84] and ADZP[25] basis sets gave longer Fe-C bond lengths than that presented here. Thus, the def2tzvp/6-311G(2dp,3df) basis set gives better predictions on the Fe-C bond length. The m6-31G(d)[40] basis set gave Fe-C bond lengths in very close agreement with experimental data. m6-31G(d) is a modified basis set to better describe first-row transition metals[86], and it can indeed be seen that it performs well, better than the def2tzvp/6-311G(2dp,3df) basis used here. However, the difference is relatively small.

Overall, I consider the mixed basis set def2tzvp/6-311G(2pd,2df) a good choice for appropriately describing the bond lengths in ferrocene, especially the metal-carbon bond length, and possibly other metallocenes.

5.1.3 FeCp₂ ions

Appendix A, Table A6 gives details of the spin state and Fe-C, C-C, and C-H bond lengths for the lowest-energy spin state structures of ferrocene ions and fragments.

FeCp₂⁻ (d⁷), was found to be in a doublet spin state, which is highly reasonable, as an electron is added to a molecule with no unpaired electrons. This electron should reasonably occupy one of the vacant LUMO orbitals. For the FeCp₂²⁻ (d⁸) ion, the energies of the quintet and triplet states differ only by 1 kJ/mol, which is essentially negligible and both should be almost equally accessible. Suggestively, the electrons occupy the LUMO orbitals according to Hund’s rule in the triplet state. In the quintet state, the electrons must have occupied higher-energy orbitals than the first LUMO. The most favorable state for FeCp₂⁺ (d⁵) is the doublet state, indicating the removal of one electron from the HOMO orbital, consistent with experimental findings[23]. The FeCp₂²⁺ ion (d⁴) is in a triplet state, suggesting the removal of another electron from the HOMO orbital.

In terms of bond lengths, the Fe-C bonds are longer in the ions compared to FeCp₂. This is reasonable, as the addition or removal of electrons disrupts the 18-electron rule, leading to fewer accessible electrons for maintaining the aromatic structure of the rings in cations and increased repulsion forces in all ions. Consequently, the bond lengths increase, indicating that the ions may be more prone to dissociation. This is further investigated later, by examining dissociation reactions.

To accurately describe electron behaviour in anions, diffuse functions can be added to the basis set. Diffuse functions were included for the anions, specifically on C and H as the charge is not expected to distribute on Fe due to its low reduction potential. The inclusion of diffuse functions resulted in smaller Fe-C, C-C, and C-H bond lengths in the anions. The optimised geometries of the FeCp₂ ions are visualised in Appendix B, Table B1.

5.1.4 FeCp fragments

The FeCp complex can form when FeCp₂ loses one of its Cp⁻ rings. The optimised geometries of the FeCp fragment and ions are visualised in Appendix B, Table B2. The Fe-C bond lengths were in the range of approximately 2.1-2.5 Å. Most Fe-C bond lengths are longer in the fragments than in ferrocene, indicating a possible decrease in interaction between iron and carbon. The ions have in general high spin states.

FeCp⁻ and FeCp²⁻ were favoured in a quintet and quartet state, respectively, indicating the extra electron in FeCp²⁻ has been added to an unpaired electron. In both complexes, the C-C and C-H bond lengths share equal values, indicating an equal distribution of the electrons between the carbons, suggesting aromatic properties in the ring. FeCp³⁻ had a singlet state.

FeCp is favoured in a sextet state with long Fe-C and shorter C-C and C-H bond lengths, indicating stronger bonding in the ring and weaker Fe-C bonding. It is reasonable that the extra positive charge compared to FeCp⁻ is distributed throughout the carbon rings, leading to a lower electrostatic attraction to the positively charged iron.

The electronic spin states of FeCp⁺, FeCp²⁺ and FeCp³⁺ were all expected, with successively lower spin states: quintet, quartet, and triplet states, respectively, and increasing Fe-C, C-C and C-H bond lengths. The electrons are expected to be removed one by one from the highest-lying orbitals, and the bond lengths are expected to increase due to the repulsion forces. In the structures, the Fe-C, C-C, and C-H bond lengths vary from shorter to longer.

The differences in lengths of the C-C bonds signify that the C-C bonds might start to form double and single bonds, respectively. As a rule of thumb, a C-C single bond is around 1.5 Å, while a double bond is around 1.3 Å. Hence, some of the bonds are closer to a double bond, and some are closer to a single bond, indicating that aromaticity is lost in the ring. This should reasonably lead to destabilization. The Fe-C and C-H bonds depend on the bond length of the adjacent C-C bond.

5.1.5 Cp fragments

The optimised geometries of the Cp fragment and ions are visualised in Appendix B, Table B3. Cp⁻ was calculated to be in a singlet state. Cp⁻ has a practically aromatic structure and is relatively stable. It has three π -bonds, in which it shares 6 electrons. For an aromatic structure, it is expected that the bonding orbitals are filled with paired electrons, leaving the anti-bonding orbitals vacant, in accordance with Hückel’s molecular orbital theory.

The neutral Cp radical had a doublet spin state, which is reasonable. As the Cp⁻ anion has a practically aromatic structure and all-paired electrons, removing one of the electrons would leave one of the orbitals with an unpaired electron. The C-C bond lengths vary, with the shorter and longer bonds having characteristics of double and single bonds, respectively. The C-H bonds vary depending on the C-C bond lengths.

Cp²⁻ and Cp³⁻ were favoured in a doublet and singlet state, so the addition of further electrons to the Cp⁻ anion fills one of the vacant anti-bonding orbitals. Cp⁺, Cp²⁺, and Cp³⁺ were favoured in a triplet, doublet, and singlet state. This means the electrons should be removed from one of the weakly bonding orbitals at a time.

The anions all had equal C-C bond lengths, indicating a resonance structure. The Cp⁻, Cp²⁻, and Cp³⁻ all have C-C bond lengths relatively close to each other (1.410, 1.410, 1.412 Å). However, the C-H bond lengths become larger the higher

the negative charge on the ion (1.085, 1.104, 1.214 Å). The added electrons should be incorporated into the aromatic carbon ring because there it should be easier to distribute the electronic charge. The addition of those electrons could cause repulsive forces toward the electrons in the hydrogen atoms, leading to a longer bond C-H length.

The Cp^+ ion had equal C-C bond lengths, indicating a resonance structure, although the bonds were longer than in Cp^- . The Cp^{2+} had varying C-C and C-H bond lengths. The Cp^{3+} ion had long C-C bond lengths, indicating single bonds. It is very reasonable that the aromatic properties in the ring are lost with the removal of electrons.

5.1.6 Fe fragments

Fe was calculated to be in a quintet state, with electrons distributing according to Hund's rule. The Fe^+ , Fe^{2+} , and Fe^{3+} ion has a sextet, quintet, and sextet state, respectively. The anions Fe^- , Fe^{2-} and Fe^{3-} display a quartet, triplet and doublet state, respectively.

5.2 Electronic energies, enthalpies and Gibbs free energies of ion formation

Reactions of ion formation provide valuable information about energy requirements for electron addition and removal. Comparing calculated energies of the removal and addition of electrons to ferrocene with experimental results of the plasma electron energy might indicate whether the reaction would occur. This aids to determine the fragments present in the chamber and the growth-contributing chemical species. Table 3 lists calculated $\Delta_r E$, $\Delta_r H$, and $\Delta_r G$ values for each ion with the electron treated as a reactant or product.

Accurately describing ionisation processes is generally a bit more complex than describing the ground state, since it often involves the occupation of excited states. A deviation of around 0.2 eV (≈ 19 kJ/mol) is common for ionisation energies and electron affinities. B3LYP has been recognised to give relatively accurate ionisation energies.[59]

The energies, enthalpies, and Gibbs free energies of the ion formations increases with increasing positive or negative charge. This means it is increasingly more difficult to remove or add electrons to an ion of higher charge. This is expected, due to the increasing repulsion forces.

Few experimental data on ionisation are available for comparison of ferrocene and its fragments. The first ionisation enthalpy of ferrocene is calculated to be 679 kJ/mol. Compared to the experimental ionisation enthalpy of approximately 667 kJ/mol[87], this value compares well. The deviation is approximately 12 kJ/mol. The first ionisation enthalpy of Cp is calculated to 793 kJ/mol, which compares relatively well to experimental value of 811[88], with a deviation of 18 kJ/mol. The ionisation enthalpies of iron are here calculated to be 722, 1596, and 3051 kJ/mol. The corresponding experimental values are 762[89]-766[90], 1567[90], and 2964[90] kJ/mol. These differ by approximately 40-44, 29, and 87 kJ/mol. As these values are quite large, the deviation is acceptable. The enthalpies of the anions are -74, 767, and 1419 kJ/mol. Compared to the experimental electron affinity of 21 kJ/mol, the corresponding value of 74 here deviates by 53 kJ/mol. To yield more accurate results, diffuse functions could be included. However, as Fe here has a +II positive oxidation state in ferrocene and ideally is reduced to Fe^0 in the CVD process, as well as iron's low reduction potential, the accurate description of Fe anions is not investigated further here.

Table 3: Electronic energies $\Delta_r E$, enthalpies $\Delta_r H$, and Gibbs free energies $\Delta_r G$ of ion formation, and experimental enthalpies of ion formation ($\Delta_r H$). The calculations were performed at the def2tzvp/6-311G(2df,2pd) level including Grimmes D3 dispersion correction. Obtained bond lengths after inclusion of diffuse functions are included in the parentheses, calculated at the def2tzvp/6-311++G(2df,2pd) level including Grimmes D3 dispersion correction. The thermochemistry is calculated at standard temperature and pressure, $T = 298.15$ K, $p = 1$ atm. All values are in kJ/mol.

Product	$\Delta_r E$	$\Delta_r H$	$\Delta_r G$	Exp. $\Delta_r H$
FeCp_2^-	67 (45)	48 (27)	36 (15)	667[91]
FeCp_2^{2-}	550 (258)	537 (253)	538 (252)	
FeCp_2^+	680	679	681	
FeCp_2^{2+}	1127	1117	1120	
Fe^-	-71	-74	-67	-21[90]
Fe^{2-}	773	767	781	762 [89] 766 [90] 1567 [90] 2964 [90]
Fe^{3-}	1429	1419	1440	
Fe^+	719	722	715	
Fe^{2+}	1590	1596	1583	
Fe^{3+}	3042	3051	3030	
FeCp^-	17 (-1)	9 (-7)	23 (-3)	
FeCp^{2-}	461 (253)	408 (-247)	417 (253)	
FeCp^{3-}	1151 (803)	1169 (804)	1189 (818)	
FeCp^+	623	627	620	
FeCp^{2+}	1303	1304	1291	
FeCp^{3+}	1913	1918	1899	
Cp^-	-140 (-172)	-144 (-176)	-131 (-157)	-173 \pm 4.5[92]
Cp^{2-}	710 (368)	692 (362)	705 (364)	811[88]
Cp^{3-}	1092 (598)	1073 (598)	1095 (607)	
Cp^+	784	793	792	
Cp^{2+}	1503	1502	1482	
Cp^{3+}	2141	2168	2159	

Electron affinity is defined as the release of enthalpy when an anion is formed, thus the release of energy is positive, as opposed to thermodynamic convention. This is an effect of the fact that a free electron is highly unfavourable and generally considered to have zero energy at 0 K. In the cases where negative electron affinities occur, such as for some noble gases, the value is only very slightly positive. The anions FeCp_2^- and FeCp^- have a positive value of the enthalpy of ionisation, which means the electron affinity is negative. This is not reasonable, according to the

previous reasoning. This means there are errors in the calculations. This is not uncommon, especially for negative molecules where the electron cloud is expected to be diffuse. However, it gives an indication that the anion formation is not that favourable and the electron affinities for these ions are most probably small. This would be reasonable, as ferrocene is an 18-electron system. An 18-electron system is generally considered a very stable configuration, and the addition of another electron would impair this configuration and thus is expected to destabilise the complex.

To see if the problem of positive electron affinities could be addressed, diffuse functions were included on the C and H atoms in ferrocene and the anions. The reaction electronic energies, enthalpies, and Gibbs free energies of the first and second anion formation decreased significantly, as expected. However, the enthalpy of the first anion formation is still positive, 27 kJ/mol. This means that the diffuse functions used here could not accurately describe the behaviour of the ions and that the electron cloud is probably very big. Another computational study[93] at the 6-311+G(2d,p) level arrived at an enthalpy change of anion formation of approximately 41, thus this seems like a consistent problem. To solve it, one could try adding even larger diffuse functions to the basis set. However, this has not been done here and is left as a future outlook to reach higher accuracy of the calculations.

As the addition of diffuse functions to the basis set gives more reasonable energies, enthalpies, and Gibbs free energies of the anion formations, diffuse functions on C and H were added also to the FeCp and Cp anions. Similar results are seen for the formation of these ions, where the inclusion of diffuse functions lead to lower energies, enthalpies, and Gibbs free energies, and an increasing difference with increasing negative charge. This is as anticipated, as the electron clouds are expected to increase with increasing charge.

5.3 Ferrocene dissociation

Examining bond lengths reveal chemical interactions. To gain deeper insights, I analysed the thermodynamics of dissociation reactions in the gas phase. This reveals the thermodynamically favourable reactions and whether the molecules and ions are stable or reactive in the gas phase. I investigated the dissociation of FeCp_2 and its ions, including up to two positive and negative charges. The considered fragments were FeCp , Fe , and Cp and respective ions up to three positive and negative charges. Appendix C, Table C1 lists all investigated reactions, energies, enthalpies, and Gibbs free energies, calculated without diffuse functions. Table 4 shows the lowest-energy reactions, energies, enthalpies, and Gibbs free energies from the asymmetric and symmetric dissociation of respective ferrocene species. Two symmetric dissociation reactions for FeCp_2^{2-} are shown as both are spontaneous.

Table 4: The investigated dissociation reactions of FeCp_2 and ions into FeCp , Cp , and Fe fragments. The calculations were performed at the def2tzvp/6-311G(2df,2pd) level including Grimmes D3 dispersion correction. Obtained bond lengths after inclusion of diffuse functions are included in the parentheses, calculated at the def2tzvp/6-311++G(2df,2pd) level including Grimmes D3 dispersion correction. The thermochemistry was calculated at standard temperature and pressure, $T = 298.15$ K, and $p = 1$ atm.

Reactant	Products	$\Delta_r E$	$\Delta_r H$	$\Delta_r G$
FeCp_2	$\text{FeCp} + \text{Cp}$	397	380	305
	$\text{Fe} + 2 \text{ Cp}$	673	647	532
FeCp_2^-	$\text{FeCp} + \text{Cp}^-$	191 (174)	188 (168)	138 (125)
	$\text{Fe} + \text{Cp}^- + \text{Cp}$	466 (449)	455 (437)	365 (349)
FeCp_2^{2-}	$\text{FeCp}^- + \text{Cp}^-$	-342 (-85)	-343 (-92)	-374 (-129)
	$\text{Fe} + 2 \text{ Cp}^-$	-224 (19)	-229 (8)	-300 (-61)
	$\text{Fe}^- + \text{Cp} + \text{Cp}^-$	-155 (120)	-159 (110)	-236 (30)
FeCp_2^+	$\text{FeCp}^+ + \text{Cp}$	341	322	251
	$\text{Fe}^+ + 2 \text{ Cp}$	712	684	573
FeCp_2^{2+}	$\text{FeCp}^+ + \text{Cp}^+$	-2	-12	-66
	$\text{Fe}^+ + \text{Cp} + \text{Cp}^+$	369	351	256

Two reactions are shown to be energetically favourable, the dissociation of the bivalent positive and negative ions. This is probably due to the high repulsion forces within these ions. The other reactions are calculated to energetically unfavourable, which is reasonable as ferrocene is generally considered to be very stable.

The enthalpy of dissociation of the removal of one and two neutral rings $\text{FeCp}_2 \longrightarrow \text{FeCp}^0 + \text{Cp}^0$, and $\text{FeCp}_2 \longrightarrow \text{Fe}^0 + 2\text{Cp}^0$ were calculated to be 380 and 647 kJ/mol, agreeing exceptionally well with experimental results of approximately 382 kJ/mol[94] and 663 kJ/mol[94]. The deviation is 2 and 16 kJ/mol, respectively. Asymmetric dissociation is more energetically favourable than symmetric dissociation.

The most favourable dissociation reaction of FeCp_2^+ was $\text{FeCp}_2^+ \longrightarrow \text{FeCp}^+ + \text{Cp}$, and the energy of dissociation decreases compared to ferrocene; from 397 kJ/mol in FeCp_2 to 341 kJ/mol in FeCp_2^+ . The most favourable symmetric dissociation of FeCp_2^+ was to form Fe^+ and two Cp, with $\Delta E = 712$ kJ/mol. The dissociation energy is higher compared to the ferrocene molecule, even though the Fe-C bond lengths are longer in the FeCp_2^+ complex. A possible explanation is that the positive charge is easier to distribute throughout the FeCp_2 complex than it is putting the positive charge on one of the separate fragments. The positive charge in FeCp_2 does however seem to increase the electrostatic repulsion between the Fe and ligands, leading to an increase in the bond lengths. The dissociation of FeCp_2^{2+} into FeCp^+ and Cp^+ was calculated as slightly exothermic and spontaneous, probably due to repulsion forces between two positive charges. The bond lengths are longer than in FeCp_2 and FeCp_2^+ , also indicating the bonding could indeed be weaker in this ion.

As the addition of diffuse functions is important in the description of anions, the reactions for which anions are present as reactants or products are calculated with diffuse functions on C and H for all species in the reaction.

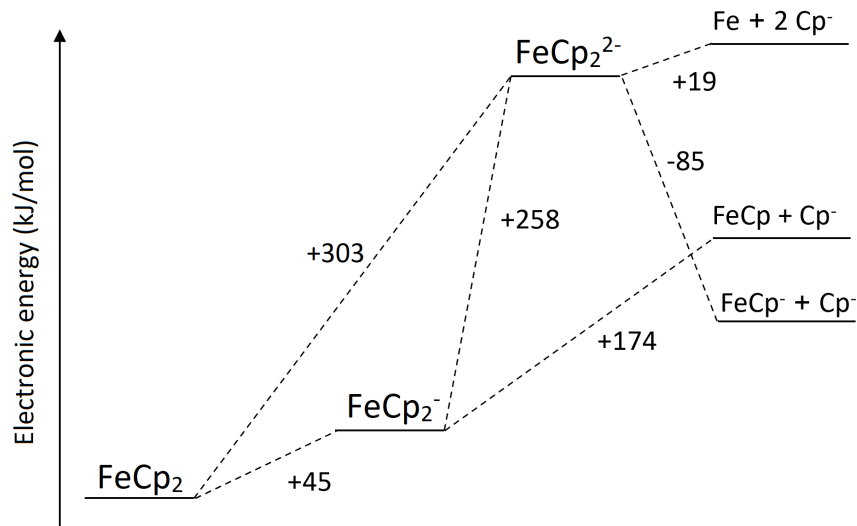
The dissociation energy, enthalpy, and Gibbs free energy of the ferrocene anions FeCp_2^- and FeCp_2^{2-} decreases with increasing negative charge. This is reasonable, due to the increase in repulsion forces between like charges. The addition of diffuse functions to the anions made a large difference in the energies, enthalpies, and Gibbs free energies. The dissociation energy of $\text{FeCp}_2^- \longrightarrow \text{FeCp}^0 + \text{Cp}^-$ and $\text{FeCp}_2^{2-} \longrightarrow \text{FeCp}^- + \text{Cp}^-$ is 223 and 482 kJ/mol more favourable than the dissociation energy of the neutral ferrocene, respectively. This indicates that the rings are easier to dissociate when the complex has earned negative charges. This is reasonable, both because of repulsion, but also because anti-bonding orbitals are occupied in the anions. The results shows that the asymmetric dissociation of FeCp_2^{2-} to form $\text{FeCp}^- + \text{Cp}^-$ is spontaneous and energetically favourable.

If the complex obtains two negative charges in the gas phase, it could decompose and form FeCp^- and Cp^- fragments in the asymmetric dissociation, or undergo symmetric dissociation to form pure Fe^0 and two negatively charged Cp^- rings. The decomposition to form FeCp^- and Cp^- is more thermodynamically favourable, which makes this reaction more likely to occur. The formation of Fe^0 and two negatively charged Cp^- rings is less favourable but would still be possible

if provided energy by the plasma electrons. Even if Fe^0 and two negatively charged Cp^- rings were to be formed, Fe^0 is likely not the species contributing the most to growth, as it is neutral and hence would not be attracted to the positive substrate bias due to a low reduction potential.

The reaction energy of the first ionisation was 45 kJ/mol and the second was 253 kJ/mol. The likelihood of these reactions occurring depends on the energy of the electrons in the plasma. As the electrons in a plasma generally are high, it is reasonable that FeCp_2^{2-} could form in the gas phase. However, this needs to be confirmed by investigating the actual energy of the electrons in the plasma. So long, experiments point to the electrons having an energy of 100-600 kJ/mol at different plasma powers and substrate biases, where the electrons seem to have a large distribution of different energies. Under usual deposition parameters of 60-80 V substrate bias and a plasma power of 100-125 W, the electron energies are distributed around 100-250 kJ/mol. This suggests that the formation of anions could be possible. If the electrons carry high energies, above that of the second ion formation, the likelihood of formation would be higher, and from there the dissociation of the molecule would happen spontaneously. The overall most energetically favourable reaction pathway would be to ionise the ferrocene molecule to the bivalent anion (+303 kJ/mol), following dissociation to form FeCp^- and Cp^- (-85 kJ/mol). If the electrons do not carry high energy, the formation of FeCp_2^- would be more likely as it requires less energy (45 kJ/mol). Then, it could either decompose to form FeCp and Cp^- , requiring 174 kJ/mol, or approach the surface as it is. The most likely species contributing to growth at high, intermediate and low electron energies would be FeCp^- and Cp^- , FeCp and Cp^- , and FeCp_2^- , respectively. If very low electron energies, it could be possible that no gas phase dissociation occurs at all. Under normal deposition parameters, FeCp_2^- , FeCp , and Cp^- are considered the most likely growth species. Figure 15 shows a schematic representation of the ion formation and dissociation reactions of the most likely gas phase reactions from the FeCp_2^- and FeCp_2^{2-} anions.

Figure 15: Schematic representation of the ion formation and dissociation reactions of the most likely gas phase reactions from FeCp_2 to the FeCp_2^- and FeCp_2^{2-} anions, and their fragments.



Whereas thermodynamics gives valuable information about which reactions might occur, reactions are also driven by kinetic factors. As ferrocene is a large molecule, and the CVD method involves plasma reactions, it is highly probable that the reactions are affected by kinetic and dynamic effects. Therefore, kinetic and dynamic considerations would also be of interest. This has not been investigated in this study but is left as a possible future outlook for further investigation.

Challenges are posed since plasma is present during the CVD method. This means that different chemical pathways can open and that the process is highly dynamic since it involves the collision of chemical species and plasma electrons. This makes it difficult to model since so many parameters are involved. To further investigate the gas phase chemistry, kinetic and dynamic considerations would definitely be of interest. This could tell valuable information about the time scale of the reactions and movement of species. If a reaction would happen too slowly, the species formed from that reaction would ultimately lead to no growth.

6 Surface Chemistry

When investigating the surface chemistry of thin film deposition, the first step is to observe the precursor adsorption on the surface. The adsorption energy tells information about if and how the molecule sticks to the surface and how thermodynamically favourable the adsorption process is. Surface chemistry modelling requires both modelling of the adsorbent and the adsorbate. The adsorbate unit cell was initially represented using a bulk structure and subsequently expanded to generate the crystal structure. The slab surface was created by cutting the crystal along the (111) direction. To eliminate image interactions the isolated adsorbate was enclosed in a box of vacuum in all directions. After optimisation, the adsorbate was placed on the surface adsorption sites and the structure was relaxed.

6.1 Bulk and crystal characterisation

The Ag fcc bulk structure, which belongs to the Fm-3m space group, was modelled as shown in Figure 16. Upon convergence, the k-points and cutoff energy were set to 7x7x7 and 450 eV, as illustrated in Figure 17. The bulk structure was optimised with and without D3-Grimme dispersion correction. The respective lattice constants were 4.072 and 4.146 Å, cell volumes 67.501 and 71.247 Å³, and the Ag-Ag nearest neighbor distances 2.879 and 2.931 Å. In both structures, the cell angles were 90°.

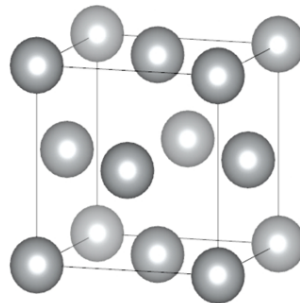


Figure 16: The optimised Ag bulk structure, with dispersion correction (gd3).

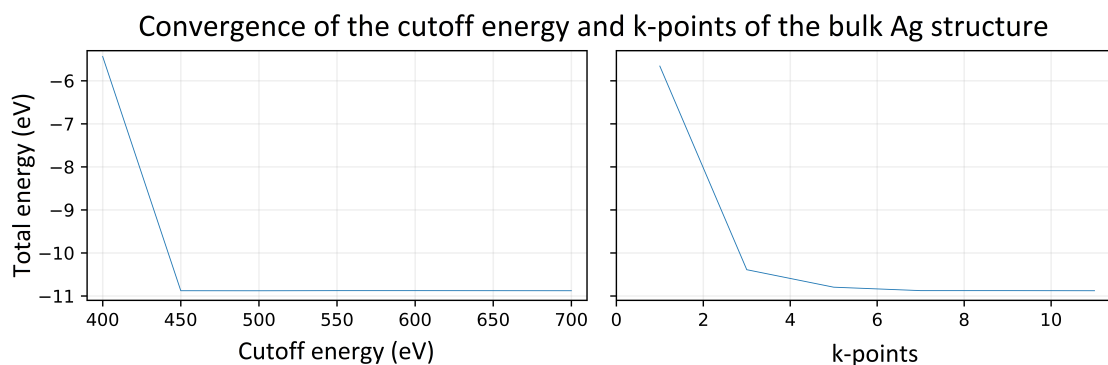


Figure 17: Convergence test of the Ag bulk system, showing the cutoff energy (left) and the k-points (right), with x being the k-points used in all directions (x×x×x).

6.1.1 Isolated Silver atom and Cohesive energy

Modelling of the bulk and an isolated silver atom in the gas phase is required to calculate the cohesive energy. With the inclusion of dispersion correction, the resulting cohesive energy was $E_{cohesive} = 3.009$, whereas without dispersion correction, 2.519. Table 5 summarises cohesive energy, cell volume, Ag-Ag bond length, and lattice constant of the bulk crystal structure, alongside corresponding values from various experimental and theoretical studies.

Table 5: Properties of the Ag bulk structure in terms of total energy, cohesive energy, cell volume, Ag-Ag bond length, and lattice constant a of the cubic structure, with and without Grimmes D3 dispersion correction (D).

^a Dispersion corrected PBE[95].

	$E_{cohesive}$ (eV)	Volume (\AA^3)	Ag-Ag (\AA)	a (\AA)	Ref.
PBE (D)	3.009	67.50	2.88	4.072	This work
PBE	2.519	71.25	2.93	4.146	This work
Exp.	2.95	-	-	-	[96]
Exp.	-	67.32	-	4.068	[97]
Exp.	2.972	-	-	-	[98]
PBE	2.513	-	-	4.163	[98]
PBE-D ^a	3.078	-	-	4.155	[98]
PBE(D)	-	-	-	4.156	[99]

Compared to the experimental cell volume of 67.32 \AA^3 [97] lattice constant of 4.068[97] \AA , and the cohesive energy 2.95-2.97[96, 98], the calculation with the dispersion correction shows better agreement. The cell volume differs from the experiment by 0.181 \AA^3 , the lattice constant by 0.004 \AA , the Ag-Ag bond length by 0.011 \AA , and the cohesive energy by 0.039-0.059 \AA . The deviations are 2.7%, 0.1-0.5%, 0.38%, and 1.3-2.0 %, respectively. The calculated results show excellent agreement with the experiment and reproduction of results from other computational studies[98], indicating method reliability.

6.1.2 Slab models and surface energies

X-ray Diffraction (XRD) is a technique to characterise the crystalline phases of a crystal by irradiating the crystal with incident X-rays and measuring the angle of the diffracted X-rays. XRD data of a silver thin film grown on a Si substrate was obtained through collaboration with experimentalists at Linköping University and showed the relevant growth directions of the polycrystalline silver substrate, shown in Figure 18. The preferred growth direction could be determined [111] by examining peak positions and relative intensities and comparing them to a reference from the Joint Committee on Powder Diffraction Data (JCPDD)[97].

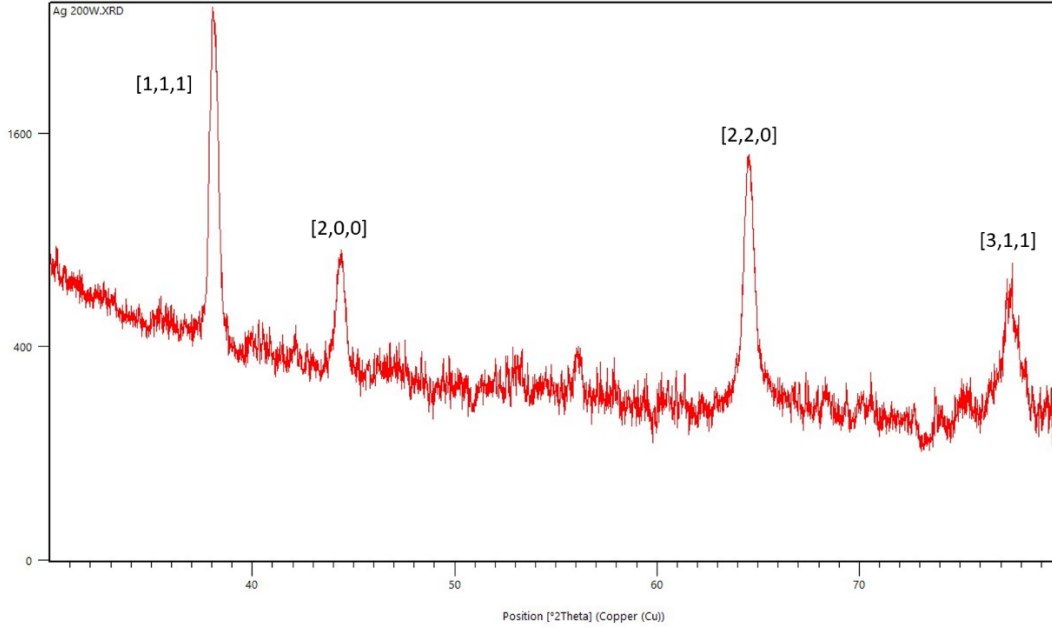


Figure 18: X-ray Diffraction (XRD) measurement of a polycrystalline silver substrate.

The energies of the surfaces from the XRD measurement were investigated by cutting the crystal along different directions [111], [311], [200], and [220] to form (111), (311), (200), and (220) slab models of the surfaces. The thickness of the crystal models were 16.455, 7.366, 8.6137, and 8.143 Å, and contained 32, 10, 14, and 28 atoms, respectively. The surface areas were 28.715 Å², 16.578 Å², 23.445 Å², and 57.429 Å², respectively.

The total energy, surface area, total number of atoms in the model, and the surface energy γ for the different surfaces are compiled in Table 6. The surface energies for the (111), (200), (220), and (311) were calculated to be 1.328, 1.409, 1.480, and 1.411 J/m², with the smaller the surface energy, the more stable the surface. The calculations showed the (111) surface has the lowest energy, which means it is the preferred growth direction, in agreement with the experimental XRD data and previous theoretical findings[99]. The calculated surface energy of Ag(111) of 1.328 J/m² also agreed relatively well with experimental data 1.246-1.250 J/m²[100, 101], with a deviation of $\approx 6\%$, which indicates the reliability of the method. Therefore, the crystal cut along the [111] direction was used for further calculations.

Table 6: Total energy, area, number of atoms, calculated surface energies of the surfaces, and experimental surface energy of Ag(111).

Surface	Total E (eV)	Area (\AA^2)	Thickness (\AA)	Atoms	γ (J/m ²)
Ag(111)	-97.891	28.715	16.455	32	1.328
Ag(200)	-40.578	16.578	7.366	10	1.409
Ag(220)	-29.162	23.445	8.6137	14	1.480
Ag(311)	-79.704	57.429	8.143	28	1.411
Exp. Ag(111)	-	-	-	-	1.246[100] 1.250[101]

6.1.3 Convergence of the crystal layers and extension of the crystal structure

When an adsorbate adsorbs to a surface, it usually interacts only with the topmost layers of the crystal. To reduce computational effort all layers are initially frozen and layer-wise made flexible from the bottom up to allow the surface energy to converge, see Figure 19. This indicates that the adsorbate would merely interact with the top surface layer. However, to ensure reliable results, a model with two flexible layers was used for further calculations. However, to ensure reliable results, a model with two flexible layers was used for further calculations.

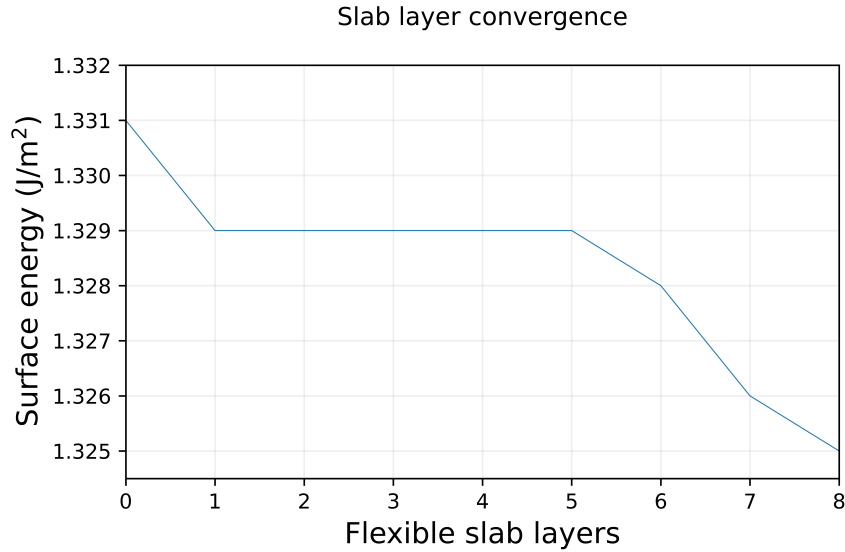


Figure 19: Convergence of the surface energy of the slabs with different numbers of flexible layers in the crystal.

Diligence towards image interaction is essential when adding an adsorbate to the slab, as an inadequate surface area would induce interactions between the adsorbate and its images in nearby cells. Figure 20 visualises the expanded crystal structure. The k-points and cutoff energy were set to 5x5x1 and 550 eV after convergence. The extended surface area was 74.603 Å², the model contained 72 Ag atoms and eight layers of which two were flexible.

6.2 Isolated ferrocene

To calculate the adsorption energy, the energy of the gas-phase ferrocene needed to be obtained. The ferrocene geometry optimised in Gaussian 16 was used as input structure and was enclosed in 20 Å vacuum in all directions, as seen in Figure 21. The k-points were set to 1x1x1 and the cutoff energy to 900 eV after convergence.

The gas phase ferrocene Fe-C, C-C, and C-H bond lengths were 2.040, 1.434, and 1.086 Å, respectively. These values differ from those obtained from the earlier gas phase calculations in Gaussian 16, using B3LYP and the mixed basis set def2tzvp/6-311G(2pd,2df), which is expected as a result of the different functionals and basis sets. Compared to bond lengths obtained at the PBE/def2tzvp level calculated in Gaussian[26], corresponding bond lengths of 2.043, 1.434, and 1.087 Å, agree well with the values presented here. This indicates that the differences occur mainly due to the used functional. The B3LYP functional is a DFT/HF hybrid functional, and PBE is a pure DFT functional. It has previously been shown that the ferrocene bond lengths are overestimated by DFT functionals and underestimated by HF functionals and that the B3LYP functional gives results in close agreement with experiments[26, 37].

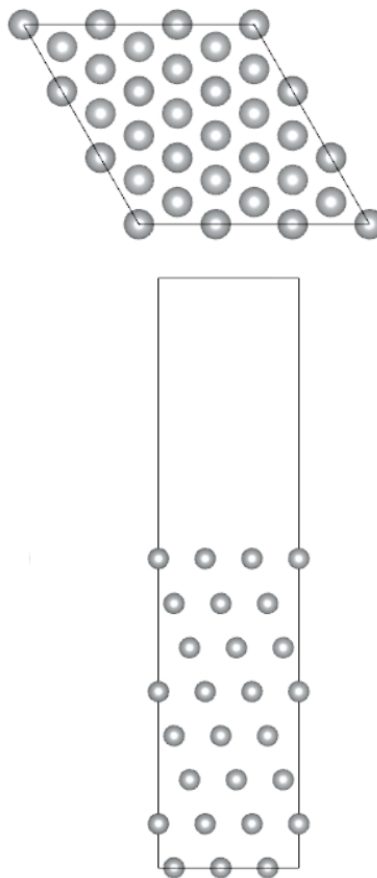


Figure 20: Side and top view of the Ag crystal model, containing 72 Ag atoms.

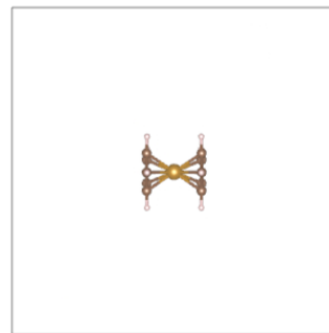


Figure 21: The gas-phase ferrocene molecule in a box with 20 Å vacuum in all directions.

6.3 Ferrocene adsorption

The horizontal and vertical adsorption of ferrocene on the Ag(111) surface was investigated. The adsorption energies were calculated, and are compiled in Table 7 together with the Ag-Fe, Ag-C, and Ag-H adsorption distances.

Table 7: Adsorption energy (E_{ads}) in kJ/mol, Fe-C, C-C, and C-H bond lengths, and Fe-Ag, C-Ag, and C-H distance to the surface of the adsorption of ferrocene to different adsorption sites on the Ag(111) surface. For calculation of the adsorption distances of the vertical adsorption, the average bond lengths of the C and H species in the rings and the average of all the Ag atoms on the first surface layer were used. For the horizontal adsorption, the distances are specified by the C and H closest to the surface, and the average of the Ag atoms on the first surface layer. The adsorption energies are given for the optimised structure at 550 eV cutoff (opt) and the single point calculation at 900 eV cutoff (sp). The bond distances are from the single-point calculation. All bond distances are in Å.

Vertical ferrocene adsorption								
Site	$E_{ads}(\text{opt})$	$E_{ads}(\text{sp})$	Ag-Fe	Ag-C	Ag-H	Fe-C	C-C	C-H
On-top	-68.9	-67.8	4.75	3.12	3.13	2.03-2.04	1.44	1.09
hollow _{hcp}	-73.2	-72.1	4.65	3.02	3.04	2.03-2.04	1.44	1.09
hollow _{fcc}	-73.1	-72.0	4.66	3.03	3.05	2.03-2.04	1.44	1.09
bridge	-72.5	-71.5	4.66	3.03	3.05	2.03-2.04	1.44	1.09
Horizontal ferrocene adsorption								
Site	$E_{ads}(\text{opt})$	$E_{ads}(\text{sp})$	Ag-Fe	Ag-C	Ag-H	Fe-C	C-C	C-H
On-top	-71.3	-72.1	4.40	3.42	2.54	2.03-2.05	1.44	1.09
hollow _{hcp}	-70.5	-72.3	4.46	3.47	2.58	2.03-2.05	1.44	1.09
hollow _{fcc}	-70.7	-71.9	4.45	3.46	2.56	2.04-2.05	1.43-1.44	1.09
bridge	-69.9	-71.1	4.46	3.47	2.58	2.04-2.05	1.44	1.09

Based on Table 7, all the adsorption energies exhibit similar values, indicating an almost equal likelihood for all adsorptions. This suggests there would be a mix of different adsorption configurations and adsorption sites. For the vertical adsorption, the hcp position was found most favourable, with an energy of -72.1 kJ/mol (sp). For the horizontal adsorption, both the hcp and on-top position exhibited similar energies. And the on-top position was slightly more energetically favourable at the optimisation level, while the hcp position was slightly more favourable at the single-point calculation level. These positions could therefore be seen as equally accessible. The adsorption energy of the horizontal on-top adsorption was determined -72.3 kJ/mol (sp). The difference between the vertical

and horizontal adsorption at the most favourable sites is negligible and both adsorptions are considered equally probable. The negative values of the adsorption energies indicate that energy is released during adsorption and that the processes are energetically favorable. It is also seen that the Fe-C, C-C, and C-H bond lengths in the adsorbed ferrocene molecule do not change much compared to the bonds in the gas-phase ferrocene.

6.3.1 Vertical adsorption

The vertical adsorption ranged between $-(61.1-72.1)$ kJ/mol. The Ag-Fe, Ag-C, and Ag-H distances are in the ranges of 4.40-4.46, 3.42-3.47, and 2.54-2.58 Å, respectively. The ferrocene Fe-C, C-C, and C-H bond lengths do not change much depending on the adsorption site and are 2.03-2.04, 1.44, and 1.09 Å, respectively. The modelled vertical adsorption can be seen in Figure 22. It flatly adsorbs on the surface, similar to what has been found previously for benzene[55, 56] and the cyclopentadienyl anion[56] on surfaces.

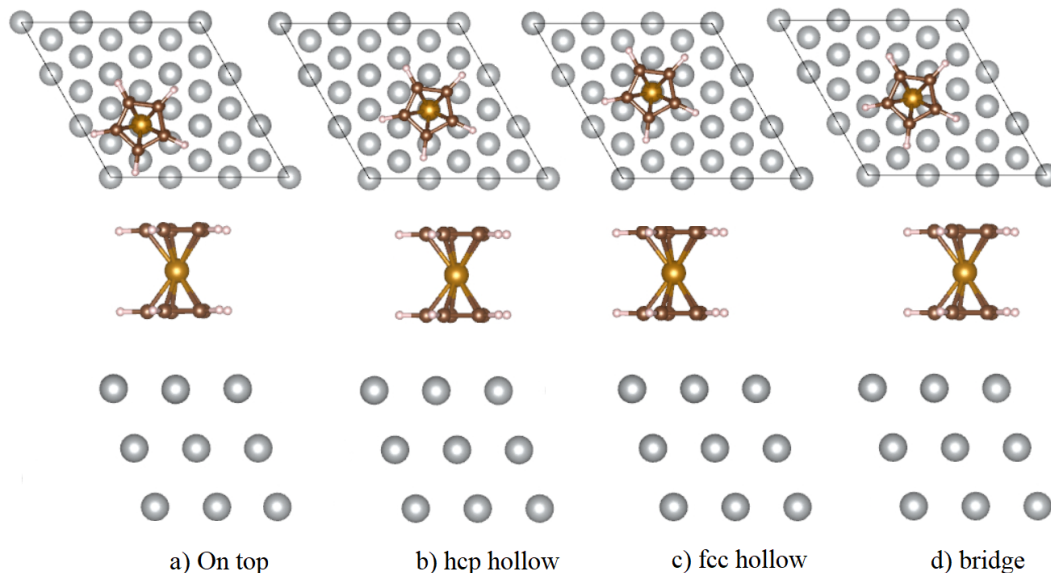


Figure 22: Side and top view of the vertical on-top, hcp hollow, fcc hollow, and bridging adsorption positions of ferrocene.

The vertical hollow_{hcp} position, with the closest proximity to the surface, exhibits the lowest adsorption energy, while the on-top adsorption site that is furthest away from the surface is the least preferred. The favourable adsorption site of a cyclopentadienyl anion on a Ni(111) surface has also been found to be the hcp position[56].

The lower adsorption energy of the hcp position could stem from giving the strongest carbon-silver interaction. The hcp and fcc positions have very close energies and adsorb almost as far from the surface. Figure 22 illustrates that the hcp and fcc hollow sites both provide two carbon atoms close to different top-layer surface silver atoms and a third carbon atom near a third top-layer surface silver atom, maximising C interaction with the top-layer surface silver atoms. This would also explain why the on-top position would be the lowest in energy, as the iron atom is directly placed above a first-layer silver atom. Hence, the carbon atoms do not have any silver atoms nearby. This suggests that it is the carbon-silver interaction that is the most important for vertical adsorption and provides an explanation for the pattern of the adsorption energies. It also indicates that the iron-silver interaction is not as important during vertical adsorption, which is highly reasonable due to the steric hindrance of the ring.

6.3.2 Horizontal adsorption

The horizontal adsorption energies were in the range of $-(71.1 - 72.1)$ kJ/mol. It rendered Ag-Fe, Ag-H, and Ag-C distances in the range of 4.40-4.46, 3.42-3.47, and 2.54-2.58 Å. The horizontal adsorption had shorter Ag-Fe and Ag-H distances, but longer Ag-C distances than the vertical adsorption. The modelled horizontal adsorption can be seen in Figure 23.

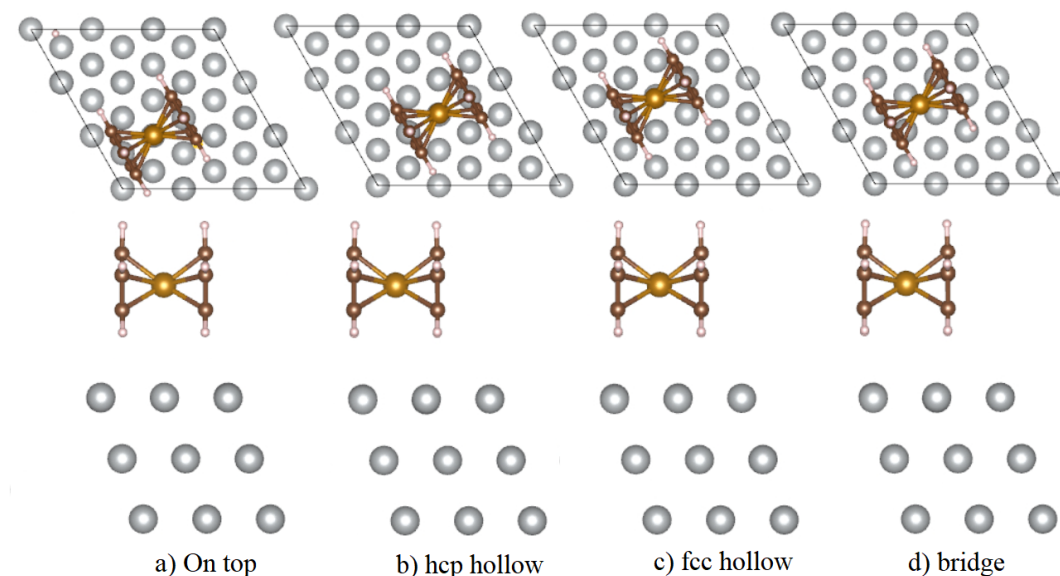


Figure 23: Side and top view of the horizontal on-top, hcp hollow, fcc hollow, and bridging adsorption positions of ferrocene.

The on-top and hcp hollow adsorption sites were the preferred horizontal ad-

sorption sites. The on-top position had the shortest Fe-Ag, C-Ag, and H-Ag distances, of 4.40, 3.42 Å, and 2.54 Å, respectively. In the on-top position, iron is positioned directly above a top-layer Ag atom. This suggests that the Fe-Ag interaction could be important in horizontal adsorption.

6.4 Electronic structure analysis

6.4.1 Density of states

The electronic DOS tells information about the orbital occupation and energies. It gives information about the hybridisation of the orbitals and thus gives indications of chemical interactions and their character.

Figure 24 show the electronic DOS and orbital character of the isolated Ag atom. The HOMO-LUMO gap is approximately 2.6 eV. The p and d-orbitals are respectively degenerate, demonstrating the orbitals are occupied according to Hund's rule. As expected in silver, the $3d$ orbitals lie lower in energy than the $4s$.

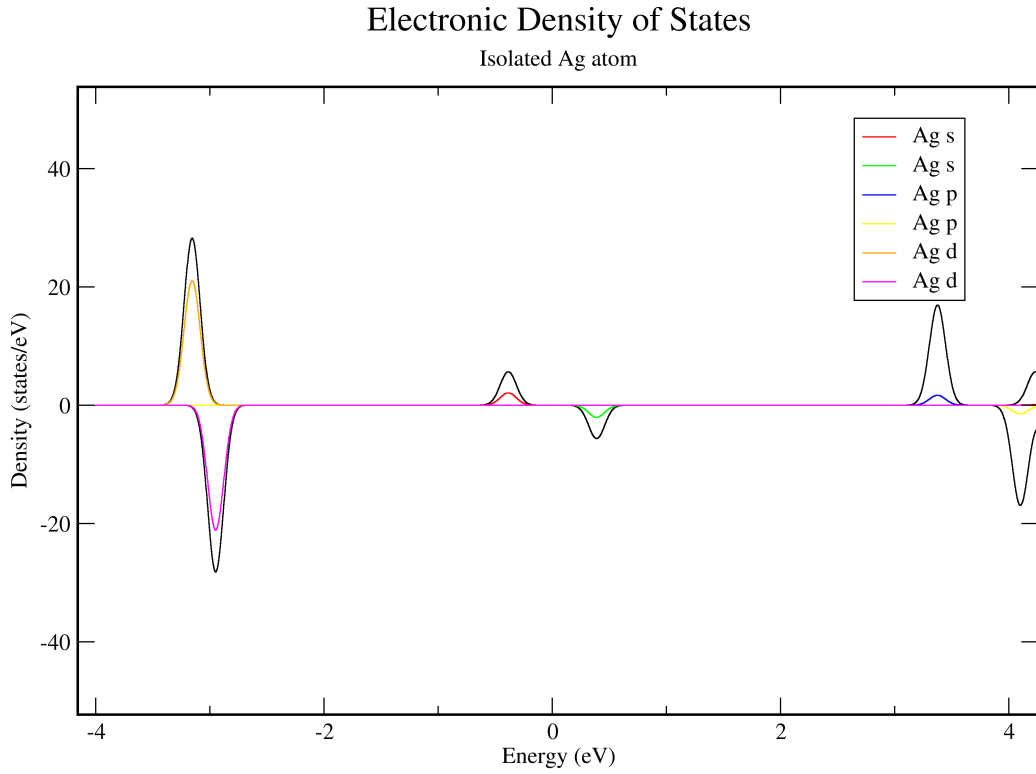


Figure 24: Electronic density of states of the isolated Ag atom.

Figure 25 display the DOS of the bulk silver structure. The bulk exhibits the expected metallic behavior with no band gap. Hybridization between the s, p, and

d orbitals is seen, with d-orbital character predominating in the -6.7 to -2.4 eV range.

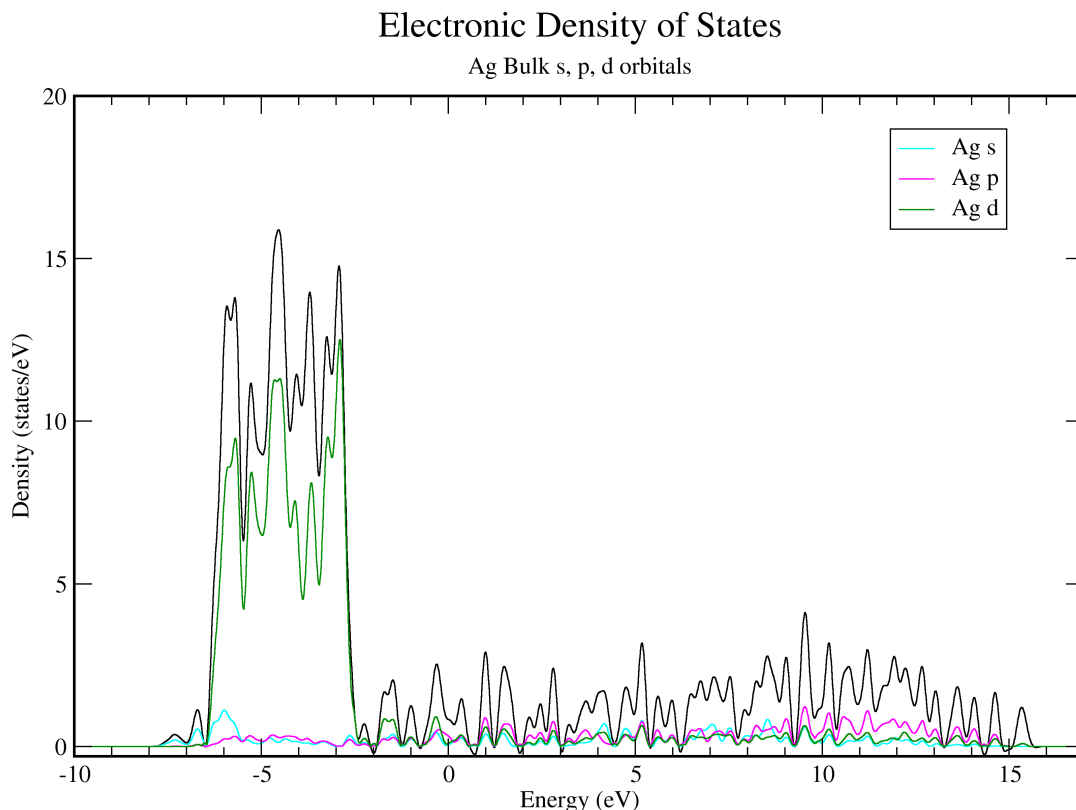


Figure 25: Electronic density of states showing the Ag s,p, and d orbital contributions in the silver bulk structure.

Figure 26 displays the DOS of the gas phase ferrocene. The HOMO-LUMO gap is approximately 2.9 eV. Hybridisation is seen between the C, H, and Fe. The lower-lying orbitals have mainly s(C) character, from the C-C and C-H single bonds. Around (-10)-(-5) eV, the orbitals consist mostly of p(C) orbitals from the pi-bonding system. The orbitals above -3 eV occur mainly from the interaction between Fe orbitals and ligand p orbitals. The HOMO is contributed by mainly d(Fe) and p(C) orbitals, showing the characteristic bonding between the metallic d-orbitals and the pi-system.

Figure 27 depicts the DOS of the adsorption systems, with the ferrocene adsorbed vertically or horizontally on the Ag(111) surface. In vertical adsorption, an orbital overlap between the surface and adsorbate is observed from -8 eV and forward, particularly between the d(Ag) and the p(C) orbitals. Small contributions

from $s(\text{H})$, $d(\text{Fe})$, $s(\text{Ag})$, and $p(\text{Ag})$ are also present. A small peak from $d(\text{Fe})$ is observed around -0.8 eV, overlapping with $p(\text{C})$ and $d(\text{Ag})$ orbitals. The negative adsorption energy and the overlap between the $p(\text{C})$ and Ag orbitals, especially the d -orbital, is an indication of the formation of a chemical interaction occurring largely between the π -bonds in the ring, and the Ag d -orbitals. The horizontally adsorbed ferrocene system exhibits a similar profile but with a shift in the energies of the Fe , C , and H orbitals lying approximately 0.5 eV higher in energy. This could be a numerical error, or a consequence of change due to the electric field of the surface. The contribution from iron orbitals is minimal in both spectra, indicating limited interaction, reasonably due to steric hindrance posed by the rings in both configurations.

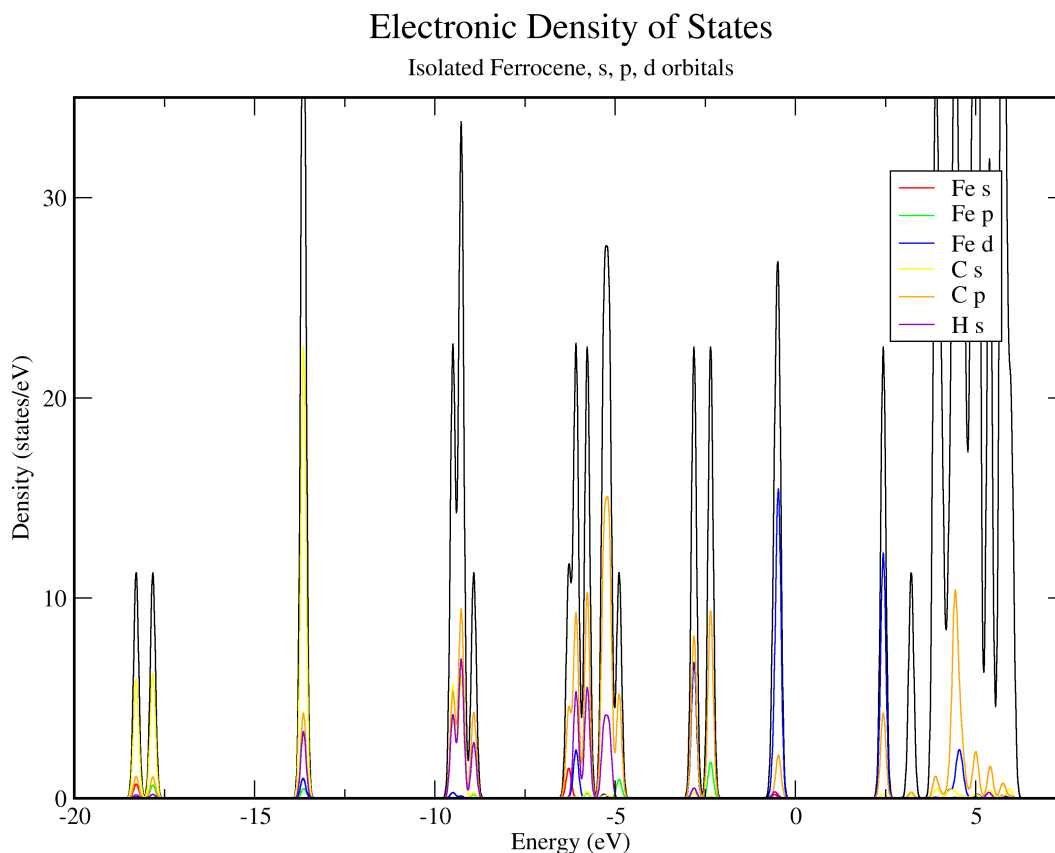


Figure 26: Electronic density of states showing the s,p, and d orbitals in Fe , C , and H in ferrocene.

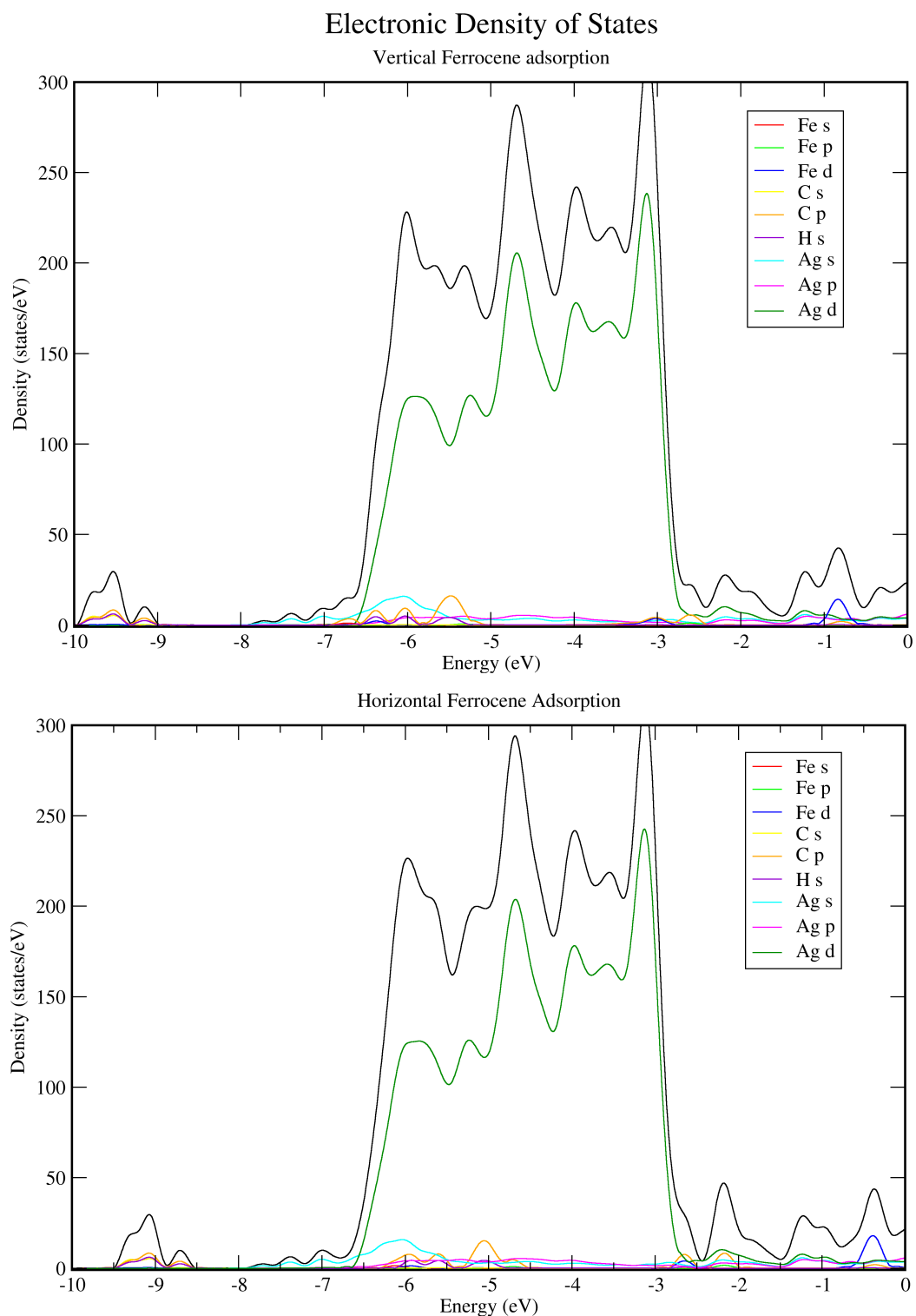


Figure 27: Electronic density of states of the adsorption systems, showing the Ag, Fe, C, and H orbital contributions.

6.4.2 Bader charge analysis

The Bader charges in the gas phase ferrocene and the horizontally and vertically adsorbed ferrocene is compiled in Table 8. No charge transfer is seen between the surface and a specific atom. Therefore, I looked into the change in the charge of the whole ferrocene molecule. The charge of the isolated ferrocene molecule is 58.00 and remains the same for both horizontal and vertical adsorption. This, along with the long adsorption distances, suggests no significant charge transfer upon adsorption, indicating the adsorption occurs through weak long-range interactions.

Table 8: Bader charges of the elements and the ferrocene molecule of the gas phase and adsorbed ferrocene.

	Gas phase	Vertical	Horizontal
Ag	-	11.00	11.00
Fe	7.26	7.27	7.27
C	4.14	4.15	4.15
H	0.93	0.92	0.92
Ferrocene	58.00	58.00	58.00

6.5 Vertical ferrocene surface decomposition

From the vertically adsorbed ferrocene, the decomposition to form Fe, FeCp, and Cp fragments on the surface was investigated. To better understand the adsorption of fragments, the adsorptions of a Fe atom, Cp ring, and FeCp complex were investigated. The Fe and Cp fragments were adsorbed to the Ag(111) surface, at the same four adsorption sites on-top, hcp hollow, fcc hollow, and bridging position. The FeCp was adsorbed with Fe facing down and up from the surface. It was adsorbed in the fcc position, as this was the most favourable position for both the Fe and Cp ring.

6.5.1 Fe adsorption

The isolated Fe in the gas phase was calculated, using a cutoff of 500 eV after convergence. Since the system possessed magnetisation of 4.0, spin polarisation was considered.

For the ferrocene adsorption, the cutoff energy was set to 550 eV. Spin polarisation was considered, and the system possessed magnetisation of 3.5. The change in magnetisation compared to the gas phase signifies half an electron has been donated from Fe to the surface. This was further investigated using a Bader charge analysis. The Bader analysis of the gas phase Fe was 8.00, and for the adsorbed Fe 7.67. This shows a small electron donation from Fe to the surface. The average charge of the silver atoms in the crystal was 11.00, indicating that the donated charge distributes throughout the crystal. The adsorption energies of the iron atom are compiled in Table 9, and the adsorptions are visualised in Figure 28. The iron atom adsorbs near the surface, at distances around 1.81-1.82 Å. The adsorption energies take large negative values, which indicates the adsorption might involve a chemical bond. To investigate this further, a density of state analysis was performed, visualised in Figure 29. It shows an overlap of d(Fe) and Ag orbitals, with a large d(Fe) peak around -2.7 eV, further indicating the occurrence of a chemical bond. The results from the adsorption energy, DOS, and Bader analysis indicate Fe binds chemically to the Ag surface.

Table 9: Initial and final adsorption sites, adsorption energy (E_{ads}), and Fe-Ag distance to the surface of the adsorption of Fe on the Ag(111) surface.

Fe adsorption			
Initial site	Final site	E_{ads} (kJ/mol)	Ag-Fe (Å)
On-top	hollow _{fcc}	-278.4	1.81
hollow _{hcp}	hollow _{hcp}	-277.3	1.82
hollow _{fcc}	hollow _{fcc}	-278.4	1.81
bridge	hollow _{hcp}	-277.3	1.81

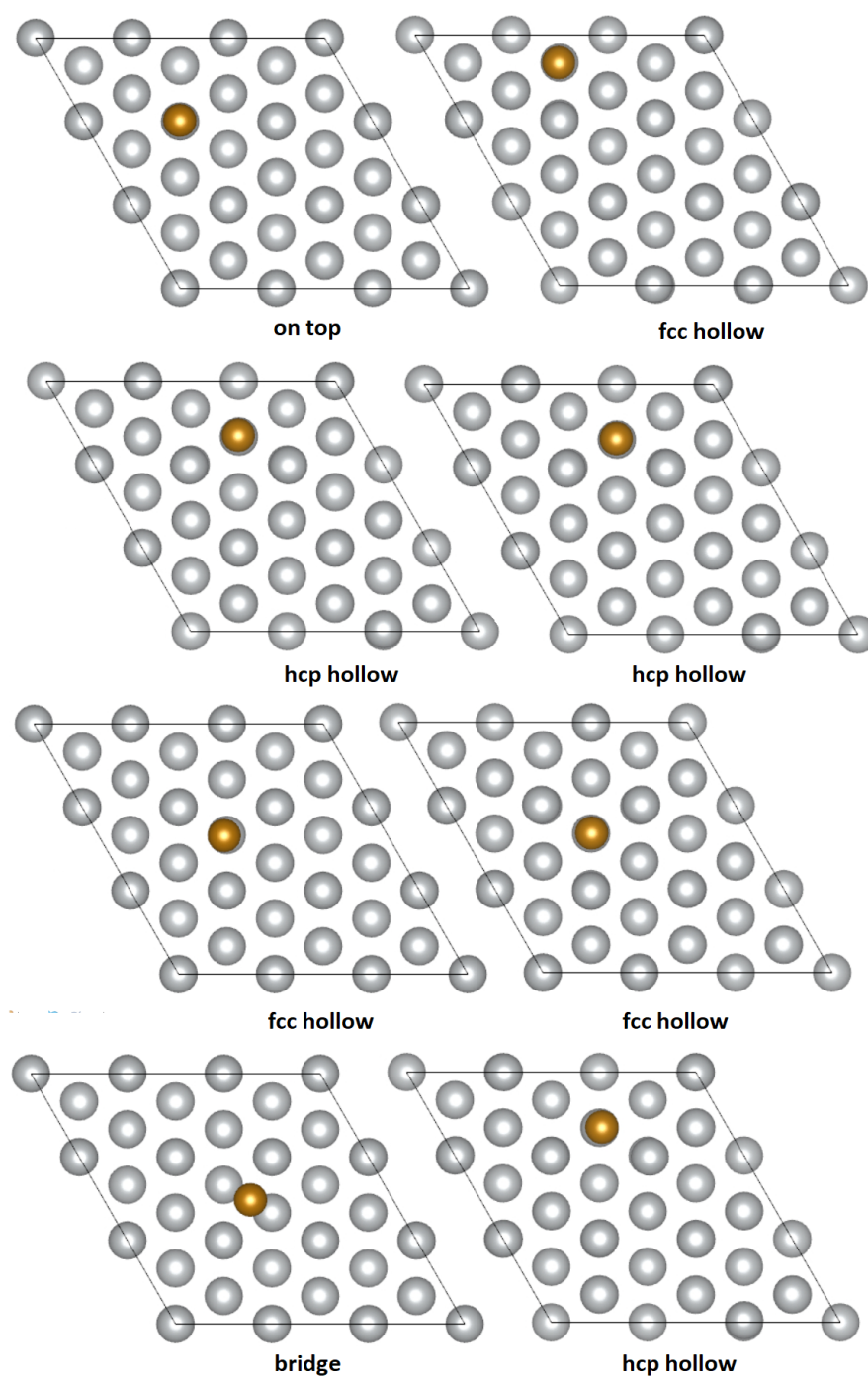


Figure 28: Top view of the initial on-top, hcp hollow, fcc hollow, and bridging and final adsorption positions of Fe.

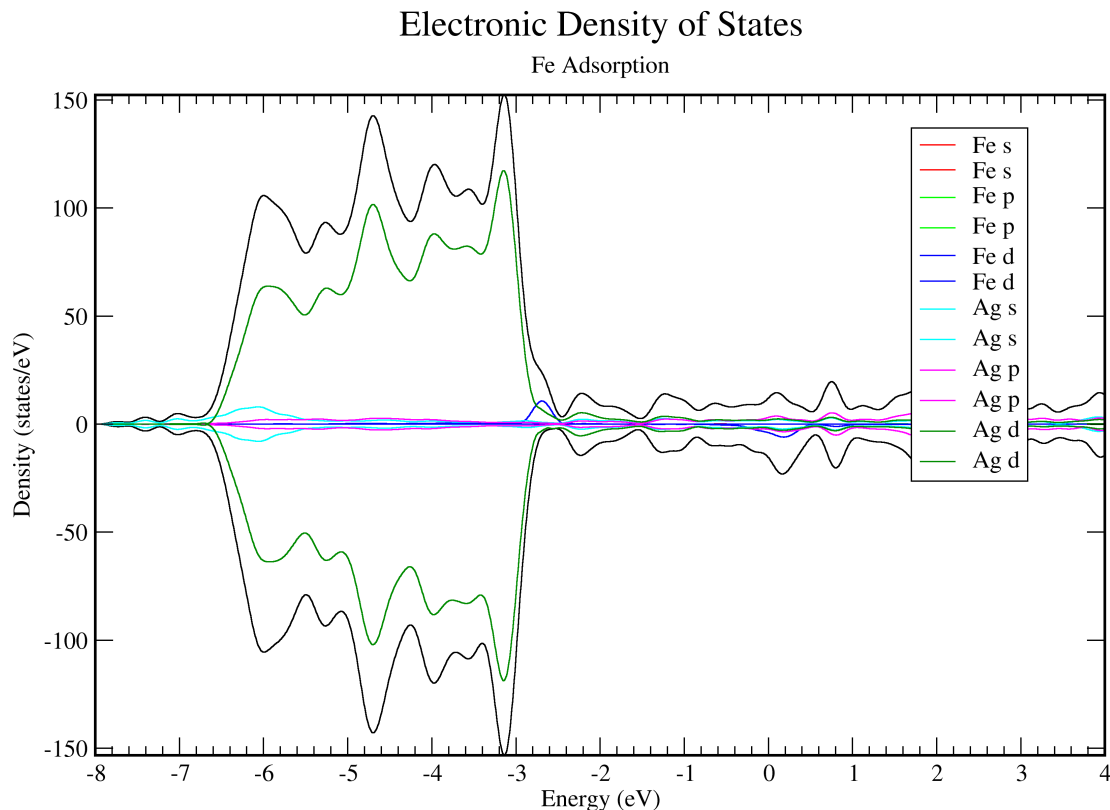


Figure 29: Electronic density of states of the adsorbed Fe.

6.5.2 Cp adsorption

For the adsorption of a neutral Cp radical on the surface, the gas phase Cp was calculated. The cutoff energy was converged and set to 900 eV. The system possessed magnetisation of 1.0, whereas spin polarisation was considered.

The adsorption energies of Cp are compiled in Table 10, and the adsorptions are visualised in Figure 30. The adsorption system did not possess magnetisation, which signifies that there could be a charge transfer between the surface and the adsorbate. This, along with a low adsorption energy is an indication of a possible chemical bond. It was further investigated with Bader analysis. In the gas phase neutral Cp radical, C had an average charge of 4.06 and H of 0.94, and the whole molecule had a charge of 25.00. For the adsorption system, C had an average charge of 4.13, H of 0.93, and Ag of 11.0. This suggests that the surface donates charges of an average of 0.07 to C and 0.01 to C H. The total charge for the adsorbed Cp ring was 25.30, showing charge donation from the surface. As no difference in charge is seen in the crystal, the electron deficiency is reasonably distributed throughout the

silver crystal. It is highly reasonable that a Cp radical would accept an electronic charge from the surface, as this would produce the aromatically stabilised Cp^- anion, and the Ag crystal has a larger volume to distribute the charge deficiency. DOS shows an overlap between $p(\text{C})$, $s(\text{H})$, and Ag orbitals around -5.5 and -5.0 eV, indicating a possible hybridisation of the orbitals, as visualised in Figure 31.

Table 10: Initial and final adsorption sites, adsorption energy (E_{ads}) in kJ/mol, and C-Ag and H-Ag distance (\AA) to the surface of the adsorption of the neutral Cp radical on the Ag(111) surface. The average bond lengths of the C and H species in the rings and the average of all the Ag atoms on the first surface layer were used to calculate the adsorption distances of the vertical adsorption. The adsorption energies are given for the optimised structure at 550 eV cutoff (opt) and the single point calculation at 900 eV cutoff (sp). The bond distances are from the single-point calculation.

Cp adsorption				
Initial site	$E_{ads}(\text{opt})$	$E_{ads}(\text{sp})$	Ag-C (\AA)	Ag-H (\AA)
On-top	-181.4	-179.0	2.53	2.67
hollow _{hcp}	-180.2	-177.8	2.53	2.68
hollow _{fcc}	-181.4	-179.0	2.52	2.67
bridge	-177.5	-175.1	2.52	2.68

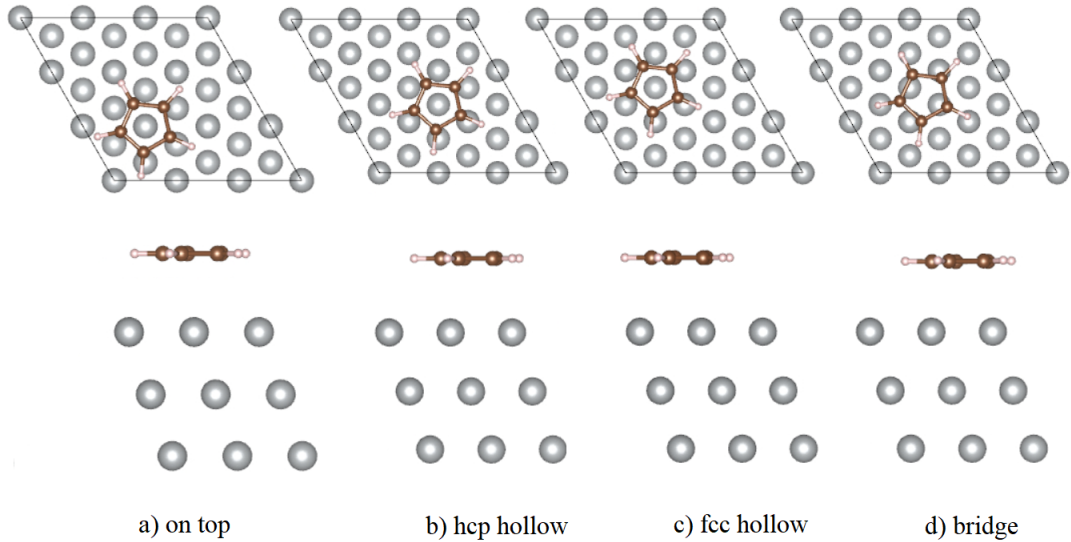


Figure 30: Side and top view of the on-top, hcp hollow, fcc hollow, and bridging adsorption positions of a neutral Cp radical.

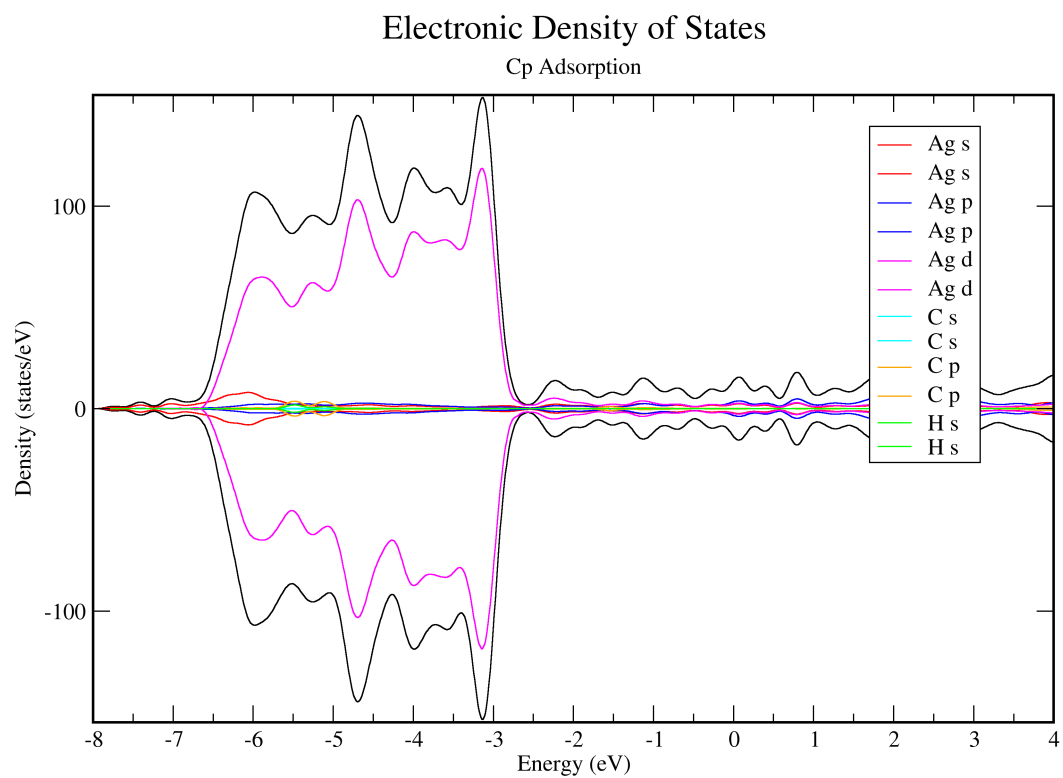


Figure 31: Electronic density of states of the adsorbed, neutral Cp ring.

6.5.3 FeCp adsorption

The adsorption of the neutral FeCp was modelled with Fe facing upwards, and downwards, using a cutoff of 550 eV and 5x5x1 k-points, following a single-point calculation at a cutoff of 900 eV. As the fcc hollow position was the most favorable for both Cp and Fe, the FeCp adsorption only considered this site. The adsorptions are visualised in Figure 32. The adsorption energies and Ag-Fe, Ag-C, and Ag-H distances are compiled in Table 11. The results show that the adsorption with Fe facing down to the surface is 263 kJ/mol more favourable. It should be noted that magnetism has not been considered for the surface adsorptions, and that consideration of spin polarisation might lead to differences in the results.

Table 11: Adsorption energy (E_{ads}) in kJ/mol, and Fe-Ag, C-Ag, and H-Ag distance (Å) to the surface of the adsorption of the FeCp complexes to the fcc hollow position, with Fe facing up from or down to the surface. For calculation of the adsorption distances of the vertical adsorption, the average bond lengths of the C and H species in the rings and the average of all the Ag atoms on the first surface layer were used. The adsorption energies are given for the optimised structure at 550 eV cutoff (opt) and the single point calculation at 900 eV cutoff (sp). The bond distances are from the single-point calculation.

FeCp adsorption					
Species	$E_{ads}(opt)$	$E_{ads}(sp)$	Ag-Fe (Å)	Ag-C (Å)	Ag-H (Å)
FeCp (Fe up)	-23.0	-20.2	4.35	2.78	2.81
FeCp (Fe down)	-286.2	-283.9	1.78	3.42	3.38

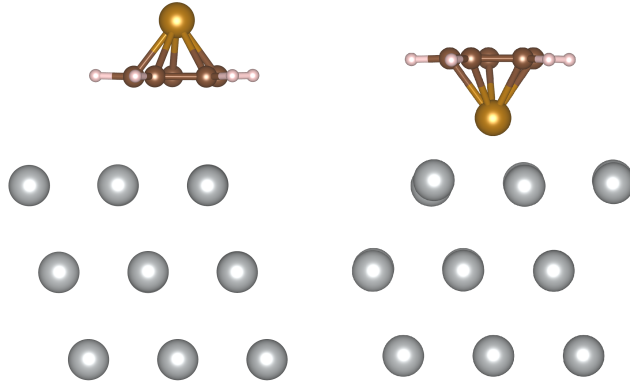


Figure 32: Side view of the FeCp adsorption at the fcc hollow position, with Fe facing upwards (left), and downwards (right).

The adsorption energy of Fe, Cp, and FeCp with Fe facing downwards takes large negative values, meaning they are more energetically favourable than the adsorption of ferrocene. This suggests that if the molecule decomposes, it will be difficult to remove the fragments from the surface. As Fe and FeCp have more negative adsorption energy than the Cp ring, they should be more strongly bound to the surface. This could be used as an advantage. For example, a limitation in the CVD method so far is carbon impurities. It could therefore be of interest to investigate if the CVD chamber could be heated or if energy could be provided in another way to desorb the Cp rings after decomposition. If one could find an optimal range where the Cp rings desorb, while Fe remains adsorbed, it could provide a possible way of eliminating carbon impurities in the film. This could be done by providing energy in the range of 179 kJ/mol to 278 kJ/mol, to eliminate the Cp fragment while keeping the FeCp and Fe adsorbed. An example would be to provide above 180 kJ/mol in energy in the form of heating the substrate, after deposition. As FeCp is more strongly adsorbed than Fe, this suggests it might be difficult to remove the FeCp fragment once on the surface, leading to carbon impurities. Further studies could delve deeper into how the Cp ring in the adsorbed FeCp fragment could decompose on or desorb from the surface.

6.5.4 Vertical decomposition

The vertically adsorbed ferrocene could decompose by sliding off one of the Cp rings. The remaining FeCp fragment could then remain adsorbed with the iron facing downwards or upwards from the surface. This was investigated. To add the adsorbates, a larger surface was needed. Thus, a larger surface with an area of 129.2 \AA^2 was modelled. The neutral FeCp and Cp fragments were put on the surface, at fcc positions, represented in Figure. 33.

The adsorption energies and Ag-Fe, Ag-C, and Ag-H bond lengths are compiled in Table 12. The decomposition forming a FeCp fragment with Fe facing towards the surface is more energetically favourable than with Fe facing upwards. It should be noted that magnetism has not been considered for the surface adsorptions, and that consideration of spin polarisation might lead to differences in the results.

For future studies, a nudged elastic band (NEB) analysis could be performed from the adsorbed ferrocene molecule, to adsorbed fragments at neighboring fcc position, and possibly with the Cp fragment at fcc positions further away. This could elucidate the reaction mechanism and possible transition states from the initial structure of the adsorbed ferrocene molecule to the final decomposed structure.

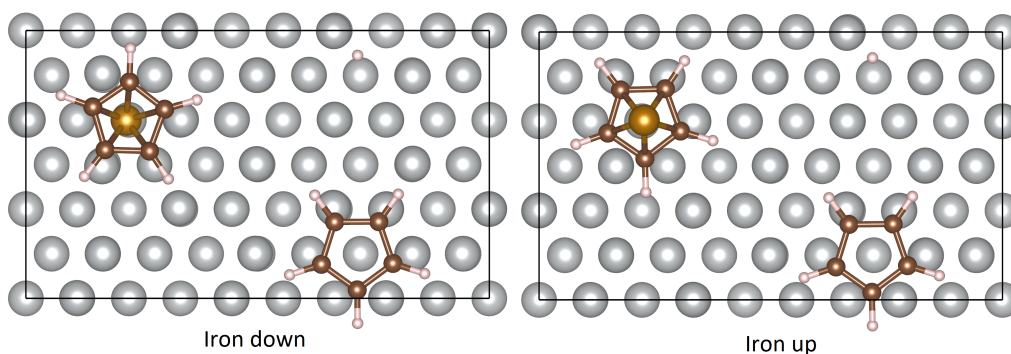


Figure 33: Top view of surface ring dissociation, with the FeCp and Cp fragments at fcc positions on the surface.

Table 12: Adsorption energy (E_{ads}) in kJ/mol of the vertical ferrocene decomposition into Cp and FeCp complexes in fcc hollow positions, with Fe facing up from or down to the surface. The adsorption energies are given for the optimised structure at 550 eV cutoff (opt) and the single point calculation at 900 eV cutoff (sp).

Vertical surface decomposition into Cp + FeCp		
Species	$E_{ads}(\text{opt})$ (kJ/mol)	$E_{ads}(\text{sp})$ (kJ/mol)
Cp + FeCp (Fe up)	-207.2	-207.2
Cp + FeCp (Fe down)	-465.6	-465.6

6.6 Horizontal ferrocene surface decomposition

To evaluate the horizontal surface decomposition, the on-top adsorbed ferrocene was gradually moved closer to the surface, in steps of 0.2 Å, while keeping the z-coordinate of the Fe froze, to evaluate how Fe can bind to the surface and what happens to the Cp⁻ rings. Figure 34 shows images from a selection of decomposition steps. Table 13 shows the adsorption energy, the relative energy compared to the energy of the initial adsorption structure, the Ag-Fe distance, and the H-C-Ag bond angle closest to the surface.

The decomposition from horizontal configuration is energetically unfavourable and has an energy barrier of at least 229 kJ/mol. When the Ag-Fe distance is 2.76 Å, the molecule diffuses from the on-top position to the bridging position. This could be an indication that the molecule is starting to decompose.

None of the decomposition step systems up to 1.8 Å have possessed magnetisation. The stepwise decomposition was stopped after moving the molecule 2.0 Å closer to the surface, from its optimum position, due to limitations in time. For the last step, it should be noted that magnetism has not been considered, and that consideration of spin polarisation might lead to differences in the results.

The Cp rings do not seem to dissociate from the molecule on their own, whereas a continuation to reach full decomposition would possibly need to be induced by manually releasing the rings from the structure after the system has reached a local energy minimum, or when the Ag-Fe distance is close to that of an adsorbed Fe atom (1.8 Å). To understand the decomposition mechanism further, a NEB analysis could be performed.

Table 13: Relative energies (ΔE), Adsorption energies (E_{ads}), Ag-Fe bond lengths and H-C-Ag bond angle of the horizontal decomposition steps. The Fe-Ag bond length was evaluated between Fe and the closest surface Ag. The H-C-Ag angle is between the H closest to a surface Ag, and the adjacent C.

Step (\AA)	ΔE (kJ/mol)	E_{ads} (kJ/mol)	Ag-Fe (\AA)	H-C-Ag ($^\circ$)
0.0	0.0	-71.8	4.40	125.5
0.2	2.8	-69.0	4.23	125.5
0.4	10.9	-60.9	4.05	125.8
0.6	25.2	-46.6	3.86	126.2
0.8	46.7	-25.1	3.66	127.2
1.0	76.3	4.5	3.45	128.3
1.2	115.1	43.3	3.25	131.8
1.4	163.5	91.7	3.06	133.9
1.6	220.9	149.0	2.97	134.2
1.8	228.9	157.1	2.76	146.5
2.0	283.2	211.4	2.54	140.3

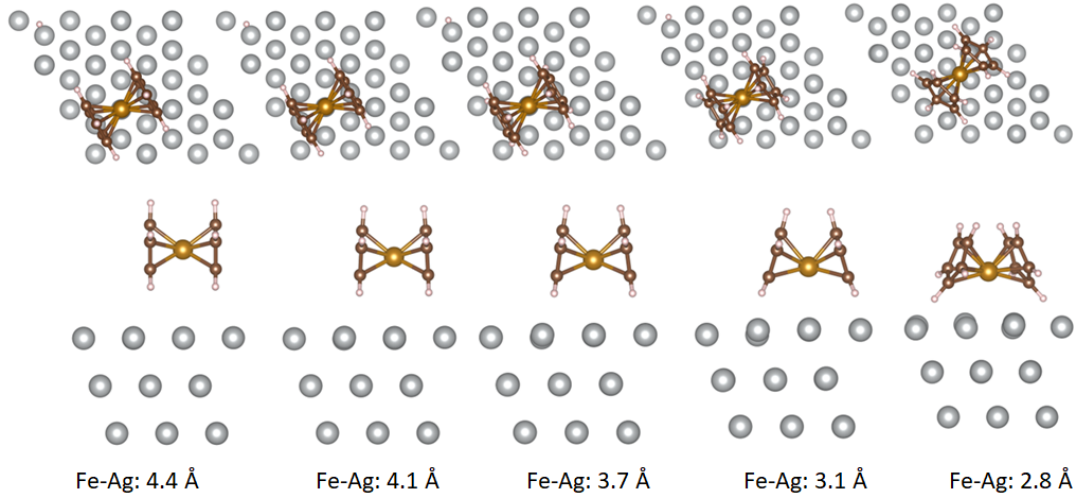


Figure 34: Side and top view of a selection of the decomposition steps of the horizontal decomposition.

7 Concluding Remarks & Future Outlook

In this thesis, I have examined the ferrocene gas phase and surface chemistry in a recently developed CVD method to form metallic thin films using plasma electrons as reducing agents. The gas phase ion formation and dissociation of ferrocene were examined to elucidate possible reactions and film-contributing species. The results show that it gets successively easier to dissociate ferrocene when it has gained electrons, with the electronic energy decreasing from 397 to 174, to -85 kJ/mol for the dissociation of FeCp_2 , FeCp_2^- and FeCp_2^{2-} , respectively. The dissociation of FeCp_2^{2-} into FeCp^- and Cp^- shows a release in energy. The dissociation of one ring was energetically favourable for all species. The formation of positive ions is energetically unfavourable and thus considered improbable.

The ion formation and decomposition reaction pathway depends on the energy of the plasma electrons, which in turn depends on the process parameters, especially the plasma power. In general, the electrons should possess sufficient energy for the FeCp_2^- anion to form and dissociate in the gas phase. However, since the reactions are influenced by both reaction velocity and the number of collisions between electrons and chemical species, considering kinetic and dynamic processes in the gas phase would be of interest for future research. If ionization and dissociation occur in the gas phase, FeCp_2^- , FeCp^- , and Cp^- are identified as the species that likely contribute to surface growth, depending on the electron energy.

For the adsorption of ferrocene on the surface, the vertical and horizontal adsorption and all the four on top, hcp hollow, fcc hollow, and bridging adsorption sites are almost equally probable, all with values close to -72 kJ/mol. Ferrocene adsorbs vertically in the hcp hollow position around 3.0 Å above the surface. Horizontally, it adsorbs with the closest hydrogen 2.5 Å and Fe 4.4 Å above the surface, in the on-top position. The Cp, Fe, and the FeCp with Fe facing towards the surface are more strongly adsorbed to the surface than ferrocene, with values of -179, -279, and -284 kJ/mol, respectively. The vertical decomposition is energetically favourable, while the horizontal decomposition has an energy barrier. Continued investigations would be needed to probe the surface decomposition mechanisms.

To summarise, the electron energy of around 220 kJ/mol would provide sufficient energy for the ion formation of ferrocene to FeCp_2^- , and its dissociation into FeCp and Cp^- fragments in the gas phase, from which the adsorption of the fragments would be energetically favourable. Fe and FeCp with Fe facing towards the surface interact stronger with the surface than Cp and FeCp_2 . It would therefore be worth investigating the possibility of providing energy, suggestively in the form of heat on the substrate, to desorb the unwanted fragments after adsorption and decomposition, to potentially eliminate carbon impurities in the film.

References

- ¹J. E. Greene, “Tracing the 5000-year recorded history of inorganic thin films from 3000 bc to the early 1900s ad.”, *Applied Physics Reviews* **1**, 1–36 (2014).
- ²E. D. Nicholson, “The ancient craft of gold beating.”, *Gold Bulletin* ; volume 12, issue 4, page 161-166 ; ISSN 0017-1557 2190-7579 (1979).
- ³H. Nadhom, *Area selective chemical vapor deposition of metallic films using plasma electrons as reducing agents*. Linköping Studies in Science and Technology. Dissertations: 2147 (Department of Physics, Chemistry and Biology, Linköping University, 2021).
- ⁴K. Seshan, *Handbook of thin-film deposition techniques principles, methods, equipment and applications, 2nd ed.* (Noyes Publications, William Andrew Publishing, Norwich, NY, 2002).
- ⁵L. Yu, S. Kang, O. Jinka, M. Mason, S. Cordes, and L. Romankiw, “Development of electroless nickel-iron plating process for microelectronic applications.”, 2014 IEEE 64th Electronic Components and Technology Conference (ECTC), Electronic Components and Technology Conference (ECTC), 2014 IEEE 64th, 1782–1789 (2014).
- ⁶Vaz, Bland, and Lauhoff, “Magnetism in ultrathin film structures.”, *Reports on Progress in Physics* **71**, 56501 (2008).
- ⁷D. Dimitrov, G. Hadjipanayis, V. Papaefthymiou, and A. Simopoulos, “Magnetic properties and microstructure of fe-o and co-o thin films.”, *IEEE Transactions on Magnetics* **33**, 4363–4366 (1997).
- ⁸W. Kudernatsch, G. Peng, H. Zeuthen, Y. Bai, L. R. Merte, L. Lammich, F. Besenbacher, M. Mavrikakis, and S. Wendt, “Direct visualization of catalytically active sites at the fe-pt(111) interface.”, *ACS Nano* **9**, 7804–7814 (2015).
- ⁹Sun, Qin, Lewandowski, Carrasco, Sterrer., Shaikhutdinov, and Freund, “Monolayer iron oxide film on platinum promotes low temperature co oxidation.”, *Journal of catalysis* **266**, 359–368.
- ¹⁰A. C. Jones and M. L. Hitchman, *Chemical vapour deposition : precursors, processes and applications*. (RSC Pub., 2009).
- ¹¹M. Donald M., *Handbook of physical vapor deposition (pvd) processing*. Vol. 2nd ed (William Andrew, 2010).
- ¹²H. Pedersen and S. Elliott, “Studying chemical vapor deposition processes with theoretical chemistry.”, *Theoretical Chemistry Accounts: Theory, Computation, & Modeling* **133**, 1–10 (2014).

- ¹³A. R. WEST, *Solid state chemistry and its applications second edition* (John Wiley & Sons, Ltd, 2014), pp. 28–29.
- ¹⁴H. Nadhom, R. Boyd, P. Rouf, D. Lundin, and H. Pedersen, “Area selective deposition of metals from the electrical resistivity of the substrate.”, (2021).
- ¹⁵H. Nadhom, D. Lundin, P. Rouf, and H. Pedersen, “Chemical vapor deposition of metallic films using plasma electrons as reducing agents”, *Journal of Vacuum Science & Technology. A. Vacuum, Surfaces, and Films* **38** (2020).
- ¹⁶H. Nadhom, Y. Yuan, P. Rouf, N. Solin, and H. Pedersen, “Area selective deposition of iron films using temperature sensitive masking materials and plasma electrons as reducing agents.”, *Journal of Vacuum Science & Technology A* **39**, 043411 (2021).
- ¹⁷E. S. Phillips, *Ferrocenes. compounds, properties and applications*. Chemical engineering methods and technology (Nova Science Publishers, 2011).
- ¹⁸P. Atkins, T. Overton, J. Rourke, M. Weller, and F. Armstrong, *Shriver and atkins’ inorganic chemistry, fifth edition* (Oxford University Press, 2010).
- ¹⁹J. D. Dunitz, L. E. Orgel, and A. Rich, “The crystal structure of ferrocene”, *Acta Crystallographica* **9**, 373–375 (1956).
- ²⁰G. Miessler, P. Fischer, and D. Tarr, *Inorganic chemistry: pearson new international edition* (Pearson, 2013).
- ²¹G. Frenking and N. Frohlich, “The nature of the bonding in transition-metal compounds.”, *Chemical Reviews* **100**, 717–774 (2000).
- ²²B. W. Pfennig, *Principles of inorganic chemistry*. (Wiley, 2015).
- ²³Z.-F. Xu, Y. Xie, W.-L. Feng, and H. F. Schaefer, “Systematic investigation of electronic and molecular structures for the first transition metal series metallocenes $m(c\ 5h\ 5)\ 2\ (m = v, cr, mn, fe, co, \text{ and } ni)$.”, *Journal of Physical Chemistry A* **107**, 2716–2729 (2003).
- ²⁴M. Swart, “Metal–ligand bonding in metallocenes: differentiation between spin state, electrostatic and covalent bonding.”, *Inorganica Chimica Acta* **360**, 179–189 (2007).
- ²⁵F. N. N. Pansini and F. A. L. de Souza, “Trends in the spin states and mean static dipole polarizability of the group viii metallocenes.”, *The Journal of Physical Chemistry. A* **120**, 2771–2778 (2016).
- ²⁶F. Andersson, “Cvd of iron thin films using plasma electrons as a reducing agent a quantum chemical study”, [Unpublished report], Linköping University (2022).
- ²⁷A. D. Becke, “Density-functional thermochemistry. iii. the role of exact exchange.”, *Journal of Chemical Physics* **98**, 5648 (1993).

- ²⁸C. Lee, W. Yang, and R. Parr, "Development of the colle-salvetti correlation-energy formula into a functional of the electron density.", *Physical Review B* **37**, 785–789 (1988).
- ²⁹E. I. Ioannidis and H. J. Kulik, "Towards quantifying the role of exact exchange in predictions of transition metal complex properties.", (2015).
- ³⁰Y. Zhao and D. Truhlar, "The m06 suite of density functionals for main group thermochemistry, thermochemical kinetics, noncovalent interactions, excited states, and transition elements: two new functionals and systematic testing of four m06-class functionals and 12 other functionals.", *Theoretical Chemistry Accounts* **120**, 215–241 (2008).
- ³¹J. Perdew, K. Burke, and M. Ernzerhof, "Generalized gradient approximation made simple.", *Physical Review Letters* **77**, 3865–3868 (1996).
- ³²J. Perdew, K. Burke, and M. Ernzerhof, "Erratum: generalized gradient approximation made simple (physical review letters (1996) 77 (3865)).", *Physical Review Letters* **78**, 1396 (1997).
- ³³R. Ditchfield, W. Hehre, and J. Pople, "Self-consistent molecular-orbital methods. ix. an extended gaussian-type basis for molecular-orbital studies of organic molecules.", *The Journal of Chemical Physics* **54**, 720–723 (1971).
- ³⁴H. Nadhom, Y. Yuan, P. Rouf, N. Solin, and H. Pedersen, "Area selective deposition of iron films using temperature sensitive masking materials and plasma electrons as reducing agents.", *Journal of Vacuum Science & Technology A* **39**, 043411 (2021).
- ³⁵F. Weigend and R. Ahlrichs, "Balanced basis sets of split valence, triple zeta valence and quadruple zeta valence quality for h to rn: design and assessment of accuracy.", *Physical Chemistry Chemical physics -Cambridge- Royal Society of Chemistry* **7**, 3297–3305 (2005).
- ³⁶S. Grimme, J. Antony, S. Ehrlich, and H. Krieg, "A consistent and accurate ab initio parametrization of density functional dispersion correction (dft-d) for the 94 elements h-pu.", *Journal of Chemical Physics* **132**, 154104 (2010).
- ³⁷S. Coriani, A. Haaland, T. Helgaker, and P. Jorgensen, "The equilibrium structure of ferrocene.", *ChemPhysChem* **7**, 245–249 (2006).
- ³⁸A. Haaland and J. Nilsson, "The determination of the barrier to internal rotation in ferrocene and ruthenocene by means of electron diffraction.", *Chemical Communications (London)*, 88–89 (1968).
- ³⁹R. K. Bohn and A. Haaland, "On the molecular structure of ferrocene, $\text{Fe}(\text{C}_5\text{H}_5)_2$ ", *Journal of Organometallic Chemistry* **5**, 470–476 (1966).

- ⁴⁰N. Mohammadi, A. Ganesan, C. T. Chantler, and F. Wang, "Differentiation of ferrocene d5d and d5h conformers using ir spectroscopy.", *Journal of Organometallic Chemistry* **713**, 51–59 (2012).
- ⁴¹U. Hohm, D. Goebel, and S. Grimme, "Experimental and theoretical study of the dipole polarizability of ferrocene $\text{Fe}(\text{C}_5\text{H}_5)_2$.", *Chemical Physics Letters* **272**, 328–334 (1997).
- ⁴²S. Islam and F. Wang, "A comparative study of energetics of ferrocenium and ferrocene.", *Preprints*, 10.20944/preprints201808.0166.v1 (2018).
- ⁴³M. Ryan, J. Eyler, and D. Richardson, "Adiabatic ionization energies, bond disruption enthalpies, and solvation free energies for gas-phase metallocenes and metallocenium ions.", *Journal of the American Chemical Society* **114**, 8611–8619 (1992).
- ⁴⁴C. Waldfried, D. Welipitiya, C. Hutchings, H. De Silva, G. A. Gallup, P. A. Dowben, W. Pai, J. Zhang, J. Wendelken, and N. Boag, "Preferential bonding orientations of ferrocene on surfaces", *The Journal of Physical Chemistry B* **101**, 9782–9789 (1997).
- ⁴⁵D. Welipitiya, P. Dowben, J. Zhang, W. Pai, and J. Wendelken, "The adsorption and desorption of ferrocene on $\text{Ag}(100)$ ", *Surface Science* **367**, 20–32 (1996).
- ⁴⁶D. Welipitiya, A. Green, J. P. Woods, P. A. Dowben, B. W. Robertson, D. Byun, and J. Zhang, "Ultraviolet and electron radiation induced fragmentation of adsorbed ferrocene.", *JOURNAL OF APPLIED PHYSICS* **79**, 8730–8734 (1996).
- ⁴⁷C. M. Woodbridge, D. L. Pugmire, R. C. Johnson, N. M. Boag, and M. A. Langgell, "HREELS and xps studies of ferrocene on $\text{Ag}(100)$ ", *The Journal of Physical Chemistry B* **104**, 3085–3093 (2000).
- ⁴⁸M. Ormaza, P. Abufager, N. Bachellier, R. Robles, M. Verot, T. Le Bahers, M.-L. Bocquet, N. Lorente, and L. Limot, "Assembly of ferrocene molecules on metal surfaces revisited", *The Journal of Physical Chemistry Letters* **6**, 395–400 (2015).
- ⁴⁹B. Özdamar, C. Massobrio, and M. Boero, "Stability and destabilization processes in the formation of ferrocene-based metal–organic molecule–metal nanojunctions", *The Journal of Physical Chemistry C* **120**, 13825–13830 (2016).
- ⁵⁰R. Paul, R. G. Reifenberger, T. S. Fisher, and D. Y. Zemlyanov, "Atomic layer deposition of FeO on $\text{Pt}(111)$ by ferrocene adsorption and oxidation", *Chemistry of Materials* **27**, 5915–5924 (2015).

- ⁵¹J. Reimers and D. Wang Y.and Kosov, “Decomposition of ferrocene on pt(111) and its effect on molecular electronic junctions.”, Journal of Physical Chemistry C (2019).
- ⁵²K.-F. Braun, V. Iancu, N. Pertaya, K.-H. Rieder, and S.-W. Hla, “Decompositional incommensurate growth of ferrocene molecules on a au(111) surface”, Phys. Rev. Lett. **96**, 246102 (2006).
- ⁵³J. Meyer, T. Bredow, C. Tegenkamp, and H. Pfnür, “Thiol and thiolate bond formation of ferrocene-1,1-dithiol to a ag(111) surface”, The Journal of Chemical Physics **125**, 194705 (2006).
- ⁵⁴L. Atkinson, J. Lipton-Duffin, J. MacLeod, V. Jayalatharachchi, and T. Liao, “1d coordination polymers of 1,1'-dibromoferrocene following debromination on ag(111).”, Journal of Physical Chemistry C (2022).
- ⁵⁵O. Schaff, V. Fernandez, P. Hofmann, K.-M. Schindler, A. Theobald, V. Fritzsche, A. Bradshaw, R. Davis, and D. Woodruff, “Coverage-dependent changes in the adsorption geometry of benzene on ni111”, Surface Science **348**, 89–99 (1996).
- ⁵⁶E. Germán, S. Simonetti, E. Pronso, A. Juan, and G. Brizuela, “C-c5h5 on a ni(111) surface: theoretical study of the adsorption, electronic structure and bonding”, Applied Surface Science **254**, 5831–5836 (2008).
- ⁵⁷W. W. Pai, Z. Zhang, J. Zhang, and J. F. Wendelken, “Direct visualization in manipulation of stable molecular radicals at room temperature”, Surface Science **393**, L106–L112 (1997).
- ⁵⁸B. W. Heinrich, L. Limot, M. V. Rastei, C. Iacovita, J. P. Bucher, D. M. Djimbi, C. Massobrio, and M. Boero, “Dispersion and localization of electronic states at a ferrocene/cu(111) interface”, Phys. Rev. Lett. **107**, 216801 (2011).
- ⁵⁹W. Koch and M. C. Holthausen, *A chemist’s guide to density functional theory*. (Wiley, 2001).
- ⁶⁰M. Born and R. Oppenheimer, “Zur quantentheorie der molekeln”, Annalen der Physik, 457–484 (1927).
- ⁶¹E. G. Lewars, *Computational chemistry: introduction to the theory and applications of molecular and quantum mechanics. third edition*. (Springer Nature, 2016).
- ⁶²V. Fock, “Näherungsmethode zur lösung des quantenmechanischen mehrkörper-problems”, Zeitschrift für Physik **61**, 126–148 (1930).
- ⁶³D. R. Hartree, “The wave mechanics of an atom with a non-coulomb central field. part i. theory and methods”, Mathematical Proceedings of the Cambridge Philosophical Society **24**, 89–110 (1928).

- ⁶⁴P. W. Atkins, J. De Paula, and R. Friedman, *Physical chemistry : quanta, matter, and change*. (Oxford university Press, 2014).
- ⁶⁵P. Hohenberg and W. Kohn, “Inhomogeneous electron gas”, *Phys. Rev.* **136**, B864–B871 (1964).
- ⁶⁶W. Kohn and L. J. Sham, “Self-consistent equations including exchange and correlation effects”, *Phys. Rev.* **140**, A1133–A1138 (1965).
- ⁶⁷P. Joseph W. Ochterski, *Vibrational analysis in gaussian*. Gaussian, Inc. 1999-08-29. Minor updates: 2018-06-17, 2020-08-20. Available at <https://gaussian.com/vib/> (retrieved 2022-01-02).
- ⁶⁸P. Joseph W. Ochterski, *Thermochemistry in gaussian*. Gaussian, Inc. 2000-04-19. Available at <https://gaussian.com/thermo/> (retrieved 2022-01-02).
- ⁶⁹P. Atkins and R. S. Friedman, *Molecular quantum mechanics* (Oxford University Press Inc., 2011).
- ⁷⁰A. R. Leach, *Molecular modelling principles and applications 2nd ed.* (1996, 2001), p. 138.
- ⁷¹P. W. Atkins, J. De Paula, and J. Keeler, *Atkins’ physical chemistry*. (Oxford University Press, 2018).
- ⁷²R. A. Evarestov, *Quantum chemistry of solids: the lcao first principles treatment of crystals* (Springer-Verlag Berlin Heidelberg, 2007), p. 8.
- ⁷³P. Blöchl, “Projector augmented-wave method.”, *Physical Review. B, Condensed matter* **50**, 17953–17979 (1994).
- ⁷⁴G. Henkelman, A. Arnaldsson, and H. Jónsson, “A fast and robust algorithm for bader decomposition of charge density.”, *Computational Materials Science* **36**, 354–360 (2006).
- ⁷⁵R. Dennington, T. A. Keith, and J. M. Millam, *Gaussview Version 6*, 2019.
- ⁷⁶M. J. Frisch, G. W. Trucks, H. B. Schlegel, G. E. Scuseria, M. A. Robb, J. R. Cheeseman, G. Scalmani, V. Barone, G. A. Petersson, H. Nakatsuji, X. Li, M. Caricato, A. V. Marenich, J. Bloino, B. G. Janesko, R. Gomperts, B. Mennucci, H. P. Hratchian, J. V. Ortiz, A. F. Izmaylov, J. L. Sonnenberg, D. Williams-Young, F. Ding, F. Lipparini, F. Egidi, J. Goings, B. Peng, A. Petrone, T. Henderson, D. Ranasinghe, V. G. Zakrzewski, J. Gao, N. Rega, G. Zheng, W. Liang, M. Hada, M. Ehara, K. Toyota, R. Fukuda, J. Hasegawa, M. Ishida, T. Nakajima, Y. Honda, O. Kitao, H. Nakai, T. Vreven, K. Throssell, J. A. Montgomery Jr., J. E. Peralta, F. Ogliaro, M. J. Bearpark, J. J. Heyd, E. N. Brothers, K. N. Kudin, V. N. Staroverov, T. A. Keith, R. Kobayashi, J. Normand, K. Raghavachari, A. P. Rendell, J. C. Burant, S. S. Iyengar, J. Tomasi, M. Cossi, J. M. Millam, M. Klene, C. Adamo, R. Cammi, J. W. Ochterski, R. L.

- Martin, K. Morokuma, O. Farkas, J. B. Foresman, and D. J. Fox, *Gaussian 16*, Gaussian Inc. Wallingford CT, 2016.
- ⁷⁷H. Koch, P. Jo, and T. Helgaker, “The molecular structure of ferrocene.”, *Journal of Chemical Physics* **104**, 9528 (1996).
- ⁷⁸C. Timothy, S. Paul von Ragué, C. Jayaraman, and S. Günther W., “Efficient diffuse function-augmented basis sets for anion calculations. iii. the 3-21+g basis set for first-row elements, li-f.”, *Journal of Computational Chemistry* **4**, 294–301 (1983).
- ⁷⁹J. E. Bartmess, “Thermodynamics of the electron and the proton”, *The Journal of Physical Chemistry* **98**, 6420–6424 (1994).
- ⁸⁰J. J. Fifen, “Thermodynamics of the electron revisited and generalized”, *Journal of Chemical Theory and Computation* **9**, 3165–3169 (2013).
- ⁸¹H. Monkhorst and J. Pack, “Special points for brillouin-zone integrations”, *Physical Review B* **13**, 5188–5192 (1976).
- ⁸²H. Valencia, M. Kohyama, S. Tanaka, and H. Matsumoto, “Ab initio study of EMIM-BF₄ molecule adsorption on li surfaces as a model for ionic liquid/li interfaces in li-ion batteries”, *Phys. Rev. B* **78**, 205402 (2008).
- ⁸³M. Swart, A. R. Groenhof, A. W. Ehlers, and K. Lammertsma, “Validation of exchange-correlation functionals for spin states of iron complexes.”, *Journal of Physical Chemistry A* **108**, 5479–5483 (2004).
- ⁸⁴T. Gryaznova, S. Katsyuba, V. Milyukov, and O. Sinyashin, “Dft study of substitution effect on the geometry, ir spectra, spin state and energetic stability of the ferrocenes and their pentaphospholyl analogues.”, *Journal of Organometallic Chemistry* **695**, 2586–2595 (2010).
- ⁸⁵A. Haaland and J. Nilsson, “The determination of barriers to internal rotation by means of electron diffraction. ferrocene and ruthenocene.”, *Acta Chemica Scandinavica* **22**, 2653–2670 (1968).
- ⁸⁶A. V. Mitin, J. Baker, and P. Pulay, “An improved 6-31G* basis set for first-row transition metals”, *The Journal of Chemical Physics* **118**, 7775–7782 (2003).
- ⁸⁷M. Toma, T. Kuvek, and V. Vrček, “Ionization energy and reduction potential in ferrocene derivatives: comparison of hybrid and pure dft functionals”, *The Journal of Physical Chemistry A* **124**, 8029–8039 (2020).
- ⁸⁸L. F. P. and T. J. C., “Stabilization in cyclopentadienyl, cyclopentenyl, and cyclopentyl cations.”, *Journal of the American Chemical Society* **97**, 1579–1580 (1975).

- ⁸⁹M. McKee, “Theoretical study of iron-ligand binding. mechanism of ferrocene formation from iron plus cyclopentadiene.”, *Journal of Physical Chemistry* **96**, 1683-1690 –1690 (1992).
- ⁹⁰L. G. Allan Gahan Blackman, *Aylward and findlay’s si chemical data* (Wiley, 2014).
- ⁹¹R. Gleiter, M. C. Bohm, and R. D. Ernst, “The he(i) photoelectron spectrum of bis(pentadienyl) iron: a comparison with the ferrocene spectrum”, *Journal of Electron Spectroscopy and Related Phenomena* **33**, 269–278 (1984).
- ⁹²R. N. McDonald, E. J. J. Bianchina, and C. C. Tung, “Electron photodetachment of cyclopentadienylidene anion radical in a flowing afterglow apparatus: ea and hfio of cyclopentadienylidene”, *Journal of the American Chemical Society* **113**, 7115–7121 (1991).
- ⁹³N. Rieke, S. Eustis, and K. Bowen, “Combined experimental and theoretical study of deprotonated ferrocene: anion photoelectron spectroscopy and density functional calculations.”, *International Journal of Mass Spectrometry* **357**, 63-65 –65 (2014).
- ⁹⁴J. P. Puttemans, G. P. Smith, and D. M. J. Golden, *Journal of Physical Chemistry* **94** (1990).
- ⁹⁵S. Grimme, “Semiempirical gga-type density functional constructed with a long-range dispersion correction”, *Journal of Computational Chemistry* **27**, 1787–1799 (2006).
- ⁹⁶K. Kambe, “Cohesive energy of noble metals”, Harvard University, Cambridge, Massachusetts **99** (1955).
- ⁹⁷V. L, *Physical Review* **18** (1921).
- ⁹⁸A. Ambrosetti and P. L. Silvestrelli, “Cohesive properties of noble metals by van der waals–corrected density functional theory: au, ag, and cu as case studies”, *Phys. Rev. B* **94**, 045124 (2016).
- ⁹⁹M. G. Sandoval, J. Walia, M. S. Houache, Y. Abu-Lebdeh, P. Berini, R. Faccio, and A. Weck, “Co2 adsorption and activation on ag(111) surfaces in the presence of surface charge density: a static gas phase dft study”, *Applied Surface Science* **610**, 155498 (2023).
- ¹⁰⁰W. M. W.R. Tyson, *Surf. Sci.* **62** **267**. (1977).
- ¹⁰¹F. de Boer, R. Boom, W. Mattens, A. Miedema, and A. Niessen, “Cohesion in metals: transition metal alloys”, North-Holland, Amsterdam (1988).

8 Appendix

8.1 Appendix A.

Appendix A compiles the calculated electronic energies of the investigated species and multiplicities (Mult.) in Tables A1-A4. The relative energies of the investigated electronic spin states are shown in Table A5. Table A6 compiles the Fe-C, C-C, and C-H bond lengths of the lowest-energy structures and electronic spin states. All species were calculated at the def2tzvp/6-311G(2df,2pd) level, with Grimmes D3 dispersion correction.

Table A1: Electronic energy of the investigated ferrocene (FeCp_2) and ions.

Species	Mult.	E(kJ/mol)
FeCp_2	1	-4334684.118
FeCp_2	3	-4334601.420
FeCp_2	5	-4334607.324
FeCp_2	7	-4334313.240
FeCp_2^-	2	-4334617.521
FeCp_2^-	4	-4334602.067
FeCp_2^-	6	-4334544.505
FeCp_2^-	8	-4334133.842
FeCp_2^{2-}	1	-4333968.811
FeCp_2^{2-}	3	-4334066.428
FeCp_2^{2-}	5	-4334067.433
FeCp_2^{2-}	7	-4333985.321
FeCp_2^+	2	-4334004.484
FeCp_2^+	4	-4333976.653
FeCp_2^+	6	-4333898.690
FeCp_2^+	8	-4333547.187
FeCp_2^{2+}	1	-4332594.275
FeCp_2^{2+}	3	-4332877.427
FeCp_2^{2+}	5	-4332749.413
FeCp_2^{2+}	7	-4332667.577

Table A2: Electronic energy of the investigated iron (Fe) and ions.

Species	Mult.	E(kJ/mol)
Fe	1	-3317500.190
Fe	3	-3317745.401
Fe	5	-3317786.647
Fe	7	-3317453.467
Fe^+	2	-3316225.451
Fe^+	4	-3317060.234
Fe^+	6	-3317067.449
Fe^+	8	-3316311.448
Fe^{2+}	1	-3315098.426
Fe^{2+}	3	-3315235.760
Fe^{2+}	5	-3315477.325
Fe^{2+}	7	-3315034.178
Fe^{3+}	2	-3311824.746
Fe^{3+}	4	-3312068.513
Fe^{3+}	6	-3312435.770
Fe^{3+}	8	-3306245.586
Fe^-	2	-3317042.058
Fe^-	4	-3317857.437
Fe^-	6	-3317589.675
Fe^-	8	-3317209.227
Fe^{2-}	1	-3316895.545
Fe^{2-}	3	-3317084.259
Fe^{2-}	5	-3316929.162
Fe^{2-}	7	-3316701.553
Fe^{3-}	2	-3315655.019
Fe^{3-}	4	-3315549.195
Fe^{3-}	6	-3315420.915
Fe^{3-}	8	-3315224.589

Table A3: Electronic energy of the investigated cyclopentadienyl iron (FeCp) and ions. **Table A4:** Electronic energy of the investigated cyclopentadienyl iron (FeCp) and ions.

Species	Mult.	E(kJ/mol)
FeCp	2	-3826044.324
FeCp	4	-3826089.369
FeCp	6	-3826174.192
FeCp	8	-3825746.202
FeCp ⁻	1	-3825967.055
FeCp ⁻	3	-3826070.373
FeCp ⁻	5	-3826156.711
FeCp ⁻	7	-3825924.769
FeCp ²⁻	2	-3825589.064
FeCp ²⁻	4	-3825695.622
FeCp ²⁻	6	-3825516.466
FeCp ²⁻	8	-3825310.317
FeCp ³⁻	1	-3824544.717
FeCp ³⁻	3	not conv.
FeCp ³⁻	5	not conv.
FeCp ³⁻	7	-3824512.204
FeCp ⁺	1	-3825445.008
FeCp ⁺	3	-3825498.682
FeCp ⁺	5	-3825551.000
FeCp ⁺	7	-3825388.258
FeCp ²⁺	2	-3824121.412
FeCp ²⁺	4	-3824247.976
FeCp ²⁺	6	-3824217.251
FeCp ²⁺	8	not conv.
FeCp ³⁺	1	-3821950.916
FeCp ³⁺	3	-3822334.868
FeCp ³⁺	5	-3822296.381
FeCp ³⁺	7	not conv.

Species	Mult.	E(kJ/mol)
Cp	2	-508112.481
Cp	4	-507751.640
Cp	6	-507172.418
Cp	8	-506342.322
Cp ⁻	1	-508252.303
Cp ⁻	3	-507842.578
Cp ⁻	5	-507536.603
Cp ⁻	7	-506945.187
Cp ²⁻	2	-507542.654
Cp ²⁻	4	-507163.743
Cp ²⁻	6	-506750.229
Cp ²⁻	8	-506156.086
Cp ³⁻	1	-506450.742
Cp ³⁻	3	-506449.358
Cp ³⁻	5	-506144.702
Cp ³⁻	7	-505732.214
Cp ⁺	1	-507282.096
Cp ⁺	3	-507328.177
Cp ⁺	5	-506643.999
Cp ⁺	7	not conv.
Cp ²⁺	2	-505825.394
Cp ²⁺	4	-505603.022
Cp ²⁺	6	-504989.088
Cp ²⁺	8	not conv.
Cp ³⁺	1	-503684.891
Cp ³⁺	3	-503423.699
Cp ³⁺	5	-503198.969
Cp ³⁺	7	-502563.097

Table A5: Relative energies of the different electronic spin states of FeCp₂, FeCp, Cp, Fe, and respective ions, calculated at the def2tzvp/6-311G(2df,2pd) level, with Grimmes D3 dispersion correction. The electronic spin state is presented in parentheses. sing., doub., trip., quar., quin., sext., sept., and oct. refer to a singlet, doublet, triplet, quartet, quintet, sextet, septet, and octet state, respectively. - signifies the energy of the structure could not be converged.

Species	Relative energies (kJ/mol)							
FeCp ₂	0.0	(sing.)	82.7	(trip.)	76.8	(quin.)	370.9	(sept.)
FeCp ₂ [−]	0.0	(doub.)	15.5	(quar.)	73.0	(sext.)	483.7	(oct.)
FeCp ₂ ^{2−}	98.6	(sing.)	1.0	(trip.)	0	(quin.)	82.1	(sept.)
FeCp ₂ ⁺	0	(doub.)	27.8	(quar.)	105.8	(sext.)	457.3	(oct.)
FeCp ₂ ²⁺	283.2	(sing.)	0	(trip.)	128.0	(quin.)	209.9	(sept.)
FeCp	129.9	(doub.)	84.8	(quar.)	0	(sext.)	428.0	(oct.)
FeCp [−]	189.7	(sing.)	86.3	(trip.)	0	(quin.)	231.9	(sept.)
FeCp ^{2−}	106.6	(doub.)	0	(quar.)	179.1	(sext.)	385.3	(oct.)
FeCp ^{3−}	0	(sing.)	-	(trip.)	-	(quin.)	103.8	(sept.)
FeCp ⁺	106.0	(doub.)	52.3	(quar.)	0	(sext.)	162.7	(quar.)
FeCp ²⁺	126.6	(sing.)	0	(trip.)	30.7	(quin.)	-	(sept.)
FeCp ³⁺	384.0	(doub.)	0	(quar.)	38.5	(sext.)	-	(quar.)
Cp	0.0	(doub.)	360.8	(quar.)	940.1	(sext.)	1770.2	(quar.)
Cp [−]	0.0	(sing.)	409.7	(trip.)	715.7	(quin.)	1307.1	(sept.)
Cp ^{2−}	0.0	(doub.)	378.9	(quar.)	792.4	(sext.)	1386.6	(quar.)
Cp ^{3−}	0.0	(sing.)	1.4	(trip.)	306.0	(quin.)	718.5	(sept.)
Cp ⁺	46.1	(doub.)	0.0	(quar.)	684.2	(sext.)	-	(quar.)
Cp ²⁺	0.0	(sing.)	222.4	(trip.)	836.3	(quin.)	-	(sept.)
Cp ³⁺	0.0	(doub.)	261.2	(quar.)	485.9	(sext.)	1121.8	(quar.)
Fe	-	(sing.)	41.2	(trip.)	0.0	(quin.)	333.2	(sept.)
Fe [−]	842.0	(doub.)	7.2	(quar.)	0.0	(sext.)	-	(quar.)
Fe ^{2−}	378.9	(sing.)	241.6	(trip.)	0.0	(quin.)	443.1	(sept.)
Fe ^{3−}	611.0	(doub.)	367.3	(quar.)	0.0	(sext.)	6190.2	(quar.)
Fe ⁺	815.4	(sing.)	0.0	(trip.)	267.8	(quin.)	-	(sept.)
Fe ²⁺	188.7	(doub.)	0.0	(quar.)	155.1	(sext.)	382.7	(quar.)
Fe ³⁺	0.0	(sing.)	105.8	(trip.)	234.1	(quin.)	-	(sept.)

Table A6: The lowest-energy electronic spin states and bond lengths for the species FeCp₂, FeCp, Cp, Fe, and their respective ions. The calculations were performed at the def2tzvp/6-311G(2df,2pd) level including Grimmes D3 dispersion correction. The obtained bond lengths after the inclusion of diffuse functions are included in the parentheses, calculated at the def2tzvp/6-311++G(2df,2pd) level including Grimmes D3 dispersion correction.

Species	State	Fe-C (Å)	C-C (Å)	C-H (Å)
FeCp ₂ ⁻	Doublet	2.170 - 2.194 (2.133-2.190)	1.422 - 1.434 (1.414-1.423)	1.078-1.080 (1.078-1.079)
FeCp ₂ ²⁻	Quintet	2.345 - 2.349 (2.314)	1.420 (1.423)	1.082 (1.079)
	Triplet	2.145-2.205 (2.113-2.177)	1.413-1.432 (1.418)	1.082-1.084 (1.080)
FeCp ₂ ⁺	Doublet	2.089	1.424	1.077
FeCp ₂ ²⁺	Triplet	2.106-2.180	1.413-1.432	1.080
FeCp	Sextet	2.300-2.367 (2.305-2.372)	1.414-1.420 (1.415-1.420)	1.077 (1.077)
FeCp ⁻	Quintet	2.238 (2.241)	1.426 (1.421-1.432)	1.078 (1.074-1.078)
FeCp ²⁻	Quartet	2.482 (-)	1.419 (-)	1.080 (-)
FeCp ³⁻	Singlet	2.053-2.118 (2.070-2.108)	1.427-1.451 (1.421-1.432)	1.091-1.144 (1.074-1.078)
FeCp ⁺	Quintet	2.162-2.257	1.420-1.430	1.078
FeCp ²⁺	Quartet	2.261-2.325	1.381-1.477	1.081-1.084
FeCp ³⁺	Triplet	2.395-2.553	1.451	1.092
Cp	Doublet	- -	1.353-1.466 (1.366-1.479)	1.077-1.080 (1.077-1.080)
Cp ⁻	Singlet	-	(1.410) (1.412)	(1.085) (1.083)
Cp ²⁻	Doublet	-	1.410 (1.410)	1.104 (1.085)
Cp ³⁻	Singlet	-	(1.412)	(1.214)
		-	(1.415)	(1.085)
Cp ⁺	Triplet	-	1.420	1.079
Cp ²⁺	Doublet	-	1.395-1.507	1.0861.091
Cp ³⁺	Singlet	-	1.474	1.106

8.2 Appendix B.

Appendix B visualises the optimised FeCp_2 , FeCp , and Cp structures in Figures B2-B3. Bond lengths are given in Å.

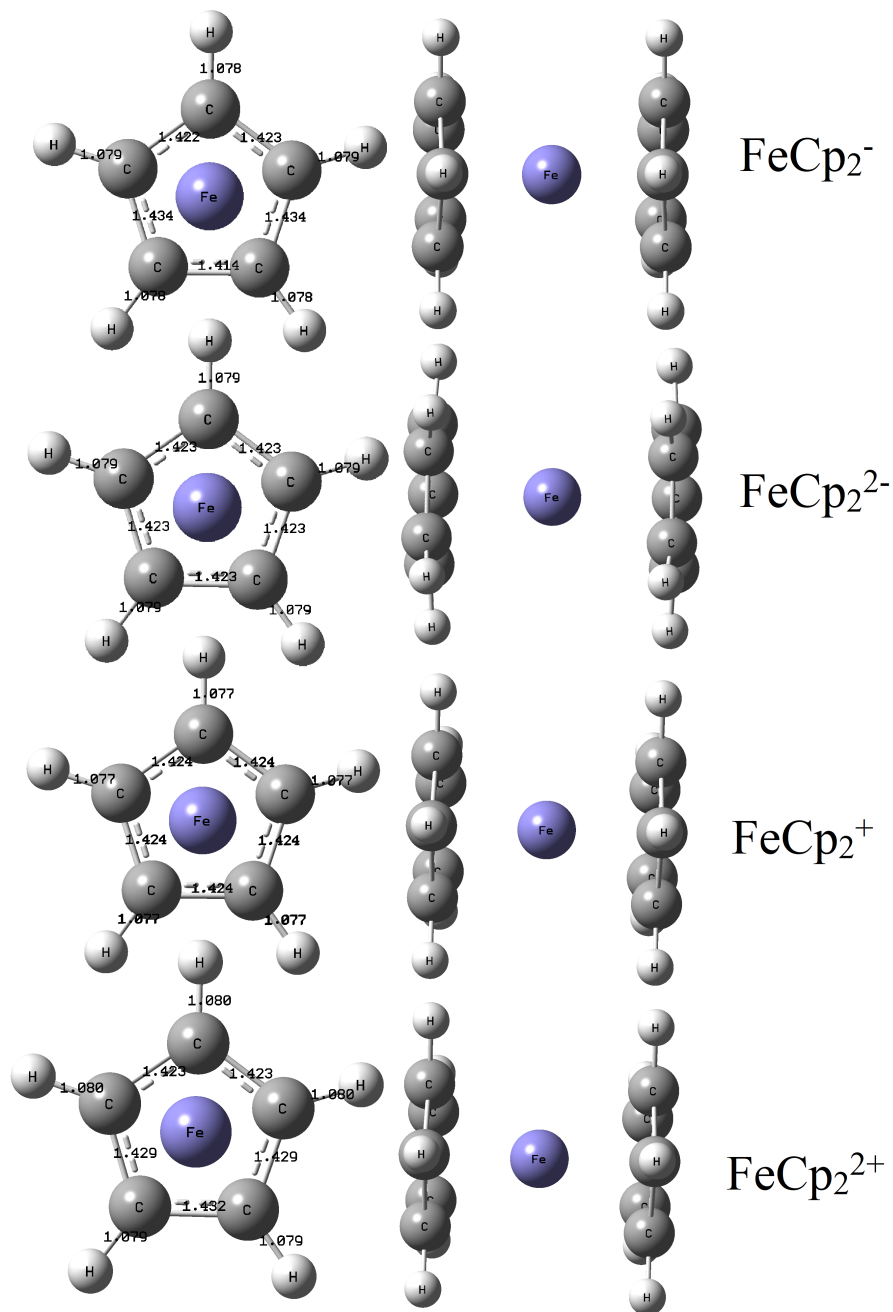


Figure B1: Geometrical structures (top view and side view) of the ferrocene ions.

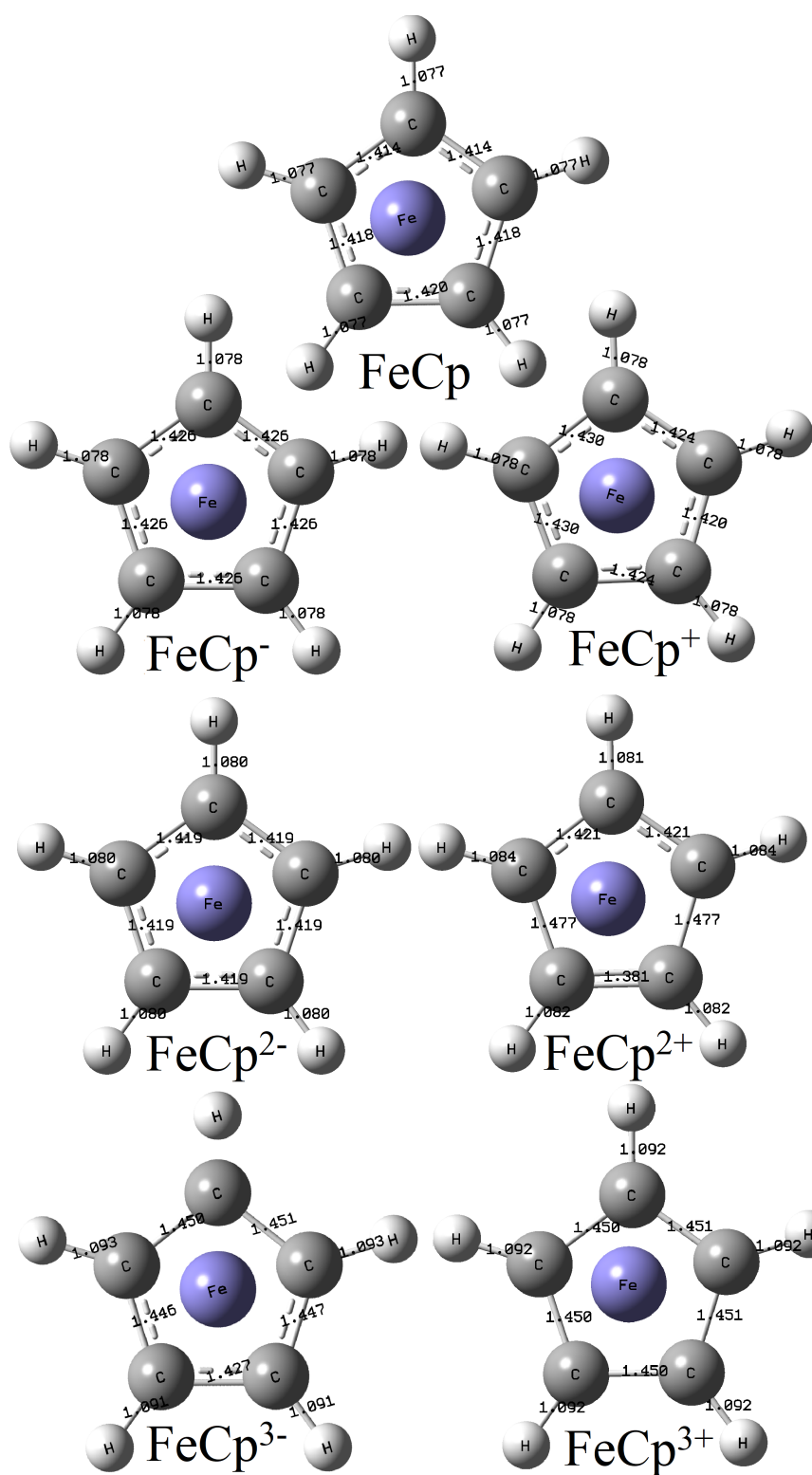


Figure B2: Geometrical structures of the FeCp complex, and ions.

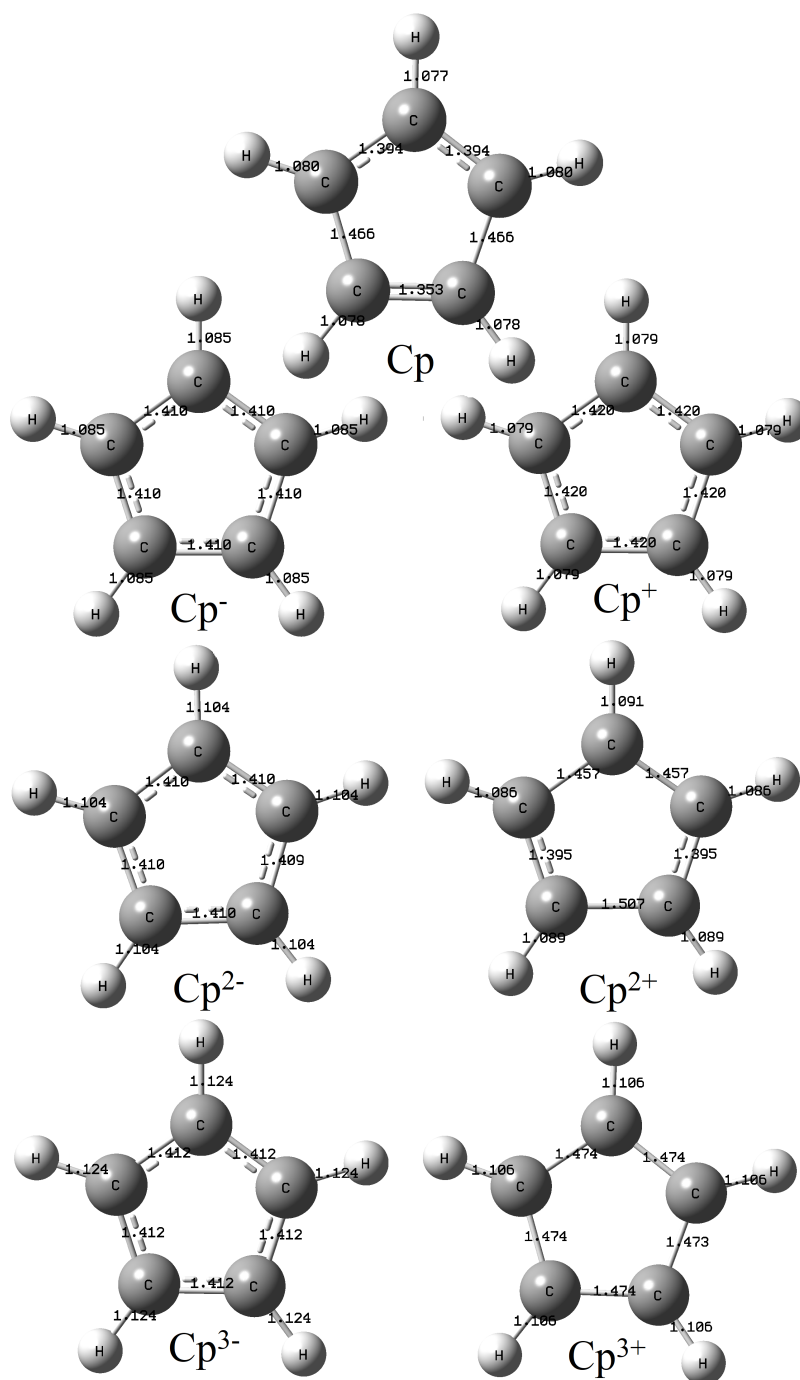


Figure B3: Geometrical structures of the cyclopentadienyl fragment and ions.

8.3 Appendix C.

Appendix C compiles the investigated dissociation reactions of ferrocene and ions in Table C1.

Table C1: The investigated dissociation reactions of FeCp_2 and ions FeCp_2^- , FeCp_2^{2-} , FeCp_2^+ , and FeCp_2^{3+} into fragments FeCp , FeCp^- , FeCp^{2-} , FeCp^{3-} , FeCp^+ , and FeCp^{2+} and FeCp^{3+} , Cp , Cp^- , Cp^{2-} , Cp^{3-} , Cp^+ , and Cp^{2+} and Cp^{3+} , and Fe , Fe^- , Fe^{2-} , Fe^{3-} , Fe^+ , and Fe^{2+} and Fe^{3+} . All values are in kJ/mol. Calculated at the def2tzvp/6-311G(2df,2pd) level, with Grimmes D3 dispersion correction.

Reactant	Products	$\Delta_r E$	$\Delta_r H$	$\Delta_r G$
FeCp_2	$\text{FeCp}^{3+} + \text{Cp}^{3-}$	5899	5849	5784
	$\text{FeCp}^{2+} + \text{Cp}^{2-}$	2893	2858	2790
	$\text{FeCp}^+ + \text{Cp}^-$	881	863	794
	$\text{FeCp} + \text{Cp}$	397	380	305
	$\text{FeCp}^- + \text{Cp}^+$	1199	1183	1120
	$\text{FeCp}^{2-} + \text{Cp}^{2+}$	3163	3092	3019
	$\text{FeCp}^{3-} + \text{Cp}^{3+}$	6455	6429	6367
	$\text{Fe} + 2 \text{Cp}$	673	647	532
	$\text{Fe}^+ + \text{Cp}^- + \text{Cp}$	1252	1225	1116
	$\text{Fe}^{2+} + 2 \text{Cp}^-$	2702	2674	2573
	$\text{Fe}^{3+} + \text{Cp}^- + \text{Cp}^{2-}$	6453	6414	6311
	$\text{Fe}^- + \text{Cp} + \text{Cp}^+$	1386	1366	1257
	$\text{Fe}^{2-} + 2 \text{Cp}^+$	2944	2929	2826
	$\text{Fe}^{3-} + \text{Cp}^+ + \text{Cp}^{2+}$	5876	5853	5745
FeCp_2^-	$\text{FeCp}^{3+} + \text{Cp}^{4-}$	7267	7243	7193
	$\text{FeCp}^{2+} + \text{Cp}^{3-}$	3919	3890	3841
	$\text{FeCp}^+ + \text{Cp}^{2-}$	814	1509	1459
	$\text{FeCp} + \text{Cp}^-$	191	188	138
	$\text{FeCp}^- + \text{Cp}$	348	341	291
	$\text{FeCp}^{2-} + \text{Cp}^+$	1594	1545	1497
	$\text{FeCp}^{3-} + \text{Cp}^{2+}$	4247	4219	4164
	$\text{Fe}^{3+} + 2 \text{Cp}^{2-}$	7096	7060	6976
	$\text{Fe}^{2+} + \text{Cp}^- + \text{Cp}^{2-}$	3345	3321	3237
	$\text{Fe}^+ + 2 \text{Cp}^-$	1045	1033	949
	$\text{Fe} + \text{Cp}^- + \text{Cp}$	466	455	365
	$\text{Fe}^- + 2 \text{Cp}$	535	525	429
	$\text{Fe}^{2-} + \text{Cp} + \text{Cp}^+$	2093	2088	1998
	$\text{Fe}^{3-} + 2 \text{Cp}^+$	4306	4307	4223

Table C1 continued.					
Reactant	Products	$\Delta_r E$	$\Delta_r H$	$\Delta_r G$	
FeCp_2^{2-}	$\text{FeCp}^{2+} + \text{Cp}^{4-}$	4803	4791	4752	
	$\text{FeCp}^+ + \text{Cp}^{3-}$	2066	2049	2012	
	$\text{FeCp} + \text{Cp}^{2-}$	351	343	304	
	$\text{FeCp}^- + \text{Cp}^-$	-342	-343	-374	
	$\text{FeCp}^{2-} + \text{Cp}$	259	212	171	
	$\text{FeCp}^{3-} + \text{Cp}^+$	2195	2181	2144	
	$\text{Fe}^{3+} + \text{Cp}^{2-} + \text{Cp}^{3-}$	7638	7600	7529	
	$\text{Fe}^{2+} + 2 \text{Cp}^{2-}$	3505	3476	3404	
	$\text{Fe}^+ + \text{Cp}^{2-} + \text{Cp}^-$	1205	1188	1116	
	$\text{Fe} + 2 \text{Cp}^-$	-224	-229	-300	
	$\text{Fe}^- + \text{Cp} + \text{Cp}^-$	-155	-159	-236	
	$\text{Fe}^{2-} + 2 \text{Cp}$	758	755	672	
	$\text{Fe}^{3-} + \text{Cp} + \text{Cp}^+$	2972	2974	2897	
FeCp_2^+	$\text{FeCp}^{3+} + \text{Cp}^{2-}$	4127	4085	4022	
	$\text{FeCp}^{2+} + \text{Cp}^-$	1504	1479	1415	
	$\text{FeCp}^+ + \text{Cp}$	341	322	251	
	$\text{FeCp} + \text{Cp}^+$	502	488	422	
	$\text{FeCp}^- + \text{Cp}^{2+}$	2022	1996	1931	
	$\text{FeCp}^{2-} + \text{Cp}^{3+}$	4624	4569	4511	
	$\text{Fe}^{3+} + 2 \text{Cp}^-$	5064	5034	4936	
	$\text{Fe}^{2+} + \text{Cp}^- + \text{Cp}$	2162	2133	2029	
	$\text{Fe}^+ + 2 \text{Cp}$	712	684	573	
	$\text{Fe} + \text{Cp}^+ + \text{Cp}$	777	755	649	
	$\text{Fe}^- + 2 \text{Cp}^+$	1491	1474	1375	
	$\text{Fe}^{2-} + \text{Cp}^{2+} + \text{Cp}^+$	3767	3743	3638	
	$\text{Fe}^{3-} + 2 \text{Cp}^{2+}$	6699	6667	6557	
FeCp_2^{2+}	$\text{FeCp}^{3+} + \text{Cp}^-$	2290	2264	2212	
	$\text{FeCp}^{2+} + \text{Cp}$	517	496	437	
	$\text{FeCp}^+ + \text{Cp}^+$	-2	-12	-66	
	$\text{FeCp} + \text{Cp}^{2+}$	878	860	799	
	$\text{FeCp}^- + \text{Cp}^{3+}$	3036	3031	2988	
	$\text{Fe}^{3+} + \text{Cp} + \text{Cp}^-$	4077	4051	3958	
	$\text{Fe}^{2+} + 2 \text{Cp}$	1175	1151	1051	
	$\text{Fe}^+ + \text{Cp} + \text{Cp}^+$	369	351	256	
	$\text{Fe} + 2 \text{Cp}^+$	434	421	332	
	$\text{Fe}^- + \text{Cp}^{2+} + \text{Cp}^+$	1866	1846	1751	
	$\text{Fe}^{2-} + 2 \text{Cp}^{2+}$	4142	4115	4014	
	$\text{Fe}^{3-} + \text{Cp}^{3+} + \text{Cp}^{2+}$	7712	7702	7614	

8.4 Appendix D.

Appendix D provides the relevant results from a previous, unpublished project report, where I investigated different functionals and basis sets to accurately describe the gas phase ferrocene, using Gaussian 16. The reaction enthalpy of the reaction $\text{Fe} + 2 \text{C}_2\text{H}_5 \longrightarrow \text{FeCp}_2$, the energy difference between the eclipsed and staggered ferrocene conformation, and the Fe-C, C-C, and C-H bond lengths were computed. The calculations were performed for the singlet state ferrocene and results are compiled in Tables D1 and D2. Figures D1 and D2 show the results from the asymmetric one-ring and the symmetric two-ring dissociation of ferrocene of different electronic spin states. The ring-iron distance was scanned using the scan method implemented in Gaussian 16, at the def2tzvp/6-311G(2df,2pd) level, with Grimmes D3 dispersion correction. The lowest electronic energies of each step are compiled in Table D3.

Table D1: Calculated energy difference of the eclipsed and staggered conformation ΔE and reaction enthalpy ΔH_r° of the reaction $\text{Fe} + 2 \text{C}_2\text{H}_5 \longrightarrow \text{FeCp}_2$, for different functionals and basis sets with different numbers of basis set electrons (e) and functions (f), with and without Grimmes D3 dispersion correction (D).

Functional	Basis set	e/f	ΔE (kJ/mol)	ΔH_r° (kJ/mol)
B3LYP	6-31G* (D)	96/206	-0.4	-1446.4
B3LYP	6-31G** (D)	96/236	-0.5	-1343.3
B3LYP	6-31+G* (D)	96/259	-3.0	-1319.8
B3LYP	6-31+G** (D)	96/289	-3.1	-1363.7
B3LYP	6-31++G* (D)	96/269	-3.0	-1371.8
B3LYP	6-31++G** (D)	96/299	-3.1	-1363.9
B3LYP	6-31G**	96/236	-0.5	-1384.3
B3LYP	LanL2DZ (D)	86/132	-2.9	-1286.2
B3LYP	LANL2DZ/6-31G* (D)	86/182	-2.4	-1366.0
B3LYP	LANL2DZ/6-31G** (D)	86/212	-2.5	-1263.9
B3LYP	LANL2DZ/6-31+G** (D)	86/252	-2.5	-1293.6
B3LYP	LANL2DZ/6-31++G** (D)	86/262	-2.5	-1295.3
B3LYP	LANL2DZ	86/132	-2.8	-1290.8
B3LYP	LANL2DZ/6-31G**	86/212	-2.5	-1046.7
B3LYP	def2tzv/6-311G (D)	96/190	-1.0	-847.1
B3LYP	def2tzvp/6-311G(2df,2pd) (D)	96/405	-2.2	-1304.8
B3LYP	def2tzvpp/6-311G(3df,3pd) (D)	96/424	-2.0	-1303.4
B3LYP	def2tzvp (D)	96/415	-2.1	-1275.5
B3LYP	def2tzvp	96/415	-2.0	-1038.6
B3LYP	def2qzvp (D)	96/954	-2.2	-1269.3
B3LYP	def2qzvp	96/954	-2.1	-1140.9
PBE	6-31(d,p) (D)	96/236	-1.9	-1272.6
PBE	def2tzvp (D)	96/415	-3.7	-1259.0
MO6-2X	6-31G(d,p) (D)	96/236	1.0	-1783.3
MO6-2X	def2tzvp (D)	96/415	-0.6	-1535.8

Table D2: Calculated ferrocene Fe-C, C-C, and C-H bond lengths for different functionals and basis set with different number of basis set electrons (e) and functions (f), with and without Grimmes D3 dispersion correction (D).

Functional	Basis set	e/f	Fe-C	C-C	C-H
B3LYP	6-31G* (D)	96/206	2.05	1.43	1.08
B3LYP	6-31G** (D)	96/236	2.05	1.43	1.08
B3LYP	6-31+G* (D)	96/259	2.06	1.43	1.08
B3LYP	6-31+G** (D)	96/289	2.06	1.43	1.08
B3LYP	6-31++G* (D)	96/269	2.06	1.43	1.08
B3LYP	6-31++G** (D)	96/299	2.06	1.43	1.08
B3LYP	6-31G**	96/236	2.07	1.43	1.08
B3LYP	LanL2DZ (D)	86/132	2.11	1.44	1.08
B3LYP	LANL2DZ/6-31G* (D)	86/182	2.07	1.43	1.08
B3LYP	LANL2DZ/6-31G** (D)	86/212	2.07	1.43	1.08
B3LYP	LANL2DZ/6-31+G** (D)	86/252	2.08	1.43	1.08
B3LYP	LANL2DZ/6-31++G** (D)	86/262	2.08	1.43	1.08
B3LYP	LanL2DZ	86/132	2.12	1.44	1.08
B3LYP	LANL2DZ/6-31G**	86/212	2.08	1.43	1.08
B3LYP	def2tzv/6-311G (D)	96/190	2.09	1.43	1.08
B3LYP	def2tzvp/6-311G(2df,2pd) (D)	96/405	2.07	1.42	1.08
B3LYP	def2tzvpp/6-311G(3df,3pd) (D)	96/424	2.07	1.42	1.08
B3LYP	def2tzvp (D)	96/415	2.07	1.42	1.08
B3LYP	def2tzvp	96/415	2.08	1.42	1.08
B3LYP	def2qzvp (D)	96/954	2.07	1.42	1.08
B3LYP	def2qzvp	96/954	2.08	1.42	1.08
PBE	6-31(d,p) (D)	96/236	2.10	1.42	1.08
PBE	def2tzvp (D)	96/415	2.14	1.42	1.08
MO6-2X	6-31G(d,p) (D)	96/236	2.02	1.44	1.090
MO6-2X	def2tzvp (D)	96/415	2.04	1.43	1.09

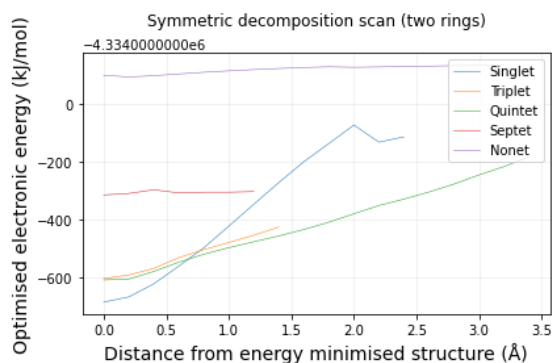


Figure D1: Electronic energies of the symmetric dissociation of both rings of ferrocene with different electronic spin states.

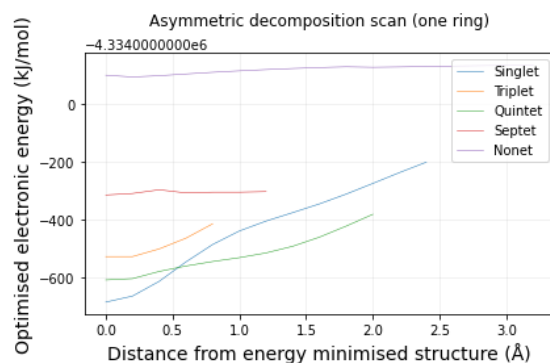


Figure D2: Electronic energies of the asymmetric dissociation of one ring of ferrocene with different electronic spin states.

Table D3: The relative electronic energies for the asymmetric and symmetric decomposition scan. The scanning distance is for the asymmetric scan the moving distance of one ring from the center of the remaining iron and carbon ring, and for the symmetric scan, it denotes the moving distance of each of the two rings from the iron center. The energy difference ΔE is the difference between the electronic energy of the asymmetric and symmetric decomposition of each scanning step.

Distance(Å)	Asymmetric(kJ/mol)	Symmetric(kJ/mol)	ΔE (kJ/mol)
0	0	0	0
+0.2	20.9	63.1	-42.2
+0.4	72.0	165.7	-93.7
+0.6	139.2	208.9	-69.8
+0.8	140.5	251.4	-110.9
+1.0	153.9	305.8	-151.9
+1.2	170.3	356.6	-186.3
+1.4	193.4	408.6	-215.2
+1.6	225.0	469.2	-244.2
+1.8	263.2	-	-
+2.0	304.1	-	-